Sulfur in Apatite as a Volatile and Redox Tracer in Magmatic and Magmatic-Hydrothermal Systems

by

Brian A. Konecke

A dissertation submitted in partial fulfillment
of the requirements for the degree of
Doctor of Philosophy
(Earth and Environmental Sciences)
in the University of Michigan
2019

Doctoral Committee:

Professor Adam Simon, Chair
Research Professor Jeff Alt
Professor Joel Blum
Research Associate Adrian Fiege, American Museum of Natural History
Assistant Professor Shelie Miller
Assistant Professor Gordon Moore, University of California-Davis

"Embrace failure, for it is the ultimate teacher".

Brian A. Konecke

bkonecke@umich.edu
ORCID: 0000-0003-1702-0908

© Brian A. Konecke 2019
All Rights Reserved

DEDICATION

This work is dedicated to my beloved family, friends, mentors, wife Kate, and our daughter Ann. Without your unyielding encouragement and patience, none of this would be possible.

ACKNOWLEDGEMENTS

I would like to thank my committee members for allotting their valuable time and effort to provide feedback on the work presented in this dissertation: Professors Joel Blum, Shelie Miller, Jeff Alt, and Drs. Gordon Moore and Adrian Fiege. I especially like to thank my advisors Professor Adam Simon, and Dr. Adrian Fiege for their unparalleled wisdom, guidance, support, patience, and freedom while learning to become an independent researcher. I am eternally grateful for them.

I want to thank Professors Francois Holtz and Harald Behrens, as they served as my mentors and gracious hosts during my several research trips to Leibniz University–Hannover (Germany). Additionally, I cannot fully express my gratitude for permitting me access to their world-class IHPV and CSPV laboratories. The experimental portion of this dissertation would not be possible without the expertise and technical "Jedi mastery" of my friends and colleagues Dr. André Stechern and Stefan Linsler, whom repeatedly went above and beyond the call of duty to operate and maintain the IHPV vessels. Their efforts were fundamental to the success of these projects, and for making Hannover feel like a second home. I thank and appreciate the graduate students and researchers whom I have had the privilege to interact with, including but not limited to: David N., Olivier N. Insa D., Lennart F., Tim M., Soren W., Tony & Mona, Kristina S., Mahender B., Mari Zea., Angela Z., Klein Kroepke, the technical and workshop staff, and many more.

The presented work was made possible via the finances and resources provided by the Rackham Graduate School, Society of Economic Geologists (SEG), American

Association of Petroleum Geologists (AAPG), Department of Earth and Environmental Sciences (EARTH), Electron Microbeam Analysis Lab (EMAL), National Science Foundation, Advanced Photon Source at Argonne National Laboratory, Institute for Mineralogy-Leibniz University Hannover, and the American Museum of Natural History.

I would like to acknowledge University of Michigan's Department of Earth and Environmental Sciences, including the students, faculty, and staff. Special thanks to my collaborators: Professors Udo Becker, Fleurice Parat, Martin Reich, Santiago (Carlos) Tassara, José Tómas Ovalle, and YoungJae Kim, as they have greatly expanded my understanding of geochemistry. I appreciate the EARTH family for their support (and entertainment), including: Laura M.M, Jameson, Mark, Xiaofei, Sara, Juliana, Man Sam, Erin, Owen, YJ, Will, and many others. I am blessed to have been part of an outstanding ***lab family***: thank you Tom, Laura B., Liz, Jaayke and Adrian (academic older siblings and role models), Tristan (academic twin, former roommate), Nikita (spirit twin), Prof. Dr. Antonio Arribas, Prof. Steve Kessler, Daniel, Gephen, Maria, Jackie, Anne, and Zach.

Finally, I would like to acknowledge my family and friends for their relentless support and inspiration, including: my wife (Kate) and our daughter (Ann), my parents and in-laws (Diane & Mark Konecke, Bob & Ann Weiss), my siblings (Jack "Henry" Konecke, Sara & Charlie Beisel), and my comrades (Ryan "Rapo" Rapshus, Ricky "Shifty" Palandri, and Adam Vales).

TABLE OF CONTENTS

LIST OF TABLES

LIST OF FIGURES

LIST OF APPENDICES

ABSTRACT

Sulfur (S) is the third most abundant volatile element in terrestrial magmatic systems, where the oxidation state(s) and behavior of S are intrinsically linked to oxygen fugacity (fO_2). However, the quantification of the oxidation states and distribution (i.e., transport and storage) of S during the evolution of magmatic systems remains poorly understood. Considering the ability of the mineral apatite to crystallize from silicate melts, the intra-and-inter-crystalline zonation with respect to S content and oxidation state(s) of S-in-apatite may serve as a proxy to reconstruct redox and degassing processes in magmatic environments.

In Chapter 2, I used micro X-ray absorption near edge structure spectroscopy (μ-XANES) at the S *K*-edge to measure the formal oxidation state(s) in experimentally grown apatite and co-existing lamproitic melt. The study demonstrates-for the first time-that apatite incorporates three oxidation states of S (S^{2-}, S^{4+}, and S^{6+}) in variable proportions, as a function of the prevailing fO_2 of the system that spans the complete transition of sulfide (S^{2-}) to sulfate (S^{6+}) in the silicate melt. A new technique involving the integrated peak area ratios of S^{2-}, S^{4+} and S^{6+} (e.g., $S^{6+}/\Sigma S$) in apatite was developed to empirically correlate the proportions of sulfur oxidation states in apatite to the redox conditions of the system, thus serving as the foundation for an empirical oxy-sulfo-barometer.

In Chapter 3, I attempt to reconcile the observation that apatite crystallizing from late-stage lunar felsic (rhyolitic) melts contains relatively elevated concentrations of S

(up to ~430 μg/g S), despite crystallizing from a reduced and anhydrous melt containing <100 μg/g S. Apatite crystallization experiments preformed at conditions relevant to late-stage lunar magmatism indicate that S behaves incompatibly (e.g., $D_S^{ap/m}$ <<1) with respect to apatite that crystallizes from rhyolitic melts under low fO_2 conditions (e.g., ≤FMQ), suggesting that the elevated S contents in lunar apatite cannot be explained by fractional crystallization processes alone. Instead, mechanisms involving either several orders of magnitude higher fO_2, or metasomatic reactions involving apatite and S and Cl-bearing, F-poor volatile phase(s), is required.

In Chapter 4, I performed apatite crystallization experiments to constrain the influence of fO_2 and bulk S contents on the oxidation states of S-in-apatite, and the distribution of S between apatite and melt (i.e., $D_S^{ap/m}$). The experimental results indicate that the integrated $S^{6+}/\Sigma S$ peak area ratios, centroid energies (eV), and $D_S^{ap/m}$ increase systematically with increasing fO_2. From this dataset, an empirical S-in-apatite oxybarometer was developed and is applicable to mafic systems such as mid ocean ridge basalt (MORB), relatively reduced ocean island basalts (OIB), and backarc basin basalt (BABB) systems.

CHAPTER 1: INTRODUCTION

1.1 SULFUR IN MAGMATIC SYSTEMS

Subduction zones link the Earth's asthenosphere to the lithosphere and hydrosphere and moderate the geochemical cycle, including the sulfur (S) budget (Evans, 2012). Arc volcanism serves as a conduit that titrates S between the oceanic slab and the Earth's surface (Gill, 1981; Alt et al., 1993; Arculus, 1994), and ultimately enables S to participate in various geologic, atmospheric, and biologic processes (Faure, 1986; Métrich and Mandeville 2010; Mandeville, 2010; Manning, 2011). Despite the ubiquity of S in terrestrial magmatic and magmatic-hydrothermal systems, the mechanisms that control the transport and storage of S in magmatic systems remain a geochemical challenge (Baker and Moretti, 2011).

The June 1991 eruption of Mt. Pinatubo (Philippines) caused one of the largest climatic disturbances of the 20th century by releasing 17-20 megatons of SO_2 into the stratosphere (Van Hoose et al., 2013; and references therein) and resulted in a decrease of global mean air temperature by up to 0.5^{o}C (Parker et al., 1996; Robock, 2002). The S released upon eruption equates to ~10-20 times more S than could be dissolved in the pre-erupted dacitic melt based on inferred T-P-X-fO_2 conditions (Gerlach et al., 1997; Keppler, 1999; Van Hoose et al., 2013; Masotta et al., 2016; and references therein). The paradoxical observation, that evolved silicate magmas are associated with S-rich gases and fluids despite being significantly less capable of dissolving sulfur compared to mafic

magmas, is known in the literature as the "excess sulfur" problem (Andres et al., 1991; Streck and Dilles, 1998).

Several hypotheses have been proposed to reconcile the "excess sulfur" problem, including: (a) the breakdown of sulfate-bearing minerals (e.g., anhydrite; Devine et al., 1994); (b) magma mixing (Kress, 1997); (c) release of a S-rich, hydrous fluid/vapor (Wallace and Gerlach, 1994; Keppler, 1997); (d) degassing of an underplating basaltic magma (de Hoog et al., 2005; Van Hoose et al., 2013); and (e) kinetic degassing of S upon decompression of an evolved melt (Fiege et al., 2014). However, the "excess sulfur" phenomenon underpins a more fundamental geochemical endeavor that began several decades before the eruption of Mt. Pinatubo.

For more than half a century, geoscientists have aimed to understand the magmatic component of the S cycle by probing the mechanisms responsible for the transport (i.e., silicate melt, fluid/gas, sulfide melt, mineral phases) and storage of S in magmatic reservoirs (Baker and Moretti, 2011; and references therein). Numerous investigators have used experimental and thermodynamic techniques in combination with analyses of natural samples to evaluate the abundance of S-bearing phases within magmatic systems. The data indicate that the transport and storage of S in magmatic systems is a function of S solubility and partitioning, and are intrinsically linked to the oxygen fugacity (fO_2) of the system (Métrich and Mandeville 2010; Simon and Ripley, 2011; Baker and Moretti, 2011; and references therein). Based on experimental evidence, it is well known that the solubility of S in silicate melts increases dramatically as the fO_2 of the system increases (Carroll and Rutherford, 1985; Jugo et al., 2005; Jugo, 2009; Jugo et al., 2010). Elucidating the behavior of S as a function of magmatic fO_2 is imperative

for understanding the controls on volcanic degassing events (including the excess sulfur phenomenon) and explosivity (Carroll and Rutherford, 1985; Burgisser and Scaillet, 2007; Jugo, 2009; Baker and Moretti, 2011; Head et al., 2018).

Sulfur can be (co-) present as various species and oxidation states in silicate melts, most predominantly as sulfide (S^{2-}) and sulfate (S^{6+}), and can be described by the sulfide-sulfate equilibrium reaction (Carroll and Rutherford, 1985; Matjuschkin et al., 2016), where:

$$S^{2-}{}_{\text{silicate melt}} + 2O_2 \Leftrightarrow SO_4{}^{2-}{}_{\text{silicate melt}} \quad \text{(eq.1)}$$

Silicate melts that are saturated with respect to either a sulfide or sulfate phase are used to constrain the S solubility at a given T-P-X-fO_2 (Baker and Moretti, 2011). Under relatively low fO_2 (reducing) conditions, a silicate melt will saturate with a sulfide phase (e.g., either pyrrhotite and/or sulfide liquid). The solubility of S is defined as the sulfur content at sulfide saturation (SCSS) via the reaction:

$$FeS_{\text{silicate melt}} \Leftrightarrow FeS_{\text{sulfide liquid}} \quad \text{(eq.2)}$$

Under relatively high fO_2 (oxidizing) conditions, a silicate melt will saturate with a sulfate phase (e.g., anhydrite) and the solubility of S is defined as the sulfur content at anhydrite saturation (SCAS) via the reaction:

$$S^{6+}{}_{\text{silicate melt}} + 4O^{2-}{}_{\text{silicate melt}} + Ca^{2+}{}_{\text{silicate melt}} \Leftrightarrow CaSO_{4\ \text{anhydrite}} \quad \text{(eq.3)}$$

The work of Jugo et al. (2010) empirically correlated the relative ratio of sulfate to total sulfur ($S^{6+}/\Sigma S$) in basaltic melt with the fO_2 by using XANES. This insight can be used to predict whether a silicate melt, at a given fO_2, can achieve saturation of a sulfide and/or sulfate phase, and directly corresponds to a magma's ability to transport and/or store S during magmatic evolution.

Jugo et al. (2010) demonstrated that the transition from a S^{2-} to S^{6+} dominated terrestrial silicate melt occurs over a narrow redox range, where $\log(fO_2)$ = ~FMQ to FMQ+2 (FMQ = fayalite-magnetite-quartz oxygen fugacity buffer; Frost, 1991; Wallace and Carmichael, 1994; Jugo et al., 2005; 2010). This narrow range of fO_2 is significant due to the fact that it overlaps with the fO_2 conditions of magmas generated in arc settings as well as for magmas erupted in back-arc, island arc, and ocean-island environments (Ballhaus, 1993; Parkinson and Arculus, 1999; Jugo, 2009). Hence, the ability of a magma to transport S is ultimately a function of the fO_2 and requires the accurate determination of the redox conditions during the evolution of magmatic systems.

Despite the role of redox conditions on magmatic and magmatic-hydrothermal processes (Evans, 2006), the fO_2 of a system remains a difficult geochemical variable to constrain. The redox state of magmas cannot be measured directly, and the electronic structure (i.e., valence state) of polyvalent elements, (e.g., Fe, V, and S) is used as a proxy for indirectly determining the fO_2 of the silicate melt (Head et al., 2018; and references therein). The advent of high resolution, in situ, spectroscopic techniques has permitted the determination of the oxidation states of redox sensitive elements (i.e., S, Fe, V, Cr) in silicate glasses (i.e., matrix glass and/or melt inclusions) and mineral phases (Jugo et al., 2010; Fiege et al., 2017; Berry et al., 2003; 2018; Kelley and Cottrell, 2009; Cottrell et al., 2009; 2018; Righter et al., 2016; Bell et al., 2017; Head et al., 2018). However, the successful application of these spectroscopic techniques can be challenging due to: (a) irradiation induced beam damage of silicate glasses (Wilke et al, 2004; Cottrell et al., 2018), (b) decrepitation and/or leakage of melt inclusions (Head et al., 2018; and references therein), and/or (c) anisotropic effects of minerals related to matrix

composition and crystal orientation (Dyar et al., 2002; Evans et al., 2014; Bell et at., 2017). Therefore, a geochemical tool that is more sensitive to fine scale redox variability and capable of preserving S signatures than the current proxies used for magmatic environments, is needed

The mineral apatite—$Ca_{10}(PO_4)_6(F,Cl,OH)_2$—is commonly present in igneous, metamorphic, sedimentary, and hydrothermal systems (Piccoli and Candela, 2002; Hughes and Rakovan, 2015). The structure of apatite can incorporate approximately 1/3 of the elements in the periodic table, including volatiles (F, Cl, OH, C, S) and redox sensitive elements (S, Fe, Mn; Pan and Fleet, 2002; Parat et al., 2011; Miles et al. 2014). Terrestrial magmatic apatite contains up to >1 wt.% S, which has historically been interpreted to be incorporated into apatite as sulfate (S^{6+}; Streck and Dilles, 1998) due to the observations of S-rich apatite in highly oxidized systems, where S^{6+} is the dominant oxidation state of S. Recently, however, it has been reported that apatite that crystallized from a terrestrial reduced, late-stage and evolved interstitial melt contains significant concentrations of sulfur; ~430 μg/g S (Boyce et al., 2010; 2014). This observation contradicts the hypothesis that apatite only incorporates oxidized S^{6+}, considering that lunar magmatism is characterized by several orders of magnitude more reducing conditions, relative to Earth, where the $S^{6+}/\sum S$ ratio of the melt is 0 (e.g., < ΔFMQ -4; Sato et al., 1973; Jugo et al., 2010). Hence, the hypothesized ability of apatite to incorporate multiple oxidation states of S, in variable proportions as a function of the redox conditions, makes apatite a potential candidate to reliably record the S oxidation states during the evolution of magmatic and magmatic-hydrothermal systems.

In *Chapter 2*, I experimentally investigate the oxidation state(s) of sulfur in apatite and co-existing melt over a range of fO_2 that spans the complete transition from S^{2-} to S^{6+} in the melt in order to test the hypothesis that S-in-apatite can be used to trace the redox evolution of magmatic systems. *In situ* micro X-ray absorption near edge structure (μ-XANES) spectroscopy at S K-edge was used to measure the sulfur oxidation state as a function of oxygen fugacity (fO_2) in natural apatite grains, as well as in experimentally grown apatite and co-existing melt. Sulfur μ-XANES analyses demonstrate that apatite incorporates reduced (S^{2-}), intermediate (S^{4+}) and oxidized (S^{6+}) sulfur in varying proportions as a function of fO_2 and, to my knowledge, represent the first direct evidence that apatite can incorporate sulfur with oxidation states other than S^{6+}. In order to correlate the proportions of sulfur oxidation states in apatite to the prevailing fO_2 of the system, I developed a new method using integrated peak area ratios of S^{2-}, S^{4+} and S^{6+} (e.g., $S^{6+}/\Sigma S$) in apatite. Additionally, I analyzed magmatic-hydrothermal apatite from the Durango (Mexico) and Mina Carmen (Chile) iron oxide apatite (IOA) deposits (Lyons, 1988; Treloar and Colley, 1996) to evaluate: (a) the oxidation state(s) of S in natural apatite from relatively oxidizing conditions, and (b) whether apatite can record the evolution of S signatures (i.e., S content and the proportions of different S oxidation states) during metasomatic reactions involving S-bearing fluids. This chapter is published in *American Mineralogist* **102**, 548–557.

1.2 BEHAVIOR OF SULFUR DURING LATE-STAGE LUNAR MAGMATISM

Bulk-rock analyses of lunar mare basalt samples collected during the Apollo missions suggest that lunar magmas were depleted in volatile elements (e.g., Cl, F, H, S, C) relative to terrestrial analogues (cf. Saal et al., 2008; and references therein). However,

recently reported abundances of volatiles in olivine-hosted silicate melt inclusions (Hauri et al., 2011), lunar volcanic glasses (Robinson and Taylor, 2014; Wetzel et al., 2015), and the mineral apatite (Boyce et al., 2010, 2014; Greenwood et al., 2011), suggest that lunar magmas were volatile-bearing (Hui et al., 2013) and even volatile-rich (Mills et al., 2017). These contradictory findings have stimulated ongoing debate regarding the role and abundance of volatiles in lunar magmatic systems (McCubbin et al., 2015; and references therein).

In *Chapter 3*, I attempt to reconcile the observation that apatite crystallizing from late-stage lunar felsic (rhyolitic) melts contains relatively elevated concentrations of S (up to ~430 μg/g S in the apatite rims), despite crystallizing from a reduced, anhydrous, and evolved melt containing <100 μg/g S. Apatite crystallization experiments equilibrated at conditions relevant to late-stage lunar magmatism indicate that S behaves incompatibly (e.g., D ap/m <<1) with respect to apatite that crystallizes in low fO_2 conditions (e.g., ≤FMQ). This observation suggests that the elevated S contents in lunar apatite cannot be explained via fractional crystallization processes as proposed previously by Boyce et al. (2014). A testable hypothesis involves >5 orders of magnitude higher fO_2 conditions (e.g., where S^{6+} is a dominant oxidation state of S in the melt and apatite); however, this is inconsistent with petrographic observations. Instead, I propose a testable hypothesis that evokes cryptic metasomatic reactions involving apatite, and S and Cl-bearing, F-poor volatile phase(s), likely released during degassing of the underlying magma. This scenario plausibly explains the volatile element zoning in lunar apatite, consistent with some lunar magmas being more volatile rich than previously suggested. This chapter is published in *Geology* **45**, 739-742.

1.3 DEVELOPMENT OF AN EMPIRICAL S-IN-APATITE OXYBAROMETER

In *Chapter 4*, I expand upon the dataset presented in Chapter 2 by performing additional experiments over an expanded range of fO_2 and bulk S concentrations (e.g., sulfur fugacity; fS_2), in order to constrain the influence of fO_2 on the oxidation states of S-in-apatite and the distribution of S between apatite and melt (i.e., $D_S^{ap/m}$). Previous studies have proposed that the $D_S^{ap/m}$ varies systematically as a function of the redox state of the system due to the strong control that the redox conditions have on the oxidation states of S in silicate magmas (Peng et al., 1997; Parat et al., 2011, and references therein; Konecke et al., 2017a, b). In Chapter 4, the S content of apatite and co-existing melt were quantified using electron probe microanalysis (EPMA) and demonstrate that the S content of apatite and $D_S^{ap/m}$ values systematically increases with increasing fO_2. This data set, combined with micro X-ray absorption near edge structure (μ-XANES) spectroscopy at S *K*-edge measurements of experimentally grown apatite, yield promising progress toward the development of an empirical S-in-apatite oxybarometer that is applicable to a range of magmatic environments.

1.4 REFERENCES

Alt J.C., Shanks III, W.C., Jackson M.C. (1993) Cycling of sulfur in subduction zones: The geochemistry of sulfur in the Mariana Island Arc and back-arc trough. Earth Planet. Sci. Lett. 119, 477-494.

Andres R. J., Rose W. I., Kyle P. R., DeSilva S., Francis P., Gardeweg M. and Moreno Roa H. (1991) Excessive sulfur dioxide emissions from Chilean volcanoes. J. Volcanol. Geotherm. Res. 46, 323–329.

Arculus, R.J. (1994) Aspects of Magma Genesis in Arcs. Lithos 33, 189-208.

Baker D. R. and Moretti R. (2011) Modeling the Solubility of Sulfur in Magmas: A 50-Year Old Geochemical Challenge. Rev. Mineral. Geochemistry 73, 167–213.

Ballhaus C. (1993) Redox states of lithospheric and asthenospheric upper mantle. Contrib. to Mineral. Petrol. 114, 331–348.

Bell A. S., Shearer, C., Burger, P., Ren, M., Newville M. and Lanzirotti A. (2017) Quantifying and correcting the effects of anisotropy in XANES measurements of chromium valence in olivine: Implications for a new olivine oxybarometer. Am. Mineral. 102, 1165–1172.

Berry A. J., O'Neill H. S. C., Jayasuriya K. D., Campbell S. J. and Foran G. J. (2003) XANES calibrations for the oxidation state of iron in a silicate glass. Am. Mineral. 88, 967–977.

Berry A. J., Stewart G. A., O'Neill H. S. C., Mallmann G. and Mosselmans J. F. W. (2018) A re-assessment of the oxidation state of iron in MORB glasses. Earth Planet. Sci. Lett. 483, 114–123.

Boyce, J.W., Liu, Y., Rossman, G.R., Guan, Y., Eiler, J.M., Stolper, E.M., and Taylor, L.A. (2010) Lunar apatite with terrestrial volatile abundances. Nature, 466, 466–9.

Boyce J.W., Tomlinson S.M., McCubbin F.M., Greenwood J.P., and Treiman A.H. (2014) The lunar apatite paradox. Science (New York, N.Y.). 344, 400–2.

Burgisser A. and Scaillet B. (2007) Redox evolution of a degassing magma rising to the surface. Nature 445, 194–197.

Carroll M. R. and Rutherford M. J. (1985) Sulfide and sulfate saturation in hydrous silicate melts. J. Geophys. Res. 90, C601.

Cottrell E., Lanzirotti A., Mysen B., Birner S., Kelley K. A., Botcharnikov R., Davis F. A. and Newville M. (2018) A Mössbauer-based XANES calibration for hydrous basalt glasses reveals radiation-induced oxidation of Fe. Am. Mineral. 103, 489–501.

Cottrell E., Kelley K. A., Lanzirotti A. and Fischer R. A. (2009) High-precision determination of iron oxidation state in silicate glasses using XANES. Chem. Geol. 268, 167–179.

De Moor J. M., Fischer T. P., Sharp Z. D., King P. L., Wilke M., Botcharnikov R. E., Cottrell E., Zelenski M., Marty B., Klimm K., Rivard C., Ayalew D., Ramirez C. and Kelley K. A. (2013) Sulfur degassing at Erta Ale (Ethiopia) and Masaya (Nicaragua) volcanoes: Implications for degassing processes and oxygen fugacities of basaltic systems. Geochemistry, Geophys. Geosystems 14, 4076–4108.

Dyar M. D., Gunter M. E., Delany J. S., Lanzarotti A. A. and Sutton S. R. (2002) Systematics in the structure and XANES spectra of pyroxenes, amphiboles, and micas as derived from oriented single crystals. Can. Mineral. 40, 1375–1393.

Evans K. A. (2006) Redox decoupling and redox budgets: Conceptual tools for the study of earth systems. Geology 34, 489–492.

Evans K. A. (2012) The redox budget of subduction zones. Earth-Science Rev. 113, 11–32.

Evans K. A., Dyar M. D., Reddy S. M., Lanzirotti A., Adams D. T. and Tailby N. (2014) Variation in XANES in biotite as a function of orientation, crystal composition, and metamorphic history. Am. Mineral. 99, 443–457.

Faure G. (1986) Principles of Isotope Geology. John Wiley and Sons, New York, 589.

Fiege A., Behrens H., Holtz F. and Adams F. (2014) Kinetic vs. thermodynamic control of degassing of H_2O–S±Cl-bearing andesitic melts. Geochim. Cosmochim. Acta 125, 241–264.

Fiege A., Ruprecht P., Simon A. C., Bell A. S., Göttlicher J., Newville M., Lanzirotti T. and Moore G. (2017) Calibration of Fe XANES for high-precision determination of Fe oxidation state in glasses: Comparison of new and existing results obtained at different synchrotron radiation sources. Am. Mineral. 102, 369–380.

Fortin M. A., Riddle J., Desjardins-Langlais Y. and Baker D. R. (2015) The effect of water on the sulfur concentration at sulfide saturation (SCSS) in natural melts. Geochim. Cosmochim. Acta. 160, 100–116.

Frost, B.R. (1991) Introduction to oxygen fugacity and its petrologic importance. Reviews in Mineralogy and Geochemistry, 25, 1–9.

Gerlach T.M., Delgad, H., McGee K.A., Doukas M.P., Venegas J.J., Cardenas L. (1997) Application of the LI-COR CO2 analyzer to volcanic plumes: a case study, Volcan Popocatepetl, Mexico, June 7 and 10, 1995. J. Geophys. Res. 102, 8005-8019.

Ghiorso M. S. and Evans B. W. (2008) Thermodynamics of Rhombohedral Oxide Solid Solutions and a Revision of the FE-TI Two-Oxide Geothermometer and Oxygen-Barometer. Am. J. Sci. 308, 957–1039.

Goldoff B., Webster J. D. and Harlov D. E. (2012) Characterization of fluor-chlorapatites by electron probe microanalysis with a focus on time-dependent intensity variation of halogens. Am. Mineral. 97, 1103–1115.

Greenwood J.P., Itoh S., Sakamoto N., Warren P., Taylor L., and Yurimoto H. (2011) Hydrogen isotope ratios in lunar rocks indicate delivery of cometary water to the Moon. Nature Geoscience, 4, 79–82.

Harlov D. E. (2015) Apatite: A Fingerprint for Metasomatic Processes. Elements 11, 171–176.

Hauri E.H., Weinreich T., Saal A.E., Rutherford M.C., and Van Orman J.A. (2011) High Pre-Eruptive Water Contents Preserved in Lunar Melt Inclusions: Science, 333, 213–215.

Head E., Lanzirotti A., Newville M. and Sutton S. (2018) Vanadium, sulfur, and iron valences in melt inclusions as a window into magmatic processes: A case study at Nyamuragira volcano, Africa. Geochim. Cosmochim. Acta 226, 149–173.

Hughes J. M. and Rakovan J. F. (2015) Structurally Robust, Chemically Diverse: Apatite and Apatite Supergroup Minerals. Elements 11, 165–170.

Hui H., Peslier A.H., Zhang Y., and Neal C.R. (2013) Water in lunar anorthosites and evidence for a wet early Moon: Nature Geoscience, 6, 177–180.

Huston D. L., Pehrsson S., Eglington B. M. and Zaw K. (2010) The geology and metallogeny of volcanic-hosted massive sulfide deposits: Variations through geologic time and with tectonic setting. Econ. Geol. 105, 571–591.

Jugo P. J. (2009) Sulfur content at sulfide saturation in oxidized magmas. Geology 37, 415–418.

Jugo P. J. (2004) An Experimental Study of the Sulfur Content in Basaltic Melts Saturated with Immiscible Sulfide or Sulfate Liquids at 1300C and 1{middle dot}0 GPa. J. Petrol. 46, 783–798.

Jugo P. J., Luth R. W. and Richards J. P. (2005) Experimental data on the speciation of sulfur as a function of oxygen fugacity in basaltic melts. Geochim. Cosmochim. Acta 69, 497–503.

Jugo P. J., Wilke M. and Botcharnikov R. E. (2010) Sulfur K-edge XANES analysis of natural and synthetic basaltic glasses: Implications for S speciation and S content as function of oxygen fugacity. Geochim. Cosmochim. Acta 74, 5926–5938.

Kelley K. A. and Cottrell E. (2009) Water and the Oxidation State of Subduction Zone Magmas. Science (80-). 325, 605-607.

Keppler H., (1999) Experimental Evidence for the Source of Excess Sulfur in Explosive Volcanic Eruptions: Science, 284, 1652–1654.

Konecke B. A., Fiege A., Simon A. C., Parat F. and Stechern A. (2017a) Co-variability of S^{6+}, S^{4+}, and S^{2-} in apatite as a function of oxidation state: Implications for a new oxybarometer. Am. Mineral. 102, 548–557.

Konecke B.A., Fiege A., Simon A. C. and Holtz F. (2017b) Cryptic metasomatism during late-stage lunar magmatism implicated by sulfur in apatite. Geology 45, 739–742.

Kress V. (1997) Magma mixing as a source for Pinatubo sulphur. Nature 389, 591–593.

Lyons J. I. (1988) Volcanogenic iron oxide deposits, Cerro de Mercado and vicinity, Durango. Econ. Geol. 83, 1886–1906.

Mandeville C. W. (2010) Sulfur: A Ubiquitous and Useful Tracer in Earth and Planetary Sciences. Elements. 6, 75–80.

Manning C. E. (2011) Sulfur Surprises in Deep Geological Fluids. Science (80-). 331, 1018–1019.

Masotta M., Keppler H. and Chaudhari A. (2016) Fluid-melt partitioning of sulfur in differentiated arc magmas and the sulfur yield of explosive volcanic eruptions. Geochim. Cosmochim. Acta. 176, 26–43.

Matjuschkin V., Blundy J. D. and Brooker R. A. (2016) The effect of pressure on sulphur speciation in mid- to deep-crustal arc magmas and implications for the formation of porphyry copper deposits. Contrib. to Mineral. Petrol. 171, 66.

McCormick M. P., Thomason L. W. and Trepte C. R. (1995) Atmospheric effects of the Mt Pinatubo eruption. Nature 373, 399–404.

McCubbin F.M., and Jones R.H. (2015) Extraterrestrial Apatite: Planetary Geochemistry to Astrobiology. Elements, 11, 183–188.

Metrich N. and Mandeville C. W. (2010) Sulfur in Magmas. Elements 6, 81–86.

Miles A. J., Graham C. M., Hawkesworth C. J., Gillespie M. R., Hinton R. W. and Bromiley G. D. (2014) Apatite: A new redox proxy for silicic magmas? Geochim. Cosmochim. Acta. 132, 101–119.

Mills R.D., Simon J.I., Alexander C.M.O., Wang J., and Hauri E.H. (2017) Water in alkali feldspar: The effect of rhyolite generation on the lunar hydrogen budget: Geochemical Perspectives Letters, 3, 115–123.

Parat F., Holtz F. and Streck M. J. (2011) Sulfur-bearing Magmatic Accessory Minerals. Rev. Mineral. Geochemistry. 73, 285–314.

Parker D., Wilson H., Jones P., Christy J. and Folland C. (1996) The Impact of Mount Pinatubo on Worldwide Temperatures. Int. J. Climatol. 16, 487–497.

Parkinson I. J. and Arculus R. J. (1999) The redox state of subduction zones: Insights from arc-peridotites. Chem. Geol. 160, 409–423.

Peng G., Luhr J. J. F. and Mcgee J. J. J. (1997) Factors controlling sulfur concentrations in volcanic apatite. Am. Mineral. 82, 1210–1224.

Righter K., Sutton S. R., Danielson L., Pando K. and Newville M. (2016) Redox variations in the inner solar system with new constraints from vanadium XANES in spinels. Am. Mineral. 101, 1928–1942.

Robinson K.L., and Taylor G.J. (2014) Heterogeneous distribution of water in the Moon: Nature Geoscience. 7, 401–408.

Robock A. (2002) PINATUBO ERUPTION: The Climatic Aftermath. Science (80-). 295, 1242–1244.

Saal A.E., Hauri E.H., Cascio M.L., Van Orman J.A., Rutherford M.C., and Cooper R.F. (2008) Volatile content of lunar volcanic glasses and the presence of water in the Moon's interior. Nature. 454, 192–195.

Simon A. C. and Ripley E. M. (2011) The Role of Magmatic Sulfur in the Formation of Ore Deposits. Rev. Mineral. Geochemistry. 73, 513–578.

Streck M. J. and Dilles J. H. (1998) Sulfur evolution of oxidized arc magmas as recorded in apatite from a porphyry copper batholith. Geology. 26, 523–526.

Treloar P.J., and Colley H. (1996) Variation in F and Cl contents in apatites from magnetite-apatite ores in northern Chile, and their ore-genetic implications: Mineralogical Magazine, 60, 285–301.

Van Hoose, A.E., Streck, M.J., Pallister, J.S., Wälle, M. (2013) Sulfur evolution of the 1991 Pinatubo magmas based on apatite. Journal of Volcanology and Geothermal Research. 257, 72-89.

Wallace P. J. and Carmichael I. S. E. (1994) S speciation in submarine basaltic glasses as determined by measurements of SKα X-ray wavelength shifts. Am. Mineral. 79, 161–167.

Wallace, P.J., Gerlach, T.M. (1994) Magmatic vapor source for sulfur dioxide released during volcanic eruptions: evidence from Mount Pinatubo. Science. 265, 497-499.

Webster J. D. and Piccoli P. M. (2015) Magmatic Apatite: A Powerful, Yet Deceptive, Mineral. Elements. 11, 177–182.

Wetzel D.T., Hauri E.H., Saal, A.E., and Rutherford M.J. (2015) Carbon content and degassing history of the lunar volcanic glasses. Nature Geoscience, 8, 755–758.

Wilke M., Jugo P. J., Klimm K., Susini J., Botcharnikov R., Kohn S. C. and Janousch M. (2008) The origin of S^{4+} detected in silicate glasses by XANES. Am. Mineral. 93, 235–240.

CHAPTER 2: CO-VARIABILITY OF S^{6+}, S^{4+} AND S^{2-} IN APATITE AS A FUNCTION OF OXIDATION STATE – IMPLICATIONS FOR A NEW OXYBAROMETER

Co-authors: Brian Konecke, Adrian Fiege, Adam Simon, Fleurice Parat, and André Stechern

Published in *American Mineralogist* (2017) **102**, 548–557.

2.1 ABSTRACT

In this study, micro X-ray absorption near-edge structures (μ-XANES) spectroscopy at the S *K*-edge was used to investigate the oxidation state of S in natural magmatic-hydrothermal apatite (Durango, Mexico and Mina Carmen, Chile) and experimental apatite crystallized from volatile-saturated lamproitic melts at 1000°C and 300 MPa over a broad range of oxygen fugacities ((log(fO_2) = FMQ, FMQ+1.2, FMQ+3; FMQ = fayalite-magnetite-quartz solid buffer). The data are used to test the hypothesis that S oxidation states other than S^{6+} may substitute into the apatite structure. Peak energies corresponding to sulfate S^{6+} (~2482 eV), sulfite S^{4+} (~2478 eV) and sulfide S^{2-} (~2470 eV) were observed in apatite, and the integrated areas of the different sulfur peaks correspond to changes in fO_2 and bulk S content. Here, multiple tests confirmed that the S oxidation state in apatite remains constant when exposed to the synchrotron beam, at least for up to 1-hour exposure (i.e., no irradiation damages). To our knowledge, this observation makes apatite the first mineral to incorporate reduced (S^{2-}), intermediate

(S^{4+}), and oxidized (S^{6+}) S in variable proportions as a function of the prevailing fO_2 of the system.

Apatite crystallized under oxidizing conditions (FMQ+1.2 and FMQ+3), where the S^{6+}/S_{Total} peak area ratio in the co-existing glass (i.e., quenched melt) is ~1, are dominated by S^{6+} with a small contribution of S^{4+}, whereas apatite crystallizing at reduced conditions (FMQ) contain predominantly S^{2-}, lesser amounts of S^{6+}, and possibly traces of S^{4+}. A sulfur oxidation state versus S concentration analytical line transect across hydrothermally altered apatite from the Mina Carmen iron oxide-apatite (IOA) deposit (Chile) demonstrates that apatite can become enriched in S^{4+} relative to S^{6+}, indicating metasomatic overprinting via a SO_2-bearing fluid or vapor phase. ThiS-XANES study demonstrates that as the fO_2 increases from FMQ to FMQ+1.2 to FMQ+3 the oxidation state of S in igneous apatite changes from S^{2-} dominant to $S^{6+} > S^{4+}$ to $S^{6+} >> S^{4+}$. Furthermore, these results suggest that spectroscopic studies of igneous apatite have potential to trace the oxidation state of S in magmas. The presence of three S oxidations states in apatite may in part explain the non-Henrian partitioning of S between apatite and melt. Our study reveals the potential to use the S signature of apatite to elucidate both oxygen and sulfur fugacity in magmatic and hydrothermal systems.

2.2 INTRODUCTION

Sulfur is the third most abundant volatile in magmatic systems released during volcanic eruptions and degassing processes (cf. Faure, 1986; Métrich and Mandeville, 2010; Mandeville, 2010) and is the fundamental chemical anomaly in arc-related magmatic-hydrothermal porphyry-type ore deposits, which are an important source of Cu, Au, Ag, and Mo (Gustafson and Hunt, 1974; Candela and Piccoli, 2005). A growing

body of data suggests that the oxidation state of S (e.g., S^{2-}, S^{4+}, S^{6+}) plays a fundamental role in controlling ore metal solubilities in parental silicate melts, and partitioning of ore metals between melt and magmatic-hydrothermal ore fluids (Simon and Ripley, 2011). Sulfur oxidation state in silicate melts and magmatic-hydrothermal fluids is intrinsically linked to oxygen fugacity (fO_2), where sulfur is present as sulfate (S^{6+}) and sulfide (S^{2-}) in oxidized and reduced silicate melts, respectively (Jugo et al., 2010). While sulfur in aqueous fluids that exsolved from oxidized and reduced silicate melts exists as sulfite (S^{4+}; SO_2), sulfide (S^{2-}; H_2S; Burgisser et al., 2015) and a trisulfur ion (S_3^-; Pokrovski et al., 2011, 2015).

The mineral apatite—commonly $Ca_5(PO_4)_3(F, Cl, OH)$—is an ubiquitous phase in terrestrial (Webster and Piccoli, 2015) and extraterrestrial (McCubbin and Jones, 2015) magmatic and magmatic-hydrothermal systems and incorporates redox sensitive elements such as Fe, Mn and S. Mainly based on the observation that S-rich (terrestrial) apatite is typically observed in relatively oxidized environments, sulfate (S^{6+}) has been suggested to replace other cations in the apatite structure via several independent substitutions (e.g., Rouse and Dunn, 1982; Liu and Comodi, 1993; Tepper and Kuehner, 1999; Parat et al., 2011b):

$$P^{5+} + Ca^{2+} = S^{6+} + Na^{+} \quad [1]$$

$$2P^{5+} = S^{6+} + Si^{4+} \quad [2]$$

However, apatite crystallized from reduced (sulfide-only) silicate melts has also been shown to contain relatively significant amounts of S. For example, analysis of lunar apatite from the Apollo 12 (sample 12039,42) and 14 (sample 14053,241) missions revealed relatively high S concentrations of >400 μg/g (Boyce et al., 2010; 2014) under

low fO_2 conditions relevant for lunar magmatic systems (e.g., ≤ΔIW+0; Sato et al., 1973), where the $S^{2-}/\Sigma S$ ratio of the system is ~1 (cf. Jugo et al., 2010). Boyce et al. (2010) suggested that the relatively S-rich lunar apatite might indicate the incorporation of S^{2-} into the apatite structure under reducing conditions. If apatite can incorporate S oxidation states other than S^{6+}, and if the S oxidation state and S content in apatite correspond to the S signature of the co-existing melt, then it seems plausible that apatite may reliably record changes in S contents and the S oxidation state during the evolution of magmatic systems. Considering the apatite's ability to crystallize from (silicate) melts and magmatic-hydrothermal fluids (e.g., Lyons, 1988; Peng et al., 1997; Streck and Dilles, 1998; Parat et al., 2004; 2011B; Webster and Piccoli, 2015; Mao et al., 2016), intracrystalline zonation in S content and oxidation state of S-in-apatite may serve as a proxy to reconstruct redox and degassing processes in magmatic and magmatic-hydrothermal environments.

To our knowledge there is no published spectroscopic evidence or constraints on the oxidations states of S, other than S^{6+} (Paris et al., 2001), in apatite over the wide range of fO_2 conditions that prevail in terrestrial magmatic systems (i.e., from fO_2 of FMQ to FMQ+4; Carmichael, 1991; Richards, 2014). Micro XANES spectroscopy at S *K*-edge is an *in situ,* high-resolution, non-destructive and sensitive technique used to probe the electronic and chemical structure (i.e., oxidation state) of S-bearing materials (Paris et al., 2001; Fleet 2005; Jugo et al., 2010). As a result, S-XANES serves as a powerful technique that can be used to investigate the relationship between the oxidation state of S-in-apatite and co-existing melt. In this study, XANES was applied to investigate the S oxidation state in natural apatite as well as in experimentally grown

apatite and co-existing silicate melt, with one potential outcome being the development of a S-in-apatite oxy-sulfo-barometer used to probe the fO_2 and fS_2 of magmatic systems.

2.3 GEOLOGIC BACKGROUND

2.3.1 Mina Carmen apatite

The Mina Carmen iron oxide apatite (IOA) deposit is located ~20 km E of the Atacama fault system in northern Chile (26.346993°S; 70.143110°W). The deposit is hosted within porphyritic andesite of the Los Cerros Florida formation and is dominated by massive iron oxide ore bodies consisting of magnetite and patches of modally minor hematite and minor apatite (Treloar and Colley, 1996). Apatite occurs as coarse-grained crystals up to 50 cm in length within the magnetite matrix and within planar zones of magnetite.

Halogen (F, Cl) and volatile (S) element zonation observed in Carmen apatite (Treloar and Colley, 1996; this study; Appendix Table A1 is interpreted to represent primary magmatic fluorapatite that was subsequently metasomatically overprinted to chlorapatite (ap-X_{Cl} > ap-X_F) by a meteoric H_2O-HCl-rich, HF-poor volatile phase. The presence of secondary REE-phosphate (e.g., monazite; [Ce,La,Th]PO_4) inclusions in Carmen apatite serve as textural evidence for chemical alteration via metasomatism (Harlov et al., 2015; this study). The fluid could be of magmatic (Piccoli and Candela, 2002) or non-magmatic origin (e.g., Barton and Johnson, 1996). Carmen apatite represents the hydrothermal (metasomatized) end-member of the apatite analyzed in this study.

2.3.2 Durango apatite

The IOA deposits near Durango, Mexico are hosted by silicic felsic volcanic rocks within the Carpintero Group (Lyons, 1988). There is general agreement that Durango apatite is magmatic-hydrothermal in origin (Piccoli and Candela, 2002). According to Lyons (1988), the low-Ti IOA deposits formed from a Fe-rich magmatic-hydrothermal fluid that evolved from felsic silicate magma following introduction of CO_2 into the magma from carbonate wall rocks. The initially single phase magmatic-hydrothermal fluid unmixed during decompression into a low-density vapor and higher-density liquid. Strong partitioning of F and Cl into the vapor phase increased the acidity of the vapor and the solubility of Fe as $FeCl_2$, and allowed significant iron oxide mineralization to occur when the vapor vented to the atmosphere and iron oxide precipitated from the Cl-rich liquid. Fluorapatite precipitated from the F-enriched vapor and is abundant in breccias and vapor cavities within the sheeted flows and flow breccia that formed the volcanic dome (Lyons, 1988). An alternative model for the formation of Durango apatite invokes non-magmatic fluids (e.g., Barton and Johnson, 1996).

Durango apatite grains from Cerro de Mercado, Mexico (Young et al., 1969; Lyons 1988), are frequently used as a fluorapatite standard (Jarosewich et al., 1980) that contains ~1,400 ±10% μg/g S and is considered to be chemically homogenous with respect to major elements. However, electron probe microanalysis (EPMA) of a Durango grain orientated where the c-axis is parallel to the incoming electron beam, yielded S totals averaging 875 ± 17 μg/g (1σ standard deviation), indicating homogeneity in terms of S distribution within a single grain, but grain-to-grain variations in S content throughout the deposit.

2.4 METHODS

2.4.1 Crystallization experiments

Apatite crystallization experiments were conducted in rapid quench internally heated pressure vessels (IHPV) at Leibniz University Hannover (LUH), Germany. Gold capsules (3.8 mm O.D., 0.12 mm wall thickness, 10 mm length) were loaded with ~40 mg of mafic starting material (natural lamproite: Vestfjella, Dronning Maud Land, Antarctica; fused overnight at 1,200^{o}C at ~FMQ+1.2 in a gas-mixing furnace; see Table 2.1) and 7-8 wt.% H_2O, in order to promote crystal growth of apatite. This composition was selected for our experiments because preliminary (unpublished) crystallization experiments showed that [1] it crystallizes homogeneous apatite, large enough for XANES and EPMA (~10 μm in diameter) and [2] it can dissolve significant amounts of S even under reducing conditions (cf., thermodynamic model of Liu et al., 2007). Here, the latter is important to reach S contents in apatite that are high enough for accurate EPMA and XANES analyses, even under reducing conditions where the apatite-melt partition coefficient ($D_S^{ap/m}$) for S is less than unity. Assemblages were loaded with either [a] ~1 wt.% pyrrhotite ($Fe_{1-X}S$; Sudbury, Ontario) or [b] ~0.37 wt.% elemental S + ~0.92 wt.% Fe_2O_3 (i.e., an Fe/S ratio corresponding to pyrrhotite) as the source of S, depending on the final fO_2 of the experiment. This procedure of adding S to the systems ensures similar bulk compositions for all runs, while ensuring that the oxidation state of S in the mixture is close to the S oxidation state prevailing at the experimental redox conditions in order to minimize the time required to reach redox equilibrium throughout the sample. It is noted that even without this step, equilibrium in terms of fO_2 between the vessel and the center of the capsule should be reached within a few hours (cf., Fiege et al., 2014).

The capsules were weighed, welded shut and placed in a drying oven (110-120°C) for several hours, then re-weighed to check for water loss. Charges were pressurized to ~60 MPa and rapidly decompressed to verify the mechanical integrity of the capsule. Lamproite experiments were run at 1000°C and 300 MPa for 3-5 days at three different imposed and controlled oxidation states, where fO_2 (log (fO_2/bar) = FMQ, FMQ+1.2, and FMQ+3 (FMQ = fayalite-magnetite-quartz solid buffer). For experiments conducted at FMQ and FMQ+1.2, the fO_2 within the IHPV was controlled by adding H_2 to the Ar-pressure medium and was monitored using a Shaw-membrane, while the most oxidized experiment was intrinsically buffered by the IHPV at FMQ+3 by using pure Ar gas (Berndt et al., 2002; Bell et al., 2011). The experiments were terminated by isobaric rapid quench. The capsules were re-weighed. Capsules revealing loss of weight (i.e., of volatiles/water) during any of the experimental steps were discarded. A list of experiments is provided in Table 2.2.

A photomicrograph of a representative run product is presented in Figure 2.1. Hexagonal apatite grains typically measure ~10 μm in diameter. The major crystalline phases in the quenched experimental run products were identified using an optical microscope and backscatter electron (BSE) imaging. The phase assemblages include apatite, clinopyroxene, amphibole, ±sulfide (e.g., depending on the prevailing fO_2 of the experiment) and co-existing silicate glass.

2.4.2 Natural samples

To better evaluate and apply the new experimental and analytical results presented here, a combination of EPMA, X-ray fluorescence (XRF) mapping and S-XANES was used to characterize natural apatite grains from Durango (Piccoli and

Candela, 2002) and the magmatic-hydrothermal Mina Carmen iron oxide – apatite (IOA) ore deposit (Chile; Treloar and Colley, 1996).

2.5 ANALYTICAL APPROACH

2.5.1 Electron probe microanalysis (EPMA)

Natural apatite from Durango and Mina Carmen, and experimental glasses and apatite were quantitatively characterized by wavelength dispersive EPMA using a CAMECA SX-100 at the University of Michigan (UM, Ann Arbor, USA), at the American Museum of Natural History (AMNH, New York, USA) and at LUH. An acceleration voltage of 15 keV, a beam current of 5-10 nA and a beam size of 5-10 μm beam was used for EPMA of the co-existing silicate glass. Peak counting times of 10 seconds were used for major and trace elements, except 5 seconds for Na and 60-240 seconds for S. An acceleration voltage of 15 keV, a beam current of 10 nA and a beam size of 2 μm was used for all element analysis of apatite. Peak counting times of 20 seconds were used for the major and trace elements, except 5 seconds for F and 60 seconds for S. Precautions were taken to prevent electron beam damage of apatite (e.g., halogen migration; see Goldoff et al., 2012) and glass (e.g., diffusion of Na and Si, Al burn-in; Morgan and London, 2005). During analysis of experimental apatite, both SiO_2 and Al_2O_3 concentrations were monitored for contribution of surrounding glass and mineral phases. Analyses indicating a contribution of the glass were rejected.

2.5.2 Electron backscatter diffraction (EBSD)

The crystallographic orientations of experimental apatite were determined by EBSD using a Zeiss EVO 60 Variable Pressure scanning electron microscope (SEM) at

AMNH. An accelerating voltage of 20 keV was used under a low vacuum (~32 Pa). Samples were fine-polished using colloidal silicon and left uncoated for analysis. The EDAX TEAM software was used for processing and fitting and only results with a confidence index of ≥ 0.2 were considered.

2.5.3 Sulfur X-ray absorption near edge structures spectroscopy (S-XANES)

In situ, S-XANES measurements at the S *K*-edge were conducted at the GSECARS 13-ID-E beamline at Advanced Photon Source (APS), Argonne National Laboratory (USA). The beamline uses a high-flux beam ($\geq 4.5 \times 10^{10}$ photons/second/100 mA/mm^2) that is equipped to produce a high spatial resolution micro-focused 2x1 μm (μ-XANES) beam using Kirkpatrick-Baez (KB) focusing mirrors and can cover an energy range of 2.4 to 28 keV. The energy of the Si(111) channel cut monochromator was calibrated to the 2481.8 (±0.2) eV white line of the spectrum for Scotch™ Brand tape. Energy ranges were collected from 2450 to 2550 eV, with step sizes of 0.1-0.3 eV at the S *K*-edge (2464 to 2484 eV) and 1 eV for the pre-and-post edge regions using 0.5-3 second scan durations per energy step. Step scan durations of 1-3 seconds per energy step were used to analyze natural and experimental apatite to achieve higher S X-ray counts required for high-quality spectra, especially in low-S bearing apatite (e.g., <100 μg/g S).

The European Synchrotron Radiation Facility (ESRF) S *K*-edge XANES spectra database was used to identify the S^{6+} (~2482 eV; anhydrite), sulfite S^{4+} (~2478 eV; sodium sulfite) and sulfide S^{2-} (~2470 eV; pyrrhotite) peak energy positions for the unknowns (see Appendix C). Natural samples were analyzed via S-XANES prior to EPMA, and experimental samples were re-polished extensively (following EPMA) to

remove the upper few μm of each sample that may have been modified by electron beam irradiation damage produced during EPMA (see Wilke et al., 2008).

2.5.4 Glasses: Assessing beam damage systematics

Beam damage to hydrous glasses caused by X-ray irradiation has been observed by Wilke et al. (2008) and requires careful monitoring during analysis, especially for beamlines that use a high-flux X-ray beam such as 13-ID-E at APS. A method similar to the one described by Fiege et al. (2014) was used to measure glasses where several short scan durations (e.g., 0.5 seconds/energy step) were used to analyze the experimental hydrous mafic glasses and the spectra were monitored for beam damage related to photo-reduction effects resulting in the systematic reduction of the S^{6+} peak and subsequent development of a S^{4+} peak (see Appendix Figure A1; Métrich et al., 2002, 2009; Wilke et al., 2008; Jugo et al., 2010). This method has been proven to produce high quality spectra in hydrous glasses with S content of ~50 μg/g S. Whenever possible, spectra exhibiting evidence for beam damage (e.g., systematic photo-reduction of S^{6+} peak to S^{4+}; see Appendix Figure A1; Wilke et al., 2008 and Jugo et al., 2010) were rejected and the remaining spectra were merged. However, the experimental run at FMQ+1.2 was particularly prone to irradiation damage and even the first analysis contains a small but distinct S^{4+} feature, which is marked accordingly in the respective figures (*note:* considering that this peak is growing with exposure time, it is safe to assume that the S in this glass was all S^{6+} prior to XANES analyses; see Results section).

2.5.5 S-XANES spectra correction and peak area integration

The X-ray absorption spectroscopy (XAS) data software analysis package Athena (Ifeffit package; Ravel and Newville, 2005) was used to first merge and subsequently normalize the raw spectra. Normalization of merged raw spectra involves setting the pre-edge and post-edge to 0 and 1, respectively. Merged and normalized spectra of samples with low S contents (e.g., <100 μg/g S) were smoothed in Athena using Gaussian 11 and 4 type filters.

The curve and peak fitting open source software Fityk (Wojdyr, 2010; version 0.9.8) was used for peak area integration analysis of merged, non-smoothed, and corrected spectra. The Fityk software provides information including the [a] peak intensity, [b] integrated peak areas, and [c] peak positions of the Gaussian functions. An exponentially modified Gaussian (EMG) function was used to fit the background to eliminate contribution from the pre-and-post edges. The inflection point of the EMG function was positioned at energies of ~2478-2480 eV for all spectra, and the pre-and-post edges of the EMG function are at 0 and 1, respectively. Gaussian area (e.g., Gaussian-A) functions were used to separately fit the S^{6+}, S^{4+}, S^{2-} and ionization peak(s) (Figure 2.2). The residual of the fitting (i.e., the difference between the fitted and raw spectrum as a function of energy) was used to evaluate the fitting functions at the S *K*-edge (~2468-2484 eV; Figure 2.2).

The peak area ratios of the S^{6+}, S^{4+}, S^{2-} peaks were used to evaluate relative changes in the oxidation state of S in the sample. Since all natural and experimental apatite analyzed in this study contained S^{6+}, the integrated S^{6+}/S_{Total} peak area ratios (e.g., $S_{Total} = (S^{6+} + S^{4+} + S^{2-})$) were used in order to remain comparable between oxidized

(FMQ+3), intermediate (FMQ+1.2) and reduced (FMQ) redox systems. It is stressed that until a calibration using standards with known S^{6+}, S^{4+}, S^{2-} ratios is developed, the S^{6+}, S^{4+}, S^{2-} integrated peak area ratios measured in the samples do not directly correspond to the actual S^{6+}, S^{4+}, S^{2-} ratio in the sample. This integrated peak area ratio fitting approach deviates from the method developed by Jugo et al. (2010), which does not consider the sharp S^{2-} peak, the S^{4+} peak, the ionization peak, and does not apply a background subtraction. Here, the background subtraction is important considering the low integrated intensity of the sulfite peak, and a similar method has proven to be a reliable approach for high precision Fe oxidation state analyses via XANES (e.g., Cottrell et al., 2009; Fiege et al., 2017). The integrated peak area ratio method, as utilized in the current study, allows for peak modeling that is more sensitive to these contributions, where calibration can serve as a consistent and accurate method to quantify the S^{6+}, S^{4+}, and S^{2-} in apatite and co-existing glass (please note the high external precision of our method illustrated in Figures 2.3 and 2.4).

2.5.6 Time series and line transect measurements on Durango apatite

Sulfur XANES line transects and time series were collected on Durango apatite in order to evaluate the susceptibility or resistance of apatite to beam damage (e.g., photo-reduction effects; Wilke et al., 2008; Jugo et al., 2010) during exposure to a relatively high-flux X-ray beam during S-XANES analysis. Time series measurements on Durango fluorapatite using analytical durations ranging from ~2 to 60 minutes per analytical spot produced insignificant variation (e.g., within analytical uncertainty) between the spectra (see Figure 2.3). Thus, irradiation damages resulting in a possible oxidation or reduction of S-in-apatite during the analyses can be ruled out.

Analysis of Durango apatite over a ~3,000 μm line transect (e.g., 100 μm step lengths and 2 scans per step) was performed (approximately parallel to the c-axis) to determine if the oxidation state of S is homogeneous throughout the grain. Following S-XANES analysis, an EPMA line transect (see Appendix A) was performed parallel (within ~25 μm) to the S-XANES analysis to measure possible variability in S concentration along the line transect. Figure 2.4 illustrates that the variability within the integrated S^{6+}/S_{Total} peak area ratios collected during S-XANES analysis is within 10% analytical error and likely reflects the minor compositional heterogeneity with respect to S. It is noted here that significant grain-to-grain variability in S (~900 to ~1400 ppm S) was observed, whereas S^{6+}/S_{Total} peak area ratios remain at a constant value of 0.955 ±0.002 (2σ standard error). Hence, I suggest that Durango apatite is a suitable reference material for S-XANES analyses of (highly oxidized) apatite but should be used with caution as a S concentration standard owing to the approximately 50% variability in measured S contents.

2.5.7 XANES and EPMA line transects measurements on Mina Carmen apatite

A ~40 μm long S-XANES line transect across hydrothermally altered (i.e., metasomatized) apatite from the Mina Carmen IOA deposit (Chile; Treloar and Colley, 1996) was performed to assess S oxidation state in S-rich areas adjacent to volatile-bearing cavities (S-rich areas were located via XRF mapping). The transect was collected near (within ±10-15 μm) a formerly volatile bearing (fluid/vapor) cavity towards the non-metasomatized region of the apatite grain (Figure 2.5). A parallel EPMA line transect was recorded ~10 μm away from the XANES transect to investigate a possible co-variation between S oxidation state and S content in Mina Carmen apatite.

2.6 RESULTS

2.6.1 S oxidation states in Carmen apatite

Combined with an EPMA transect (see Appendix Table A1) parallel to the S-XANES transect, the metasomatized areas of the Mina Carmen apatite show distinct variations in the S-concentration and the integrated S^{6+}/S_{Total} peak area ratios of the S-XANES spectra (Figure 2.6A). The integrated S^{6+}/S_{Total} peak area ratios varied from 0.982 to 0.993 (Figure 2.6B), depending on the proximity to volatile induced alteration of the apatite grain (see Figure 2.5). The EPMA transect reveals a ~2 orders of magnitude increase in S content from the non-metasomatized area of apatite (e.g., <55 μg/g S limit of detection; EPMA) to the metasomatized area of apatite near a volatile-bearing cavity rim (e.g., >2,000 μg/g S; Figure 2.6B), which correlates inversely with the evolution of the S^{6+}/S_{Total} peak area ratios.

2.6.2 XANES results at reduced oxidation state: FMQ

The average XANES spectrum for experimental apatite crystallized from the reduced (LA45-IH1; FMQ) lamproitic glasses exhibit dominant S^{2-} (~2470 eV sharp peak and ~2476 eV broad peak) and S^{6+} (~2482 eV) peaks (Figure 2.7A). The integrated S^{6+}/S_{Total} peak area ratio is 0.168 at FMQ. The reduced lamproitic glass is dominated by S^{2-} based on peaks at ~2470 eV (sharp peak) and ~2476 eV (broad peak).

Here, I highlight an observed influence of the crystallographic orientation of apatite on the S peak area ratios in the S-XANES spectra collected on apatite from the reduced run products (i.e., at FMQ; see Figure 2.8 and discussion section about the crystallographic orientation). Hence, several apatite and co-existing glass spots were

analyzed and merged (prior to baseline removal and intensity normalization) in order to achieve an average spectrum, representative for the bulk S oxidation states within each sample (see also Evans et al., 2014).

2.6.3 XANES results at intermediate oxidation state: FMQ+1.2

The XANES spectra for experimental apatite that crystallized from a lamproitic glass at intermediate redox conditions (FMQ+1.2) reveal a dominant sulfate peak (~2482 eV) and a minor sulfite (S^{4+}; ~2478 eV) peak, where the integrated S^{6+}/S_{Total} peak area ratio is 0.958 at FMQ+1.2 (LA45-IH7; Figure 2.7B).

The S oxidation state of lamproitic glass from the intermediate (FMQ+1.2) experiment is dominated by S^{6+} by peak at ~2482 eV but also shows a minor sulfite (S^{4+}; ~2478 eV) peak (Figure 2.7B). To demonstrate that beam-induced modification of the measured oxidation state of S in the glass causes the formation of the sulfite peak, the scanning time was intentionally increased from 0.5 to 1 second/energy step during analysis of the hydrous lamproitic glass from the intermediate fO_2 experiments. While using a scanning time of 1 second/energy step, the development and growth of the S^{4+} peak coupled with the simultaneous systematic depletion of the S^{6+} peak was observed during analysis, demonstrating the effects of beam damage due to X-ray irradiation (see Wilke et al., 2008). Thus, the XANES analyses indicate that S^{6+} is most probably the only, or at least the dominant, S species in the quenched glass at intermediate redox conditions (FMQ+1.2).

2.6.4 XANES results at oxidized oxidation state: FMQ+3

Dominant sulfate (~2482 eV) and minor sulfite (S^{4+}; ~2478 eV) peaks are observed in the spectra of apatite crystallized from the oxidized (FMQ+3) lamproitic glass (Figure 2.7C), where the integrated S^{6+}/S_{Total} peak area ratio was 0.963 at FMQ+3.The S oxidation state of lamproitic glass from the oxidized (FMQ+3) experiment is dominated by S^{6+} based on the strong peak at ~2482 eV and the absence of S^{2-} peaks (i.e., ~2470 eV sharp peak and ~2476 eV broad peak; Figure 2.7C). Under short scanning times (0.5 second/energy step), the presence or systematic growth of a S^{4+} peak at ~2478 eV with analytical time was not observed; whereas increasing the scanning time to 1 second/scan would probably result in beam damage similar to that observed in the intermediate glass (LA45-IH7; Figure 2.7B).

2.7 DISCUSSION

2.7.1 S oxidation state in apatite as a function of fO_2

Sulfur XANES analyses of experimental apatite crystallized over a range of fO_2 conditions (FMQ, FMQ+1.2 and FMQ+3) reveals variability in S oxidation states in apatite as a function of the redox conditions of the system. To our knowledge, these data represent the first S-XANES measurements demonstrating the substitution of S^{2-}, S^{4+} and S^{6+} in apatite or in any other naturally occurring mineral. Our observations are in agreement with recent quantum mechanical calculations that assess incorporation of S^{2-}, S^{4+} and S^{6+} in apatite (Kim et al., 2017).

The co-variation of the S content and the S oxidation state observed near a fluid cavity in Mina Carmen apatite (Figure 2.6B) is most plausibly explained by the

metasomatic enrichment of S-in-apatite via reaction with a S-bearing (e.g., SO_2) fluid or vapor (Harlov, 2015). Here, the increasing S^{4+} fraction (decreasing S^{6+}/S_{Total}) indicates [1] that the fluid was relatively oxidized (high SO_2/H_2S ratio) and [2] that the S oxidation state remains to some extent unchanged as S partitions from an oxidized fluid (SO_2) into an apatite (SO_3^{2-}; see discussion below about substitution mechanisms). There is likely no effect on the oxidation state of the fluid during the interaction with apatite, considering the elevated S contents expected of such fluids (e.g., Zajacz et al., 2012; Burgisser et al., 2015; Fiege et al., 2015).

2.7.2 Crystallographic orientation controls on S oxidation states in apatite

A co-variation of S oxidation states (mainly S^{6+} and S^{2-}) is observed in the apatite crystallized from the reduced (FMQ) lamproitic melts (Figure 2.8). These relative changes in S^{6+} and S^{2-} peak intensities are interpreted to be a function of the orientation of the crystal (e.g., parallel or perpendicular to the c-axis). Crystallographic orientation effects, i.e., variation in speciation as a function of crystallographic orientation, have been observed during Fe XANES analysis in various minerals (e.g., pyroxenes, amphiboles, micas and biotite; Dyar et al., 2002; Evans et al., 2014). This interpretation is entirely consistent with theoretical findings made by Kim et al. (2017), suggesting the sulfide (probably as S^{2-}) sits on the column anion site whereas sulfate (SO_4^{2-}) and sulfite (SO_3^{2-}) are probably positioned within the phosphate (PO_4^{3-}) anion site. Moreover, a minor contribution of S^{4+} is indicated in spectra that are rather S^{6+} dominated and S^{2-} deficient (compare Figure 2.8C and 8D). Here, the absence of a S^{4+} peak in S^{2-} dominant spectra is probably related to the relative abundance of S^{2-} versus S^{4+}, i.e., the S^{2-} peaks likely obscure the minor S^{4+} peak in most spectra.

Although crystallographic orientation effects were not observed in the apatite crystallizing from the intermediate (FMQ+1.2) and oxidized melts (FMQ+3), the possibility of orientation effects cannot be excluded, considering that the S^{4+} contribution to the spectra is small and possible changes in the S^{6+}/S_{Total} peak area ratio related to crystal orientation might be below the limit of detection.

Electron backscatter diffraction (EBSD) was performed to determine the orientation of the experimental apatite in the reduced samples (LA45-IH1) following XANES analysis (e.g., to avoid potential beam damage from electron beam irradiation). Due to the complexity of the experimental (e.g., high crystallinity) samples, we were unable to positively correlate the measured crystallographic orientation of apatite crystals via EBSD with the apatite crystals measured with S-XANES. However, EBSD generally confirmed that elongated apatite were analyzed with the electron beam being nearly perpendicular to the c-axis, and hexagonal shaped apatite were measured with the beam being approximately parallel to the c-axis (Figure 2.8). Hence, our results provide first-order evidence that S^{2-} and S^{6+} are incorporated into different locations within the apatite structure. While it is impossible to speculate about the possible location of S^{2-}, S^{4+} and S^{6+} within the apatite structure based on our analyses, we emphasize that Kim et al. (2017) came to the same conclusion by ab-initio modeling of the apatite structure, suggesting that S^{2-} is positioned in the (F^-, Cl^-, OH^-) anion site, while S^{4+} and S^{6+} are positioned in the phosphate site.

2.7.3 S-in-apatite substitution mechanisms

Several individual substitution mechanisms for S^{6+} have been proposed (cf., Parat et al., 2011). In REE-free systems, Rouse and Dunn (1982) and Parat et al. (2011a and

2011b) proposed exchange reactions involving Si and S, where: $2P^{5+} \Leftrightarrow S^{6+} + Si^{4+}$. Parat and Holtz (2005) performed apatite crystallization experiments in REE-free systems and confirmed the exchange reactions involving Na and S (Liu and Comodi, 1993; Parat and Holtz, 2004), where: $P^{5+} + Ca^{2+} \Leftrightarrow S^{6+} + Na^{+}$. In natural systems, which generally contain REEs, they can be incorporated via coupled exchange reactions (Streck and Dilles 1998; Tepper and Kuehner 1999; Parat et al. 2008; Pan and Fleet, 2002) such as:

$$2Ca^{2+} \Leftrightarrow REE^{3+} + Na^{+} \quad [3]$$

$$P^{5+} + Ca^{2+} \Leftrightarrow REE^{3+} + Si^{4+} \quad [4]$$

Sulfur XANES analyses (this study) indicate that S^{6+} and S^{4+} co-exist in experimental apatite that crystallized from intermediate to oxidized conditions (e.g., FMQ+1.2 to 3). Considering the $2P^{5+} \Leftrightarrow S^{6+} + Si^{4+}$ substitution, a mechanism involving:

$$2P^{5+} \Leftrightarrow S^{6+} + S^{4+} \quad [5]$$

is most plausible and consistent with computational results from Kim et al. (2017). A plausible explanation for the incorporation of S^{4+} into apatite is via a local redox reaction involving the reduction of S^{6+} to S^{4+}, where:

$$SO_4^{2-}{}_{(melt)} \Leftrightarrow SO_3^{2-}{}_{(apatite)} + \tfrac{1}{2}\, O_{2\,(melt)} \quad [6]$$

This redox reaction scenario is favored since [a] it does not require a significant contribution of S^{4+} from the melt and [b] S^{4+} incorporation into the apatite structure may serve as a mechanism to charge balance the incorporation of S^{6+} (see Kim et al., 2017).

Notably, for Fe-free and Fe-poor (≤ 1.6 wt.% FeO) silicic melts, Métrich et al. (2009) observed a minor S^{4+} peak, which is probably unrelated to irradiation effects. The authors suggest that S^{4+} is not stable in the glass structure, but stable in melts at elevated P-T. Hence, a possible but unlikely scenario (considering the elevated Fe contents in the

lamproitic melt) could be that the S oxidation state in apatite indeed reflects the oxidation state in the melt from which apatite crystallizes.

Although the presence of S^{2-} in natural apatite has never been directly measured spectroscopically, Henning et al. (2000) successfully synthesized calcium sulfoapatite ($Ca_5(PO_4)_3S$) and argued that sulfoapatite are not capable of absorbing H_2S into their structure the way that oxyapatite can absorb H_2O at elevated temperatures, owing to the position of the sulfide (S^{2-}) ion. This observation, which is in good agreement with the S-XANES spectra of apatite crystallizing under reducing conditions (FMQ; Figure 2.7A), provides an important constraint on the substitution mechanisms associated with S^{2-} in the apatite structure; e.g., under reducing conditions, S^{2-} is likely more favorable within the apatite structure compared to HS^- (Henning et al., 2000; Kim et al., 2017). Notably, in the reduced experimental systems (FMQ; this study), apatite is S-bearing (up to ~320 µg/g S) and is characterized stoichiometrically as hydroxyl-fluorapatite (ap-X_{OH} > ap-X_F >> ap-X_{Cl}). The results of Kim et al. (2017) also suggest that the incorporation of S^{2-} plus a lattice vacancy favors 2Cl > 2OH > 2F, suggesting that S^{2-} is increasingly stable when: ap-X_{Cl} > ap-X_{OH} > ap-X_F.

Finally, we speculate that the increasing S^{4+} fraction (decreasing S^{6+}/S_{Total}) observed in Mina Carmen apatite indicates that a sulfate-sulfite coupled substitution mechanism is dominate during hydrothermal alteration of apatite by a relatively oxidizing fluid/vapor. Here, a reaction involving: $2PO_4^{3-}{}_{(apatite)} + 2SO_{2\,(fluid)} + 1½\ O_{2\,(fluid)} \Leftrightarrow SO_4^{2-}{}_{(apatite)} + SO_3^{2-}{}_{(apatite)} + 2PO_4^{3-}{}_{(fluid)}$, plausibly explains the incorporation of S^{6+} and S^{4+} in apatite during reaction with a SO_2-bearing fluid phase.

2.8 IMPLICATIONS

The oxidation state of S as a function of fO_2 plays a crucial role in controlling the solubilities of S and (chalcophile) ore metals in silicate melts as well as the partitioning of S and (chalcophile) ore metals between silicate melts and magmatic-hydrothermal fluids. We emphasize that the strong dependence of the S oxidation state in apatite as a function of fO_2 is also coupled with changing S contents in the apatite and the co-existing melt, resulting in a complex correlation between [a] apatite-melt (or fluid) partitioning, [b] redox conditions and [c] the melt and/or fluid composition. The presence of three S oxidation states in apatite may in part, explain the non-Henrian distribution behavior of S between apatite and co-existing melt (Parat et al., 2011).

Upon calibration over a range of geologically relevant T-P-X-fO_2-fS_2, our study reveals that the oxidation state of S-in-apatite may serve as a powerful geochemical tool that will allow geoscientists to quantify the fO_2 and fS_2 conditions of ore-forming magmatic-hydrothermal and hydrothermal systems. However, the key for a robust calibration will be the determination of incorporation mechanisms for S^{6+}, S^{4+}, and S^{2-} in apatite, where the chemistry of the host apatite may introduce other controlling parameters that complicate the calibration (Kim et al., 2017).

Table 2.1: Starting mafic (lamproite) composition

Wt.%	Lamproite AL/KB6-98*
SiO_2	40.13
TiO_2	4.37
Al_2O_3	8.57
FeO	8.75
MnO	0.2
MgO	9.21
CaO	16.24
Na_2O	0.5
K_2O	5.29
P_2O_5	3.81
H_2O	n.d.
F	n.d.
Total	97.07

Analyzed by XRF at LUH; n.d.: not determined. *Lamproite sample investigated by Luttinen et al. (2002); see their work for geological and analytical details. Loss of ignition (LOI) at 1,200°C = 8.40%.

Table 2.2: Experimental conditions

Run name	T(°C)	Pressure (MPa)	fO_2 (FMQ)	Duration (days)	S added (wt. %)
LA45-IH1	1,000	300	0	3	1.0 (po.)
LA45-IH7	1,000	300	1.2	5	1.0 (po.)
LA45-IH13	1,000	300	3	5	1.0 (*po.)

*~0.35 wt.% S (elemental) + ~0.92 wt.% Fe_2O_3, where the Fe/S ratio corresponds to po.

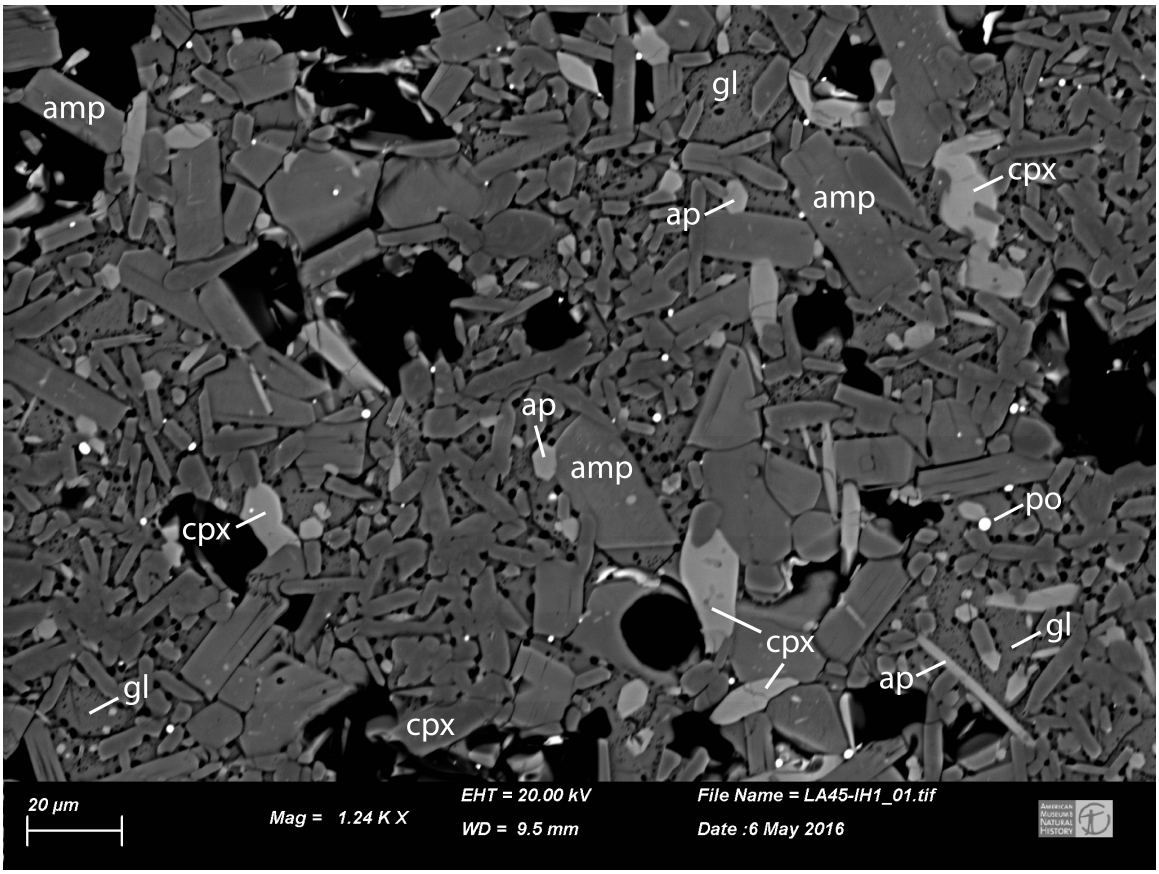

Figure 2.1: Backscatter electron (BSE) image of a representative area of experimental run product LA45-IH1. The run product includes: quenched glass (gl), apatite (ap), clinopyroxene (cpx), amphibole (amp), and ± iron sulfide (po; e.g., depending on the fO_2 of the system). Scale bar represents 20 µm.

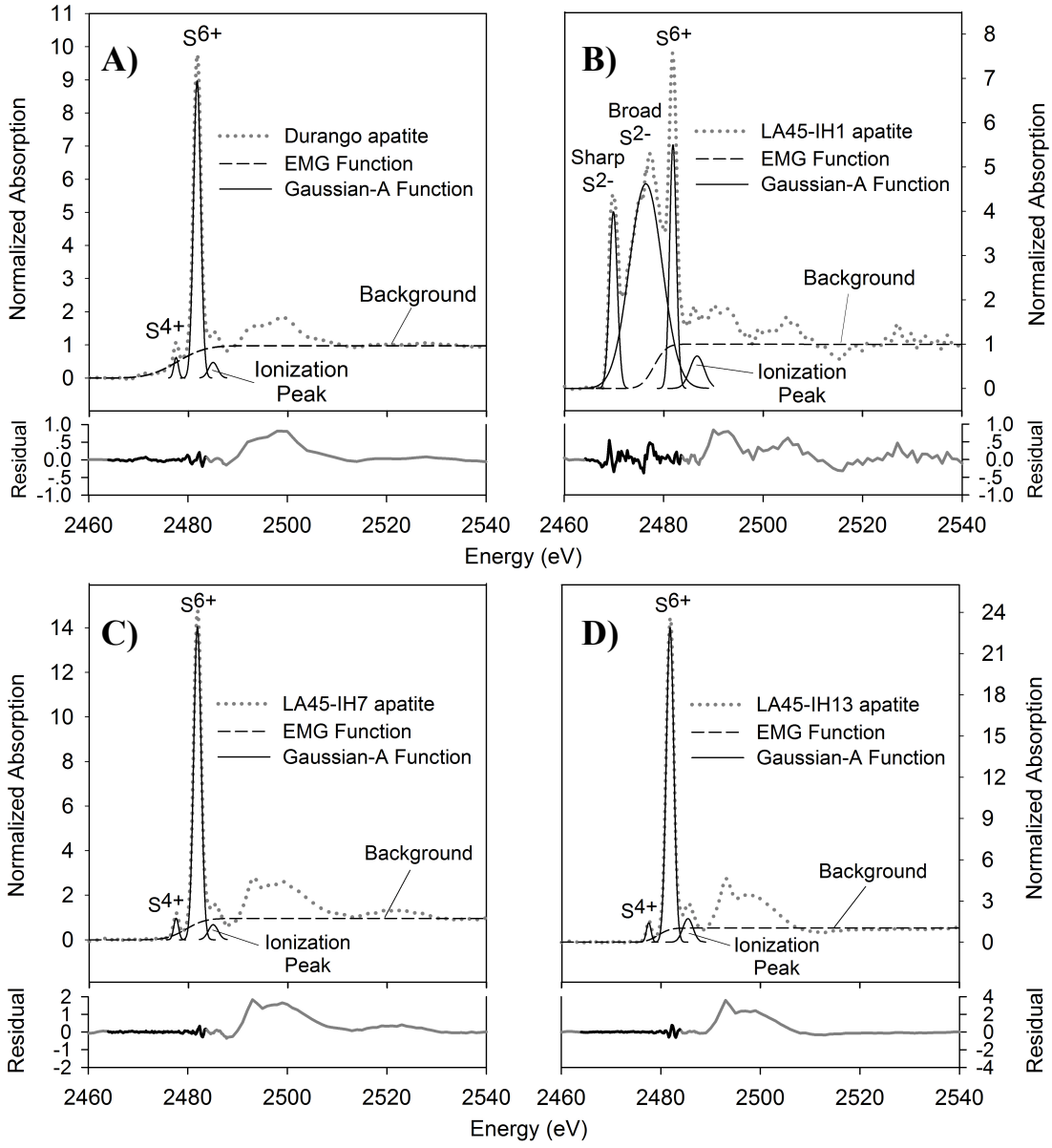

Figure 2.2 (A-D): Illustration of the Fityk peak fitting procedure for selected S-XANES spectra (merged; dotted lines) collected on apatite. (A) Durango apatite; (B) LA45-IH1 apatite (FMQ); (C) LA45-IH7 apatite (FMQ+1.2); (D) LA45-IH13 apatite (FMQ+3). Gaussian-A functions (solid lines) were used to fit the S^{6+}, S^{4+}, S^{2-} and ionization peaks and exponentially modified Gaussian (EMG) functions were used to fit the background (dashed line). The integrated peak area ratios of the S^{6+}, S^{4+} and S^{2-} peaks were used in order to evaluate relative changes in S-oxidation state in the sample, where: $S_{Total} = (S^{6+} + S^{4+} + S^{2-})$. The plots below A-D show the residual of the fitting when subtracting from the raw spectrum as a function of energy. The black part of the lines represents the fitting at the S K-edge (~2468-2484 eV), whereas the gray lines represent the non-fitted pre- and-post edge.

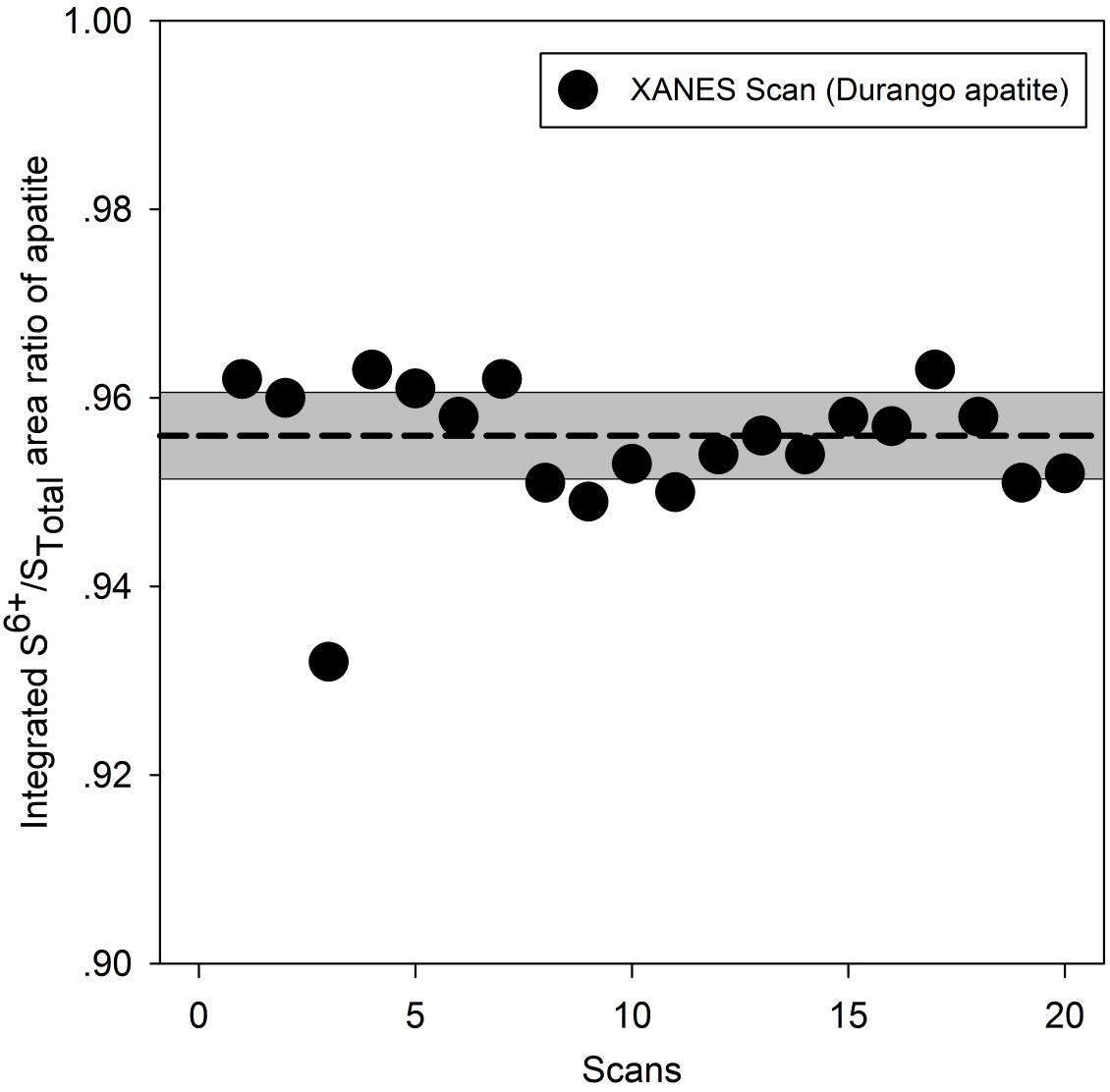

Figure 2.3: One-hour S-XANES time-series on Durango apatite to test for possible irradiation damages potentially resulting in an oxidation or reduction of sulfur in apatite during analysis. Twenty, 3-minute long scans were taken on the same analytical spot and the integrated S^{6+}/S_{Total} peak area ratios were evaluated for significant deviation (e.g., within ±1σ standard deviation; gray box). The average (dashed line) integrated S^{6+}/S_{Total} peak area ratio = 0.956 ±0.002 (2σ standard error). The determination of the integrated S^{6+}/S_{Total} peak area ratios is described in the analytical approach section.

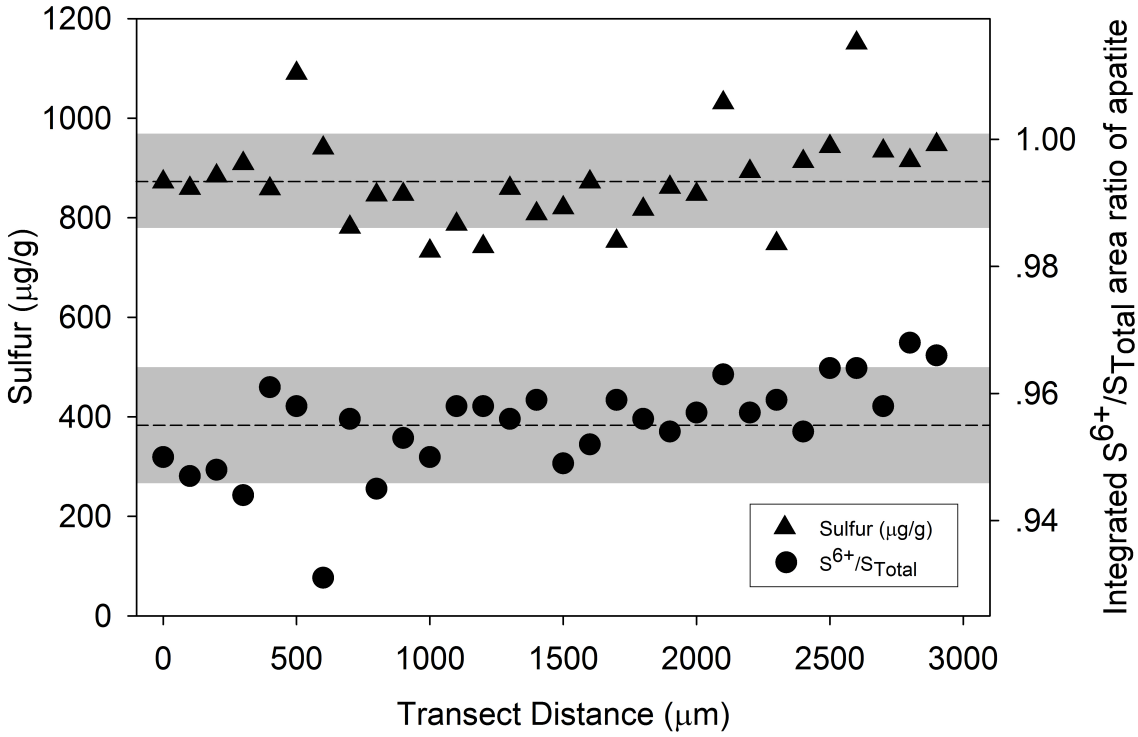

Figure 2.4: EPMA (triangles) and S-XANES (circles) line transect (~3,000 μm; rim to rim) on a grain of Durango apatite that was orientated approximately parallel to the c-axis. The EPMA and S-XANES line transects were performed parallel to each other within ~50 μm distance. The average S content, 875 ± 17 μg/g (1σ standard deviation), is ~50% lower than published values (Young et al., 1969) and may reflect either grain-to-grain heterogeneity (see main text for discussion). The gray boxes represent 1σ standard deviation of the average for each analysis. The average integrated S^{6+}/S_{Total} peak area ratio = 0.955 ±0.002 (2σ standard error).

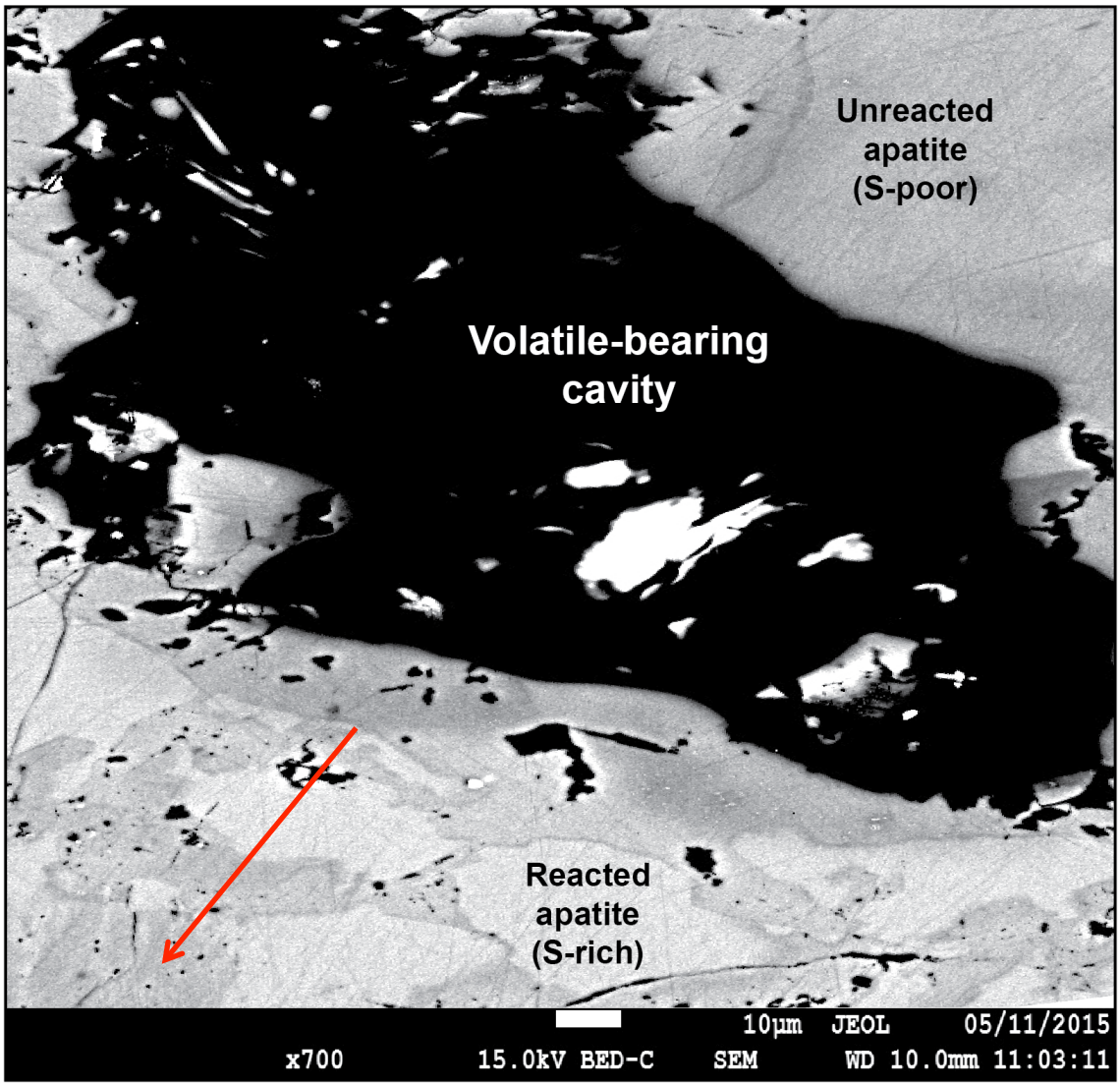

Figure 2.5: Backscatter electron (BSE) image of the volatile bearing cavity region of the Mina Carmen apatite. The reacted (e.g., metasomatized) regions are denoted by the medium gray, while the un-metasomatized the darker gray regions. The red arrow indicates the approximate location (within ±10-15 µm) of the EPMA (See Appendix Table A1) and XANES transects.

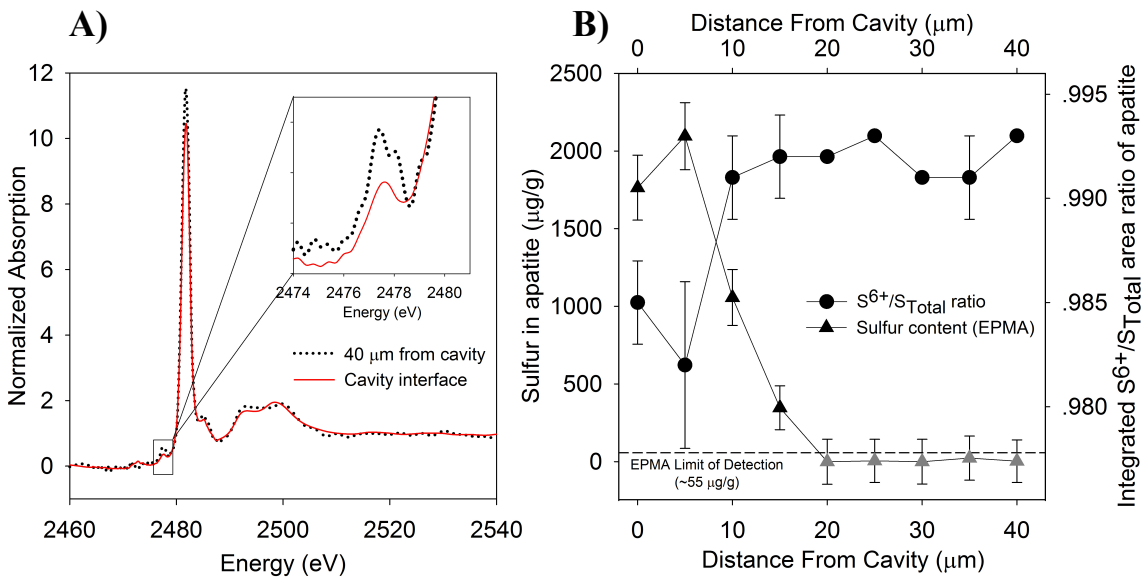

Figure 2.6 (A-B): Sulfur oxidation states and contents in Carmen apatite. (A) S-XANES spectra of Carmen apatite. The red solid line denotes the XANES scan at the edge of the volatile cavity (e.g., metasomatized region; see Figure 2.5) and the black dotted line from the scan ~40 μm away from the cavity (non-metasomatized region). (B) S-XANES and EPMA transect of Carmen apatite from the S-rich region near the cavity into the non-metasomatized, S-poor region. The black dashed line represents the EPMA limit of detection of ~55 μg/g. The gray triangles represent EPMA spot analysis below limit of detection. Error bars are reported in 2σ standard error.

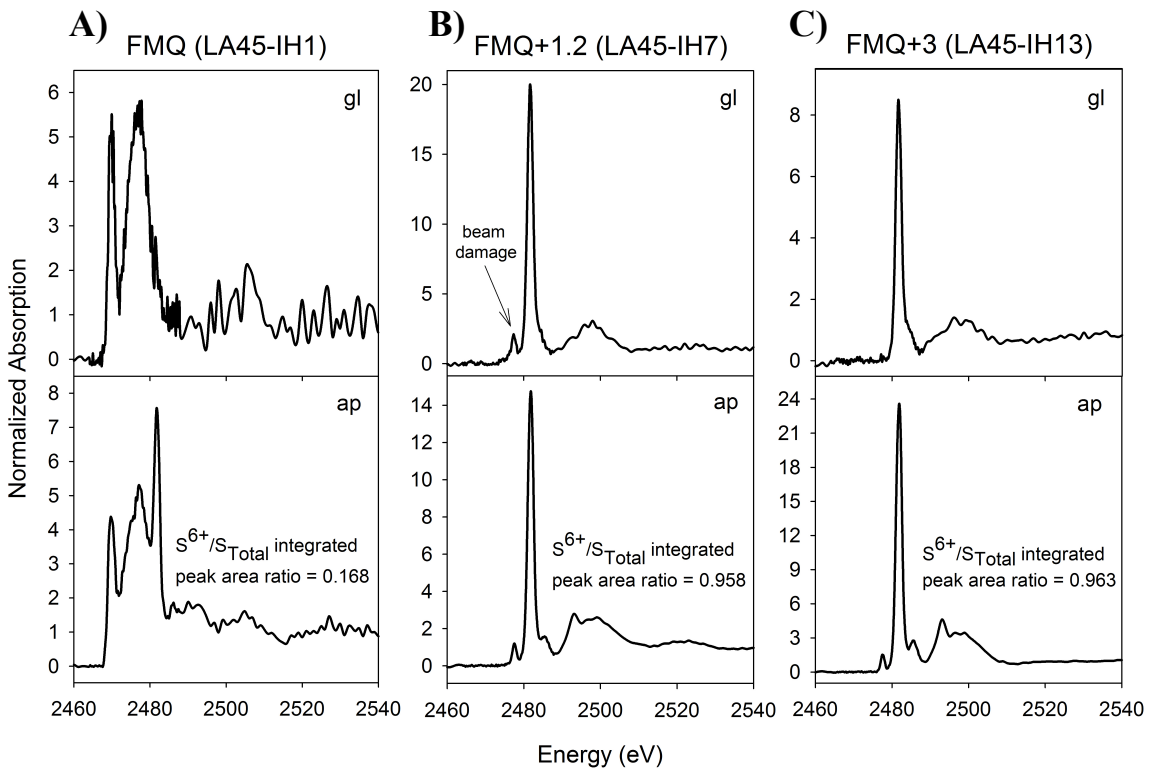

Figure 2.7 (A-C): S-XANES analysis of quenched glass (gl; top) and apatite (ap; bottom) from experiments performed at different fO_2 conditions: (A) FMQ, (B) FMQ+1.2 and (C) FMQ+3. The presented spectra are merged spectra, whereas spectra indicating beam damage (only applicable for glasses) were excluded. (A) Under reducing redox conditions (FMQ; LA45-IH1), only S^{2-} was observed in the co-existing glass, while S^{6+} and S^{2-} (and possibly S^{4+}; see Figure 2.8) were observed in apatite. (B-C) Intermediate and oxidizing redox conditions (e.g., fO_2=FMQ+1.2 and FMQ+3, LA45-IH7 and IH13, respectively) revealed S^{6+} and S^{4+} co-existing in apatite that crystallized under intermediate-oxidized redox conditions. Beam damage was observed even for the first spectrum collected on one spot on the intermediate glass (B; FMQ+1.2), resulting in the immediate formation of S^{4+}. However, the intermediate glass is interpreted to be fully oxidized (all S^{6+}) prior to XANES analyses (see main text). All S in the oxidized glass (C; FMQ+3) is present as S^{6+}.

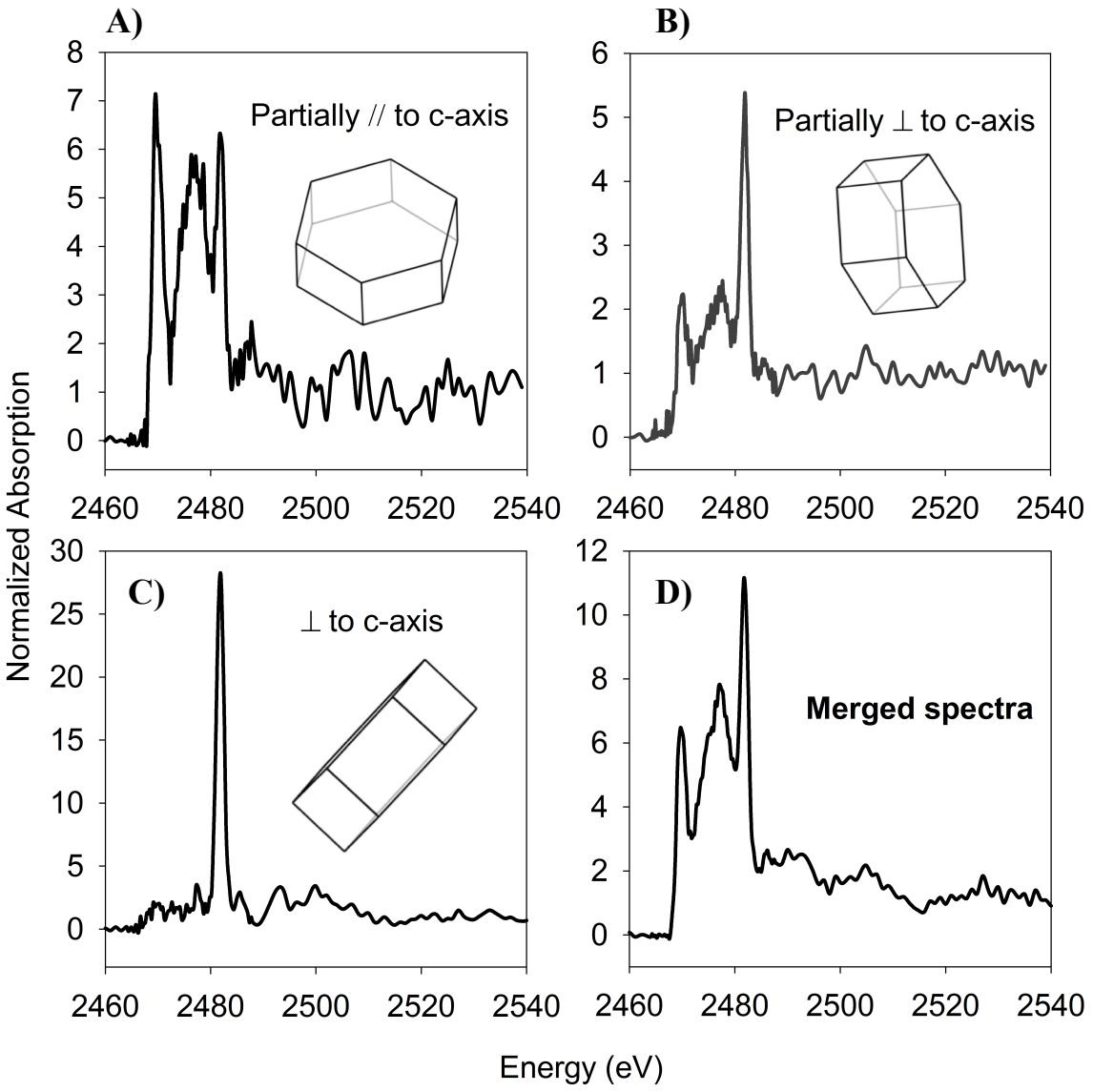

Figure 2.8 (A-D): S-XANES spectra for apatite crystallized from reduced lamproitic melt (LA45-IH1; FMQ) and separated by their perceived orientation relative to the surface. (A) Partially parallel c-axis; (B) partially perpendicular to c-axis; (C) perpendicular to c-axis; and (D) merged spectra of all apatite measured in the sample. Crystal geometries were perceived optically during XANES analysis and due to the complexity of the sample; the crystal orientations could only be correlated using EBSD. The approximate qualitative interpretation of the orientation made during the XANES sessions was generally confirmed by subsequent EBSD analyses (elongated crystals are measured ~perpendicular to c-axis; hexagonal shaped crystals were measured ~parallel to c-axis); see main text for details.

2.9 REFERENCES

Barton, M.D., and Johnson, D.A. (2000) Alternative brine sources for Fe-oxide (Cu-Au) systems: Implications for hydrothermal alteration and metals: Hydrothermal iron oxide copper-gold and related deposits a global perspective. Australian Mineral Foundation, Glenside, South Australia, 43–46.

Bell, A.S., and Simon, A. (2011) Experimental evidence for the alteration of the Fe3+/ΣFe of silicate melt caused by the degassing of chlorine-bearing aqueous volatiles. Geology, 39, 499–502.

Berndt, J., Liebske, C., Holtz, F., Freise, M., Nowak, M., Ziegenbein, D., Hurkuck, W., and Koepke, J. (2002) A combined rapid-quench and H_2 –membrane setup for internally heated pressure vessels: Description and application for water solubility in basaltic melts. American Mineralogist, 87, 1717–1726.

Boyce, J.W., Liu, Y., Rossman, G.R., Guan, Y., Eiler, J.M., Stolper, E.M., and Taylor, L.A. (2010) Lunar apatite with terrestrial volatile abundances. Nature, 466, 466–9.

Boyce, J.W., Tomlinson, S.M., McCubbin, F.M., Greenwood, J.P., and Treiman, a H. (2014) The lunar apatite paradox. Science (New York, N.Y.). 344, 400–2.

Burgisser, A., Alletti, M., and Scaillet, B. (2015) Simulating the behavior of volatiles belonging to the C–O–H–S system in silicate melts under magmatic conditions with the software D-Compress. Computers & Geosciences, 79, 1–14.

Candela, P., and Piccoli, P. (2005) Magmatic Processes in the Development of Porphyry-Type Ore Systems. Economic Geology, 25–37.

Carmichael, I.S.E. (1991) The redox states of basic and silicic magmas: a reflection of their source regions? Contributions to Mineralogy and Petrology, 106, 129–141.

Dyar, M.D., Gunter, M.E., Delany, J.S., Lanzarotti, A.A., and Sutton, S.R. (2002) Systematics in the structure and XANES spectra of pyroxenes, amphiboles, and micas as derived from oriented single crystals. Canadian Mineralogist, 40, 1375–1393.

Evans, K.A., Dyar, M.D., Reddy, S.M., Lanzirotti, A., Adams, D.T., and Tailby, N. (2014) Variation in XANES in biotite as a function of orientation, crystal composition, and metamorphic history. American Mineralogist, 99, 443–457.

Faure, G. (1986) Principles of Isotope Geology. John Wiley and Sons, New York, 589.

Fiege, A., Behrens, H., Holtz, F., and Adams, F. (2014) Kinetic vs. thermodynamic control of degassing of H_2O–S±Cl-bearing andesitic melts. Geochimica et Cosmochimica Acta, 125, 241–264.

Fiege, A., Holtz, F., Behrens, H., Mandeville, C.W., Shimizu, N., Crede, L.S., and Göttlicher, J. (2015) Experimental investigation of the S and S-isotope distribution between H_2O–S±Cl fluids and basaltic melts during decompression. Chemical Geology, 393-394, 36–54.

Fiege A., Ruprecht P., Simon A., Bell A., Göttlicher J., Newville M., Lanzirotti T., Moore G. (2016) Calibration of Fe XANES for high-precision determination of Fe oxidation state in glasses: Comparison of results obtained at different synchrotron radiation sources. American Mineralogist, 102, 548-557.

Fleet, M.E. (2005) XANES spectroscopy of sulfur in earth materials. The Canadian Mineralogist, 43, 1811–1838.

Goldoff, B., Webster, J.D., and Harlov, D.E. (2012) Characterization of fluor-chlorapatites by electron probe microanalysis with a focus on time-dependent intensity variation of halogens. American Mineralogist, 97, 1103–1115.

Gustafson, L.B., and Hunt, J.P. (1975) The porphyry copper deposit at El Salvador, Chile. Economic Geology, 70, 857–912.

Harlov, D.E. (2015) Apatite: A Fingerprint for Metasomatic Processes. Elements, 11, 171–176.

Henning, P.A., Adolfsson, E., and Grins, J. (2000) The chalcogenide phosphate apatites $Ca_{10}(PO_4)_6S$, $Sr_{10}(PO_4)_6S$, $Ba_{10}(PO_4)_6S$ and $Ca_{10}(PO_4)_6Se$. Zeitschrift für Kristallographie - Crystalline Materials, 215, 105110.

Jarosewich, E., Nelen, J.A., and Norberg, J.A. (1980) Reference samples for electron microprobe analysis. Geostandards Newsletter, 4, 43–47.

Jugo, P.J., Wilke, M., and Botcharnikov, R.E. (2010) Sulfur K-edge XANES analysis of natural and synthetic basaltic glasses: Implications for S speciation and S content as function of oxygen fugacity. Geochimica et Cosmochimica Acta, 74, 5926–5938.

Kim, Y.J., Konecke, B., Fiege, A., Simon, A., and Becker, U. (2017) An ab-initio study of the energetics and geometry of sulfide, sulfite, and sulfate incorporation into apatite: The thermodynamic basis for using this system as an oxybarometer. American Mineralogist, v. 102, 1646–1656.

Liu, Y., and Comodi, P. (1993) Some aspects of the crystal-chemistry of apatites. Mineralogical magazine, 57, 709–719.

Liu, Y., Samaha, N.-T., and Baker, D.R. (2007) Sulfur concentration at sulfide saturation (SCSS) in magmatic silicate melts. Geochimica et Cosmochimica Acta, 71, 1783–1799.

Lyons, J.I. (1988) Volcanogenic iron oxide deposits, Cerro de Mercado and vicinity, Durango. Economic Geology, 83, 1886–1906.

Mandeville, C.W. (2010) Sulfur: A Ubiquitous and Useful Tracer in Earth and Planetary Sciences. Elements, 6, 75–80.

Mao, M., Rukhlov, A.S., Rowins, S.M., Spence, J., and Coogan, L.A. (2016) Apatite Trace Element Compositions: A Robust New Tool for Mineral Exploration. Economic Geology, 111, 1187–1222.

McCubbin, F.M., and Jones, R.H. (2015) Extraterrestrial Apatite: Planetary Geochemistry to Astrobiology. Elements, 11, 183–188.

Métrich, N., Bonnin-Mosbah, M., Susini, J., Menez, B., and Galoisy, L. (2002) Presence of sulfite (SIV) in arc magmas: Implications for volcanic sulfur emissions. Geophysical Research Letters, 29, 4–7.

Métrich, N., Berry, A.J., O'Neill, H.S.C., and Susini, J. (2009) The oxidation state of sulfur in synthetic and natural glasses determined by X-ray absorption spectroscopy. Geochimica et Cosmochimica Acta, 73, 2382–2399.

Metrich, N., and Mandeville, C.W. (2010) Sulfur in Magmas. Elements, 6, 81–86.

Morgan, G., and London, D. (2005) Effect of current density on the electron microprobe analysis of alkali aluminosilicate glasses. American Mineralogist, 90, 1131–1138.

Pan, Y., and Fleet, M.E. (2002) Compositions of the Apatite-Group Minerals: Substitution Mechanisms and Controlling Factors. Reviews in Mineralogy and Geochemistry, 48, 13–49.

Peng, G., Luhr, J., and McGee, J. (1997) Factors controlling sulfur concentrations in volcanic apatite. American Mineralogist, 82, 1210–1224.

Parat, F., and Holtz, F. (2004) Sulfur partitioning between apatite and melt and effect of sulfur on apatite solubility at oxidizing conditions. Contributions to Mineralogy and Petrology, 147, 201–212.

Parat, F., and Holtz, F. (2005) Sulfur partition coefficient between apatite and rhyolite: The role of bulk S content. Contributions to Mineralogy and Petrology, 150, 643–651.

Parat, F., Holtz, F., and Feig, S. (2008) Pre-eruptive conditions of the Huerto Andesite (Fish canyon system, San Juan volcanic field, Colorado): Influence of volatiles (C-O-H-S) on phase equilibria and mineral composition. Journal of Petrology, 49, 911–935.

Parat, F., Holtz, F., and Klügel, A. (2011a) S-rich apatite-hosted glass inclusions in xenoliths from La Palma: constraints on the volatile partitioning in evolved alkaline magmas. Contributions to Mineralogy and Petrology, 162, 463–478.

Parat, F., Holtz, F., and Streck, M.J. (2011b) Sulfur-bearing Magmatic Accessory Minerals. Reviews in Mineralogy and Geochemistry, 73, 285–314.

Paris, E., Giuli, G., Carroll, M.R., and Davoli, I. (2001) The valence and speciation of sulfur in glasses by x-ray absorption spectroscopy. Canadian Mineralogist, 39, 331–339.

Piccoli, P.M., and Candela, P.A. (2002) Apatite in Igneous Systems. Reviews in Mineralogy and Geochemistry, 48, 255–292.

Pokrovski, G.S., and Dubrovinsky, L.S. (2011) The S_3^- Ion Is Stable in Geological Fluids at Elevated Temperatures and Pressures. Science, 331, 1052–1054.

Pokrovski, G.S., and Dubessy, J. (2015) Stability and abundance of the trisulfur radical ion S_3^- in hydrothermal fluids. Earth and Planetary Science Letters, 411, 298–309.

Ravel, B., and Newville, M. (2005) ATHENA, ARTEMIS, HEPHAESTUS: Data analysis for X-ray absorption spectroscopy using IFEFFIT. Journal of Synchrotron Radiation, 12, 537–541.

Richards, J.P. (2014) The oxidation state, and sulfur and Cu contents of arc magmas: Implications for metallogeny. Lithos, 233, 27–45.

Rouse, R.C., and Dunn, P.J. (1982) A contribution to the crystal chemistry of ellestadite and the silicate sulfate apatites. American Mineralogist, 67, 90–96.

Sato, M., Hickling, N. L., McLane, J.E. (1973) Oxygen fugacity values of Apollo 12, 14, and 15 lunar samples and reduced state of lunar magmas. Proceedings of the Lunar Science Conference, 4, 1061–1079.

Simon, A.C., and Ripley, E.M. (2011) The Role of Magmatic Sulfur in the Formation of Ore Deposits. Reviews in Mineralogy and Geochemistry, 73, 513–578.

Streck, M.J., and Dilles, J.H. (1998) Sulfur evolution of oxidized arc magmas as recorded in apatite from a porphyry copper batholith. Geology, 26, 523.

Tepper, J., and Kuehner, S. (1999) Complex zoning in apatite from the Idaho batholith: A record of magma mixing and intracrystalline trace element diffusion. American Mineralogist, 84, 581–595.

Treloar, P.J., and Colley, H. (1996) Variation in F and Cl contents in apatites from magnetite-apatite ores in northern Chile, and their ore-genetic implications. Mineralogical Magazine, 60, 285–301.

Webster, J.D., and Piccoli, P.M. (2015) Magmatic Apatite: A Powerful, Yet Deceptive, Mineral. Elements, 11, 177–182.

Wilke, M., Jugo, P.J., Klimm, K., Susini, J., Botcharnikov, R., Kohn, S.C., and Janousch, M. (2008) The origin of S^{4+} detected in silicate glasses by XANES. American Mineralogist, 93, 235–240.

Wojdyr, M. (2010) Fityk: A general-purpose peak fitting program. Journal of Applied Crystallography, 43, 1126–1128.

Young, E.J., Myers, A.T., Munson, E.L and Conklin, N.M. (1969) Mineralogy and geochemistry of fluorapatite from Cerro de Mercado, Durango, Mexico. USGS Professional Paper 650-D, D84-D93.

Zajacz, Z., Candela, P. a., Piccoli, P.M., and Sanchez-Valle, C. (2012) The partitioning of sulfur and chlorine between andesite melts and magmatic volatiles and the exchange coefficients of major cations. Geochimica et Cosmochimica Acta, 89, 81–101.

CHAPTER 3: CRYPTIC METASOMATISM DURING LATE-STAGE LUNAR MAGMATISM IMPLICATED BY SULFUR IN APATITE

Co-authors: Brian Konecke, Adrian Fiege, Adam Simon, and Francois Holtz

Published in *Geology* (2017) **45**, 739-742

3.1 ABSTRACT

The use of volatile bearing (H_2O-Cl-F-C-S) minerals as proxies for constraining the volatile content of lunar magmas remains controversial. In this study, we apply published F-Cl-S signature trends in apatite from lunar mare basalts, new experimentally determined apatite-melt partition coefficients for S, and thermodynamic modeling to demonstrate unequivocally that fractional crystallization of lunar silicate melt cannot produce the observed S signatures of lunar apatite. Instead, metasomatic (cryptic) alteration by a S-Cl bearing, F-poor volatile phase plausibly explains the volatile element zoning in lunar apatite, consistent with some lunar magmas being more volatile rich than previously suggested.

3.2 INTRODUCTION

Analysis of lunar mare basalts sampled during the Apollo missions supported the hypothesis that lunar magmas were depleted in water and other volatiles, relative to their terrestrial analogs (Sharp et al., 2010; Greenwood et al., 2011; Boyce et al., 2014; Robinson and Taylor, 2014). However, recently reported volatile abundances of olivine-

hosted silicate melt inclusions (Hauri et al., 2011), lunar volcanic glasses (Saal et al., 2008; Hauri et al., 2015; Wetzel et al., 2015), nominally anhydrous minerals (Hui et al., 2013; Mills et al., 2017), and apatite (Greenwood et al., 2011; Boyce et al., 2014) indicate that lunar magmas were volatile bearing (Hui et al., 2013) and even volatile rich (Mills et al., 2017). These contradictory findings have stimulated debate as to whether the relative abundances of F, Cl, and OH in lunar apatite can be used as a proxy to assess volatile concentrations in the silicate melts from which lunar apatite crystallized.

A recently proposed hypothesis to explain the F-Cl-OH trends of lunar apatite (Boyce et al., 2014) invokes nucleation and growth of apatite from an interstitial, almost anhydrous (~10 μg/g H_2O) rhyolitic melt, which evolved through crystallization (≥88 to 99% crystals; Sha, 2000) of a cooling, sulfide-undersaturated basaltic magma. The magmatic origin of the apatite in mare basalts is widely accepted; however, the reason for the volatile zoning is controversial. The fractional crystallization model for the volatile signature in lunar apatite is based on preferential incorporation of F >> Cl > OH into the apatite structure, resulting in increasing ratios of Cl/F and OH/F of the residual melt. As apatite continues to grow from the cooling, residual rhyolitic melt, it progressively incorporates Cl > OH >> F, possibly explaining the systematic, core-to-rim F-Cl-OH variation (Boyce et al., 2014; Figure 3.1). Sulfur exhibits the same behavior as Cl (Figure 3.1); however, the fractional crystallization hypothesis could not be tested for the reported enigmatic S signature of lunar apatite (Greenwood et al., 2011; Boyce et al., 2014) due to the complete absence of thermodynamic data required to model S partitioning between apatite and rhyolitic melt under reducing conditions, where all S in the melt is present as sulfide (S^{2-}).

Sulfur in apatite can be used as a proxy to trace the evolution of the S content of silicate melts, since (in contrast to the stoichiometric structural constituents F, Cl, and OH) S behaves as a trace element in the apatite structure, therefore permitting the application of apatite-melt partition coefficients, $D_S^{ap/m}$ (Parat et al., 2011). Historically, S was inferred to be present in apatite as sulfate only (S^{6+}; Parat et al., 2011), but the incorporation of S^{2-} and a minor contribution of S^{4+} were demonstrated by using X-ray absorption near edge spectroscopy (XANES; Konecke et al., 2017). Those authors demonstrate that the oxidation state of S-in-apatite is a function of oxygen fugacity (fO_2) and that $D_S^{ap/m}$ is redox sensitive; here, S^{6+} likely replaces phosphate in apatite (Parat et al., 2011), while S^{2-} may favor the column anion site (Henning et al., 2000). In this study, we use new experimental $D_S^{ap/m}$ data and thermodynamic modeling to test if crystal fractionation can explain the variation of S concentrations in apatite from reduced lunar mare basalts (Sato et al., 1973).

3.3 THERMODYNAMIC MODELING

Rhyolite-MELTS (Ghiorso and Gualda, 2015) was used to estimate a liquidus temperature ($T_{Liquidus}$) of 1090 ± 50°C for the residual lunar rhyolitic glass melt (12039,42; Boyce et al., 2014), which was presumably in equilibrium with the rim of lunar apatite (Rhodes et al., 1977). This agrees with experimentally determined solidus temperatures of lunar mare basalt of ~1,100°C, considering that the $T_{Solidus}$ of the basalt should be similar to the $T_{Liquidus}$ of late-stage residual rhyolite (cf. Taylor et al., 1991 and references therein; see Appendix Section B3.1 and B3.2). We followed Liu et al. (2007) to calculate the theoretical sulfur content in the residual lunar rhyolitic melt at sulfide saturation (SCSS) for melt H_2O contents ranging from 1 to 10,000 µg/g H_2O, fO_2 of ΔIW

iron-wüstite = -1.5 to +3.5, 1090°C, and 0.1 MPa. These parameters were selected in order to achieve the maximum possible concentration of S in melt before reaching sulfide saturation, while considering conditions reasonable for lunar magmatism (e.g., <100 µg/g H_2O in the lunar basaltic melt; Robinson and Taylor, 2014; and references therein).

3.4 EXPERIMENTAL APPROACH

Apatite crystallization experiments in rhyolitic systems were conducted for 3-5 days in rapid-quench internally heated pressure vessels at 300 MPa, $\log(fO_2) = \Delta FMQ-1$, FMQ, ΔFMQ+3 (FMQ: fayalite-magnetite-quartz buffer), and 1,000°C (i.e., < $T_{Liquidus}$ due to the melting point of the gold capsules). The capsules were loaded with ~37 mg of rhyolitic glass (Appendix Table B1), ~4.5 or ~7.5 wt% H_2O; and either 20,000 µg/g, 10,000 µg/g, or 5,000 µg/g pyrrhotite ($Fe_{1-X}S$; Sudbury, Ontario) to obtain sulfide saturated and sulfide undersaturated melts, respectively. Details are provided in Appendix section B1 and B2; additional results for mafic (lamproitic) systems are presented in Appendix Section B3. Experimental glass and apatite of the run products were characterized quantitatively by electron probe microanalysis to determine $D_S^{ap/m}$ (see Appendix Section B2; Appendix Table B2 and B3).

3.5 RELEVANCE OF THE EXPERIMENTS FOR LUNAR SYSTEMS

Experimental conditions were chosen to investigate end-member scenarios applicable to lunar magmatic systems by crystallizing apatite with a lunar-like apatite F/Cl/H composition. However, for technical reasons, experimental conditions differ slightly from lunar conditions. To reach a lower $T_{Liquidus}$ for the desired rhyolitic composition (required for the use of gold capsules), a relatively elevated melt water

content was used, which also enhances the size of the apatite crystals; while, the H_2O content of a melt coexisting with apatite is irrelevant for the applicability of the results to lunar magmatic systems, considering that the molar F/Cl/H ratios of the melt control the molar F/Cl/H ratios of the crystallizing apatite (cf. Boyce et al., 2014).

Temperature, fO_2 and the S content in the melt impose the strongest controls on $D_S^{ap/m}$ (Parat et al., 2004). The $D_S^{ap/m}$ is reported to decrease with increasing T (Peng et al., 1997; Parat et al., 2004). Considering the difference of 90°C between the experimental temperature and $T_{Liquidus}$ for lunar felsic melt, our experiments yield conservative $D_S^{ap/m}$ values to test the fractional crystallization hypothesis. At $fO_2 \leq \Delta FMQ$, S in silicate melts is exclusively present as sulfide (S^{2-}; Jugo et al., 2010), and a decrease in fO_2 from ΔFMQ-1 to ΔIW+0 (lunar basalt; Sato et al., 1973) minimally affects the SCSS (Figure 3.2A), but perhaps decreases the $D_S^{ap/m}$ considering that $S^{2-}/\Sigma S$ in apatite has not reached unity at ΔFMQ (Konecke et al., 2017). The effect of S content in the melt on the $D_S^{ap/m}$ was tested experimentally by performing sulfide saturated and undersaturated runs (Appendix Table B2). The differences between lunar systems and our experiments with respect to pressure (Peng et al., 1997) and melt composition (Parat et al., 2011) have a negligible effect on $D_S^{ap/m}$; the latter was confirmed by experiments using a mafic melt (Appendix Section B3.1 and Table B3). However, despite the negligible effect of melt composition (rhyolite vs. lamproite), the non-Henrian behavior of S partitioning between apatite and melt (Parat et al., 2011) limits the application of the determined $D_S^{ap/m}$ values to rhyolitic (and lamproitic) systems.

3.6 RESULTS

The apatite crystallization experiments yielded $D_S^{ap/m}$ (±1σ) values for reduced rhyolitic melts: ΔFMQ-1 = 0.38±0.09 (sulfide saturated); ΔFMQ = 0.46±0.04 (sulfide saturated); and ΔFMQ = 0.18±0.04 (sulfide undersaturated; Figure 3.2B; Appendix Table B2). A strong decrease of $D_S^{ap/m}$ is observed between oxidized (ΔFMQ+3; S^{6+} only in the melt;) and reduced (ΔFMQ-1; S^{2-} only in the melt) systems (see Appendix Table B2). However, results for ΔFMQ and ΔFMQ-1 are identical within analytical uncertainty, revealing a minor decrease in the $D_S^{ap/m}$ as the fO_2 decreases below ΔFMQ (see Appendix Section B1).

Apatite grains crystallized in the experiments have F-Cl-S contents similar to the core of the lunar apatite (lunar vs. experimental apatite: 2.10 vs. 1.82-2.16 wt% F; 0.10 vs. 0.01-0.12 wt% Cl; below detection limit vs. 33-88 μg/g S; see Appendix Table B2). The SCSS model by Liu et al. (2007) closely reproduces the S content of our experimental sulfide-saturated rhyolitic melts (e.g., ΔFMQ-1: SCSS model = 203 μg/g S vs. 220 ±7 (1σ) μg/g S measured in glass). Considering the aforementioned T-P-X-fO_2 effect on $D_S^{ap/m}$, our experimental and modeling results obtained for reduced rhyolitic systems (≤ΔFMQ) provide the most stringent, conservative estimates of S in the late-stage lunar rhyolitic melt and $D_S^{ap/m}$ to test whether or not the S concentrations of apatite can be reconciled with the formation of rhyolites by crystal fractionation.

3.7 DISCUSSION

The SCSS data (Figure 3.2A) and the experimental $D_S^{ap/m}$ values are combined to constrain the maximum S concentrations in apatite that crystallized from lunar rhyolitic melts (Figure 3.2B, green box), where equation 3.1 is expressed as:

$$[S^{ap}_{max}] = SCSS \times D_S^{ap/m}$$

The reported S contents of lunar apatite cores and rims are below detection limit (<200 μg/g) and ~430 μg/g, respectively (see caption of Figure 3.1). The value below detection limit for the lunar apatite core is consistent with our model, in which the $[S^{ap}_{max}]$ ranges between 10-90 μg/g S, depending on the H_2O content of the lunar felsic melt (1 μg/g to 10,000 μg/g H_2O, respectively; green box Figure 3.2B). However, assuming that the lunar rhyolitic melt remained sulfide undersaturated during fractional crystallization (Gibson et al., 1977), S concentrations of ~2,300 μg/g S in the rhyolitic melt are required to explain the S content in the apatite rim (Figure 3.2B). The nominally dry (≤100 μg/g H_2O; Robinson and Taylor, 2014), sulfide undersaturated rhyolitic lunar melt reaches sulfide saturation at ≤80 μg/g S. Thus, a ≥29 times higher SCSS is required to produce lunar apatite rims containing ~430 μg/g S and coexisting with the residual rhyolitic melt. While the necessary concentration of S in rhyolitic melts can be achieved at >5 orders of magnitude higher fO_2 than reported for lunar magmas, there is no petrologic evidence for conditions >ΔIW+5 (Sato et al., 1973), at which S^{6+} would the dominant oxidation state of S in the melt (Jugo et al., 2010; see Appendix section B3).

A second scenario to explain the enigmatic S enriched lunar apatite rims involves conditions at which the rhyolitic melt could reach sulfide saturation during apatite crystallization, considering that troilite (FeS) was observed in the mesostasis of lunar

mare basalts (Bunch et al., 1972). However, our results demonstrate that even sulfide saturated rhyolitic melts cannot produce the S concentrations in apatite rim through fractional crystallization alone. That scenario requires ~5 to 35 times higher S contents in hydrous (~10,000 μg/g H_2O) and dry (~1 μg/g H_2O) rhyolitic melts, respectively, than is possible at sulfide saturation (Figure 3.2B; black dashed lines). However, even elevated water concentrations in a residual rhyolitic melt cannot explain the S contents in lunar apatite rims (e.g., the SCSS increases to 203 μg/g S for rhyolitic melt containing ~20,000 μg/g H_2O, where ~930 μg/g S in the melt are required to crystallize apatite containing ~430 μg/g S; see Figure 3.2B).

Based on the results presented here, we propose that a new, plausible mechanism for the observed volatile signatures in lunar apatite involves a late-stage, cryptic metasomatic alteration (Figure 3.2C) by a S and Cl bearing volatile phase released during degassing (e.g., due to decompression; Tartèse et al. 2014; Hauri et al., 2015; Wetzel et al., 2015) from magma at deeper levels of the lunar mare magma plumbing system. Notably, it is well documented that S and Cl partition strongly into a magmatic volatile phase (Zajacz et al., 2012), whereas F is more compatible in the coexisting silicate melt (Webster et al., 2014). Cryptic metasomatism is implicated by the observed enrichment of trace elements (Si, S, Fe, REE)—which are compatible in a magmatic volatile phase—along the lunar apatite 12039 grain rims (Figure 1 in Boyce et al., 2014) and consistent with S-Cl enrichment and F depletion near cracks in the lunar apatite (open symbols in Figs. 1 and 2C). In this scenario, the bulk mare basalt 12039 remains largely unaffected by metasomatism (see Appendix section B3.).

3.8 CONCLUSION AND IMPLICATIONS

We hypothesize that cryptic metasomatic alteration played an important role during late-stage lunar magmatism, consistent with recent studies (Bell et al., 2015; Wetzel et al., 2015) that provide evidence for the presence of a free volatile phase during lunar magmatism. The volatile and textural signatures of lunar apatite are best explained by crystallization of Cl-H-S poor, fluorapatite from a nearly dry (≤100 μg/g H_2O; Robinson and Taylor, 2014) rhyolitic melt, which was subsequently altered to a S enriched fluor-chlorapatite due to the interaction with a S-Cl bearing, F-poor volatile phase. This is consistent with concentration of volatiles observed for metasomatized terrestrial apatite from the Mina Carmen iron oxide – apatite deposit, Chile (see Appendix section B3). Our scenario is supported by results of Shearer et al. (2012) and Bell et al. (2015) and indicates a heterogeneous volatile distribution on Earth's moon (McCubbin et al., 2011; Robinson and Taylor, 2014; Mills et al., 2017).

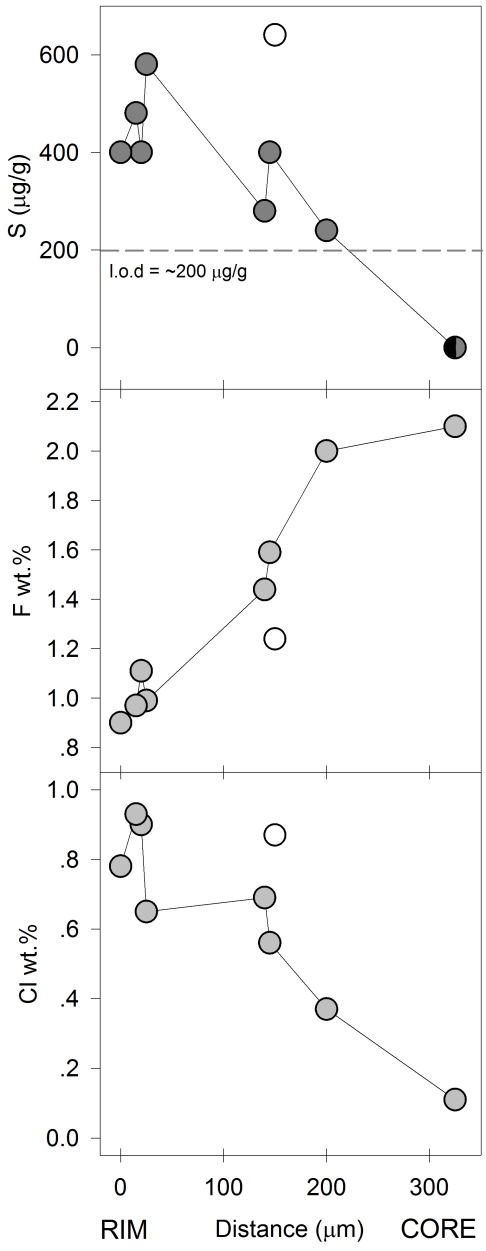

Figure 3.1: The S-Cl-F signature in apatite from lunar mare basalts (sample 12039,42 grain 12; Boyce et al., 2014). This is a modified version of Fig. 3 published by Boyce et al. (2014), data from Greenwood et al. (2011). Greenwood et al. (2011) reported S contents of the apatite core as below their (unpublished) limit of detection (l.o.d); a l.o.d of ≤200 µg/g S was calculated by using their reported analytical conditions (dashed gray line). Semi-filled circle: Below l.o.d; open circles: data near cracks, excluded by Boyce et al. (2014; see Appendix section B3).

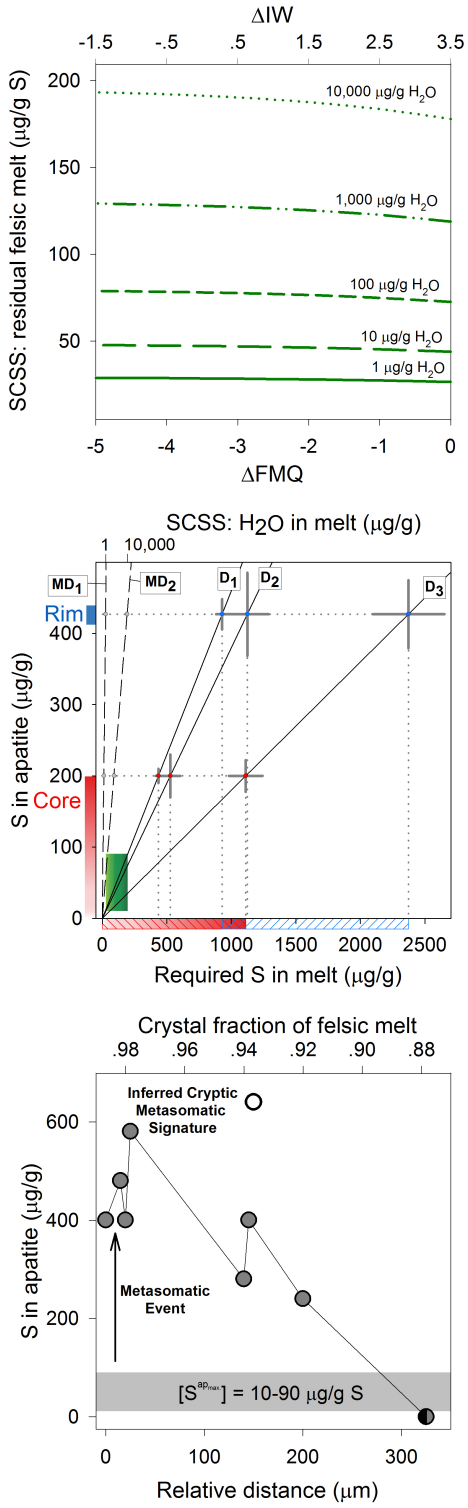

Figure 3.2 (A-C): (A) Sulfur content at sulfide saturation (SCSS) of the lunar felsic melt; predicted by using the Liu et al. (2007) model**.** This SCSS model has demonstrated reproducibility for various natural and experimental conditions and compositions, including our run products and systems with low H_2O contents. The green lines represent

the SCSS for residual lunar rhyolitic melts containing 1 to 10,000 μg/g H_2O; modeled at $\log(fO_2)$ = ΔFMQ-5 to ΔFMQ and $T_{Liquidus}$ = 1090°C. A reasonable error of ±50°C for the $T_{Liquidus}$ (MELTS; see Thermodynamic Modeling) results in an absolute uncertainty for SCSS of ±20 μg/g S. (B) Modeled and measured sulfur contents in lunar apatite and melt. Solid lines represent the experimentally determined $D_S^{ap/m}$ (±1σ) values, where D_1 = 0.46±0.04, ΔFMQ, sulfide saturated; D_2 = 0.38±0.09, ΔFMQ-1, sulfide saturated; D_3 = 0.18±0.04, ΔFMQ, sulfide undersaturated. The black dashed lines represent the modeled, *implausible* values for $D_S^{ap/m}$ (MD) required to reproduce the S content in the lunar apatite rims based on SCSS values; MD_1 = 16.4 and MD_2 = 2.2. The vertical dotted lines constrain the S content of the melt required to produce a certain S content in the apatite (horizontal dotted lines) as a function of the $D_S^{ap/m}$ (i.e., D_1, D_2, or D_3). The solid blue and fading red boxes on the Y-axis represent the published S contents of lunar apatite core and rim, respectively (Greenwood et al., 2011). A fading filling was used to illustrate that the S content of the lunar apatite core is ≤200 μg/g S (i.e., the estimated limit of detection, see Fig. 3.1). The hashed fading red and hashed blue boxes on the X-axis represent the S content in the melt required to produce the measured S content in the lunar apatite core and rim, respectively, when applying D_1, D_2, or D_3. The left and right vertical edges of the green box constrain the range of SCSS (bottom X-axis) predicted for lunar rhyolitic melts containing 1 and 10,000 μg/g H_2O (upper X-axis), where SCSS = 26 (left edge, light green) and 193 (right edge, dark green) μg/g S, respectively. Using these upper and lower SCSS limits for the lunar rhyolitic melt, maximum (~90 μg/g S; upper edge of the green box) and minimum (~10 μg/g S; lower edge of the green box) S contents in coexisting lunar apatite were calculated by using the highest plausible $D_S^{ap/m}$ value (D_1). Gray bars represent 2σ error for the lunar apatite core and rim scenarios, rather than the overall error for $D_S^{ap/m}$. (C) Cryptic metasomatic S signature recorded in lunar apatite. The gray box illustrates the predicted, plausible range of S contents in lunar apatite that can be produced through crystallization from the residual rhyolitic melt; i.e., $[S^{ap}_{max.}]$ = 10-90 μg/g S. Semi-filled circle: Below l.o.d; open circle: data near cracks, excluded by Boyce et al. (2014; see Appendix Section B3.2).

3.9 REFERENCES

Bell, A.S., Shearer, C., deMoor, J.M., and Provencio, P. (2015) Using the sulfide replacement petrology in lunar breccia 67915 to construct a thermodynamic model of S-bearing fluid in the lunar crust: Geochimica et Cosmochimica Acta, 171, 50–60.

Boyce, J.W., Tomlinson, S.M., McCubbin, F.M., Greenwood, J.P., and Treiman, A.H. (2014) The lunar apatite paradox: Science (New York, N.Y.), 344, 400–402.

Bunch, T.E., Keil, K., and Prinz, M. (1972) Mineralogy, petrology and chemistry of lunar rock 12039: Meteoritics, 7, 245–255.

Ghiorso, M.S., and Gualda, G.A.R. (2015) An H_2O–CO_2 mixed fluid saturation model compatible with rhyolite-MELTS: Contributions to Mineralogy and Petrology, 308, 957-1039.

Gibson, E. K., Jr., Brett, R., & Andrawes, F. (1977) Sulfur in lunar mare basalts as a function of bulk composition: Lunar Science Conference, 8th, 2, 1417–1428.

Greenwood, J.P., Itoh, S., Sakamoto, N., Warren, P., Taylor, L., and Yurimoto, H. (2011) Hydrogen isotope ratios in lunar rocks indicate delivery of cometary water to the Moon: Nature Geoscience, 4,79–82.

Hauri, E.H., Weinreich, T., Saal, A.E., Rutherford, M.C., and Van Orman, J.A. (2011) High Pre-Eruptive Water Contents Preserved in Lunar Melt Inclusions: Science, 333, 213–215.

Hauri, E.H., Saal, A.E., Rutherford, M.J., and Van Orman, J. a. (2015) Water in the Moon's interior: Truth and consequences: Earth and Planetary Science Letters, 409, 252–264.

Henning, P.A., Adolfsson, E., and Grins, J. (2000) The chalcogenide phosphate apatites $Ca_{10}(PO_4)_6S$, $Sr_{10}(PO_4)_6S$, $Ba_{10}(PO_4)_6S$ and $Ca_{10}(PO_4)_6Se$: Zeitschrift für Kristallographie - Crystalline Materials, 215, 226-230.

Hui, H., Peslier, A.H., Zhang, Y., and Neal, C.R. (2013) Water in lunar anorthosites and evidence for a wet early Moon: Nature Geoscience, 6, 177–180.

Jugo, P.J., Wilke, M., and Botcharnikov, R.E. (2010) Sulfur K-edge XANES analysis of natural and synthetic basaltic glasses: Implications for S speciation and S content as function of oxygen fugacity: Geochimica et Cosmochimica Acta, 74, 5926–5938.

Konecke, B.A., Fiege, A., Simon, A.C., and Parat, F. (2017) Co-variability of S^{6+}, S^{4+} and S^{2-} in apatite as a function of oxidation state – implications for a new oxybarometer,, 102,548–557.

Kim, Y.J., Konecke, B., Fiege, A., Simon, A., and Becker, U. (2017) An ab-initio study of the energetics and geometry of sulfide, sulfite, and sulfate incorporation into apatite: The thermodynamic basis for using this system as an oxybarometer: American Mineralogist, 102, 1646–1656.

Liu, Y., Samaha, N.T., and Baker, D.R. (2007) Sulfur concentration at sulfide saturation (SCSS) in magmatic silicate melts: Geochimica et Cosmochimica Acta, 71, 1783–1799.

McCubbin, F.M., Jolliff, B.L., Nekvasil, H., Carpenter, P.K., Zeigler, R.A., Steele, A., Elardo, S.M., and Lindsley, D.H. (2011) Fluorine and chlorine abundances in lunar apatite: Implications for heterogeneous distributions of magmatic volatiles in the lunar interior: Geochimica et Cosmochimica Acta, 75, 5073–5093.

Mills, R.D., Simon, J.I., Alexander, C.M.O., Wang, J., and Hauri, E.H. (2017) Water in alkali feldspar: The effect of rhyolite generation on the lunar hydrogen budget: Geochemical Perspectives Letters, 3, 115–123.

Parat, F., and Holtz, F. (2004) Sulfur partitioning between apatite and melt and effect of sulfur on apatite solubility at oxidizing conditions: Contributions to Mineralogy and Petrology, 147, 201–212.

Parat, F., Holtz, F., and Streck, M.J. (2011) Sulfur-bearing Magmatic Accessory Minerals: Reviews in Mineralogy and Geochemistry, 73, 285–314.

Rhodes, J.M, Blanchard D.P, M.A. Dungan, J.C Brannon, Rodgers, K. (1977) Chemistry of Apollo 12 mare basalts: Magma types and fractionation processes: Proc. Lunar Sci. Conf. 8th, 1305–1338.

Robinson, K.L., and Taylor, G.J. (2014) Heterogeneous distribution of water in the Moon: Nature Geoscience, 7, 401–408.

Saal, A.E., Hauri, E.H., Cascio, M.L., Van Orman, J.A., Rutherford, M.C., and Cooper, R.F. (2008) Volatile content of lunar volcanic glasses and the presence of water in the Moon's interior: Nature, 454, 192–195.

Sato, M., Hickling, N. L., McLane, J.E. (1973) Oxygen fugacity values of Apollo 12, 14, and 15 lunar samples and reduced state of lunar magmas: Proceedings of the Lunar Science Conference, 4, 1061–1079.

Sha, L.K. (2000) Whitlockite solubility in silicate melts: Some insights into lunar and planetary evolution: Geochimica et Cosmochimica Acta, 64, 3217–3236.

Sharp, Z.D., Shearer, C.K., McKeegan, K.D., Barnes, J.D., and Wang, Y.Q. (2010) The Chlorine Isotope Composition of the Moon and Implications for an Anhydrous Mantle: Science, 329, 1050–1053.

Taylor G. J., Warren P., Ryder G., Delano J., Pieters C. and Lofgren G. (1991) Chapter 6: Lunar Rocks. In Lunar Sourcebook: A User's Guide to the Moon, 183–284.

Tartèse, R., Anand, M., McCubbin, F.M., Elardo, S.M., Shearer, C.K., and Franchi, I. a. (2014) Apatites in lunar KREEP basalts: The missing link to understanding the H isotope systematics of the Moon: Geology, 42, 363–366.

Webster, J.D., Goldoff, B., Sintoni, M.F., Shimizu, N., and De Vivo, B. (2014) C-O-H-Cl-S-F Volatile Solubilities, Partitioning, and Mixing in Phonolitic-Trachytic Melts and Aqueous-Carbonic Vapor Saline Liquid at 200 MPa: Journal of Petrology, 55, 2217–2248.

Wetzel, D.T., Hauri, E.H., Saal, A.E., and Rutherford, M.J. (2015) Carbon content and degassing history of the lunar volcanic glasses: Nature Geoscience, 8, 755–758.

Zajacz, Z., Candela, P. A., Piccoli, P.M., Wälle, M., and Sanchez-Valle, C. (2012) Gold and copper in volatile saturated mafic to intermediate magmas: Solubilities, partitioning, and implications for ore deposit formation: Geochimica et Cosmochimica Acta, 91, 140–159.

CHAPTER 4: SULFUR-IN-APATITE: AN EMPIRICAL CALIBRATION OF AN OXYBAROMETER FOR MAGMATIC SYSTEMS

4.1 ABSTRACT

The incorporation of S-in-apatite and the partitioning of S between apatite and silicate melt ($D_S^{ap/m}$) have been proposed to vary systematically as a function of the oxidation state of the system owing to the demonstrated control that redox conditions have on the oxidation state of sulfur in silicate magmas. In this study, we performed apatite crystallization experiments in mafic silicate melt at 1000°C, 300 MPa and a range of oxygen fugacities (fO_2; e.g., where log fO_2 [ΔFMQ] = -1, +0, +0.3, +1.2, and +3). Variable amounts of sulfur (~0.37 and ~0.28 wt.% S) were added to the system to test the possible influence of sulfur fugacity on the $D_S^{ap/m}$. The S content of apatite and co-existing melt demonstrate that the S content of apatite and values of $D_S^{ap/m}$ systematically increase with increasing fO_2 ($D_S^{ap/m}$ = 0.02±0.01 to 3.20±0.19). Micro X-ray absorption near edge structure (μ-XANES) spectroscopy at the S *K*-edge was used to measure, *in situ*, the oxidation state(s) of S in experimentally crystallized apatite. The integrated $S^{6+}/\Sigma S$ peak area ratio and centroid energies (eV) were determined for each experimental run product. The orientation effects occurring during S-XANES analyses of apatite were considered by merging spectra from multiple grains with random crystallographic orientation. The $S^{6+}/\Sigma S$ peak area ratios and the centroid energies increase systematically

with fO_2. Centroid energies versus ΔFMQ results were fitted using a sigmoidal function (adjusted $R^2 = 0.99$), where:

$$C_{eV} = \frac{1}{1 + exp^{\left(\frac{FMQ - 0.303\ [\pm 0.017]}{0.114\ [\pm 0.026]}\right)}} \quad R^2 = 0.99$$

The calibration curve exhibits a sharp transition (e.g., slope of inflection point) from low to high centroid energies (eV). As a consequence, the S-in-apatite oxybarometer is highly sensitive from ~FMQ-0.5 to ~FMQ+1. Centroid energies that plot outside this range can only provide minimum/maximum constraints of fO_2 (e.g., ΔFMQ).

The S-XANES oxybarometer calibration is particularly sensitive for mafic systems such as mid ocean ridge basalts (MORB), relatively reduced ocean island basalts (OIB), and backarc basin basalt (BABB) systems. Owing to the ubiquity of apatite in magmatic and magmatic-hydrothermal systems, combined with the redox sensitive incorporation behavior of S-in-apatite, the S-in-apatite oxybarometer demonstrates high potential to serve as a useful oxy-barometer, applicable to systems/conditions where alternative methods are rather insensitive.

4.2 INTRODUCTION

Sulfur (S) is a ubiquitous volatile and redox sensitive element in terrestrial magmatic systems, and plays a fundamental role in various biological, atmospheric, climatic, and geological processes (Faure, 1986; Métrich and Mandeville 2010; Mandeville, 2010; Manning, 2011). Sulfur is a fundamental component in magmatic-hydrothermal ore deposits, that form in a broad range of magmatic-tectonic environments including: subduction zones (e.g., porphyry, epithermal deposits; Simon and Ripley,

2011), mid-ocean ridges (e.g., volcanic-hosted massive sulfide deposits, Huston et al., 2010), and mid-continent rifts (e.g., magmatic sulfide deposits; Simon and Ripley, 2011).

Sulfur is inferred to be present as mainly sulfide (S^{2-}) and sulfate (S^{6+}) complexes in reduced and oxidized silicate melts, respectively (Jugo et al., 2010, Wilke et al., 2008); Matjuschkin et al. (2016) recently proposed that a relatively insoluble, S-species of intermediate oxidation state (e.g., S_3^-, S^0, and S^{4+}) may also be present in some silicate melts under certain conditions. Sulfur in aqueous fluids derived from magmatic-hydrothermal systems include, sulfate (S^{6+}; as HSO_4^-; Barré et al., 2017), sulfite (S^{4+}; as SO_2), sulfide (S^{2-}; as H_2S; Burgisser et al., 2007; 2015), and a trisulfur ion (S_3^-; Pokrovski and Dubrovinsky, 2011; Pokrovski and Dubessy, 2015 and Barré et al., 2017).

Despite the importance of fO_2 for magmatic and magmatic-hydrothermal processes (Evans, 2006), the accurate determination fO_2 of the system often remains elusive. Co-existing Fe-Ti oxide pair oxygen barometry has proven to be a powerful method to directly constrain the fO_2 of a silicate melt (Ghiorso and Evans, 2008; and references therein). While in systems where Fe-Ti oxides are absent, the term "oxidized" is applied to magnetite-saturated source magmas (plutons) that can cover a range of five orders of magnitude in fO_2 that spans the transition from sulfide (S^{2-}) to sulfate (S^{6+}; Jugo et al., 2004; 2010).

Spectroscopic techniques, including Mossbauer and X-ray Absorption Near Edge Structure (XANES), have revolutionized the determination of the oxidation states of redox sensitive elements (i.e., S, Fe, V, Cr) in silicate glasses (i.e., matrix glass and/or melt inclusions) and mineral phases (Jugo et al., 2010; Fiege et al., 2017; Berry et al., 2003; 2018; Kelley and Cottrell, 2009; Cottrell et al., 2009; 2018; Righter et al., 2016;

Bell et al., 2017). However, the use of these techniques can be challenging, due to irradiation induced beam damage of silicate glasses (Wilke et al, 2008; Cottrell et al., 2018), or anisotropic effects of minerals related to matrix composition and crystal orientation (Dyar et al. 2001, 2002a; Evans et al., 2014; Bell et at., 2017).

Apatite—generally $Ca_{10}(PO_4)_6(F,Cl,OH)_2$—is a common accessory phase in terrestrial (Webster and Piccoli, 2015) and extraterrestrial (McCubbin and Jones, 2015) geologic systems, and can structurally incorporate a broad range of elements, including volatile and redox sensitive elements such as S (c.f. Parat et al., 2011; Webster and Piccoli, 2015). Apatite chemistry has been used as a geochemical tool to provide insight into the complex evolution of magmatic and magmatic-hydrothermal systems, including: [a] volatile (e.g., F, Cl, OH, S) inventories (McCubbin and Jones 2015; Webster and Piccoli, 2015; and references therein; Parat et al., 2011; Chelle-Michou and Chiaradia, 2017), and [b] metasomatic processes (Harlov, 2015, and references therein; Konecke et al., 2017a,b). The observation that S-rich apatite is commonly found in relatively oxidizing systems led to the inference that sulfate (S^{6+}) was the only oxidation state of S incorporated into apatite, via coupled substitution mechanisms (e.g., Rouse and Dunn 1982; Liu and Comodi 1993; Tepper and Kuehner, 1999; Peng et al., 1997; Parat et al. 2011b):

$$[1]\ PO_4^{3-} + Ca^{2+} = SO_4^{2-} + Na^{+}$$

$$[2]\ 2\ SO_4^{2-} + \square = Ca^{2+} + 2\ PO_4^{3-}$$

$$[3]\ 2\ PO_4^{3-} = SO_4^{2-} + SiO_4^{4-}$$

However, the recent study by Konecke et al. (2017a) demonstrated experimentally that apatite can incorporate multiple oxidation states of S, in varying proportions. In a related

study, Kim et al. (2017) used first principal (*ab-initio*) techniques to describe energetically feasible incorporation mechanisms for S^{2-}, S^{4+}, and S^{6+} in apatite, where:

$$[4]\ 2\ P^{5+} = S^{6+} + S^{4+}$$

$$[5]\ 2\ X = S^{2-} + \square$$

Konecke et al. (2017a) and Kim et al. (2017) concluded that the incorporation behavior, and the proportions of oxidation states of S (e.g., $S^{6+}/\Sigma S$) plausibly reflect the redox conditions (i.e., oxygen fugacity) at the time of apatite crystallization.

Several studies have investigated the distribution of S between apatite and silicate melt (i.e., $D_S^{ap/m}$) in order to calculate the S content of the melt prior to degassing and/or eruption (Peng et al., 1997; Parat and Holtz, 2004; 2005; Parat et al., 2008, 2011a, b; Webster and Piccoli, 2015; Konecke et al., 2017a, b). However, this application has proven challenging, for the reason that the $D_S^{ap/m}$ is sensitive to T-P-X-fO_2-fS_2 in the system (Peng et al., 1997; Parat et al., 2011b). The strong effect of fO_2 on $D_S^{ap/m}$ (Konecke et al., 2017a, b) has received little attention since oxidation states of S-in-apatite other than sulfate where only recently discovered. Konecke et al. (2017a) proposed that the presence of three S oxidations state in apatite might partially explain the non-Henrian partitioning behavior of S between apatite and melt. Therefore, considering the ability of apatite to crystallize from melts and magmatic-hydrothermal fluids (e.g., Lyons 1988; Peng et al. 1997; Streck and Dilles 1998; Parat et al. 2004, 2011b; Webster and Piccoli 2015; Mao et al. 2016), the intra- and inter-crystalline zonation with respect to S contents and oxidation states (e.g., S^{6+}, S^{4+}, S^{2-}) may serve as a proxy to reconstruct redox processes, and provide valuable insight into the behavior of S

of magmatic systems (Streck and Dilles 1998; Konecke et al., 2017a,b; Economos et al., 2017).

In this study, we combine electron probe micro-analyses (EPMA) with micro X-ray absorption near edge structure (μ-XANES) spectroscopy at the S *K*-edge, of experimentally grown apatite that equilibrated over at 1000°C, 300 MPa, and over a broad range of fO_2, to test the hypothesis that S-in-apatite can serve as a geochemical proxy for the redox, and S contents of magmatic systems.

4.3 EXPERIMENTAL METHODS

Apatite crystallization experiments were conducted in rapid-quench internally heated pressure vessels (IHPV) at Leibniz University Hannover (LUH; Germany; see Berndt et al., 2002). Gold capsules (3.8 mm OD, 0.12 mm wall thickness, 10 mm length) were loaded with 30 to 40 mg of mafic starting material (lamproite from Vestfjella, Dronning Maud Land, Antarctica), and ~6-8 wt.% deionized H_2O. All experiments were water-saturated to ensure accurate determination of the final fO_2 of the experiment (see Berndt et al., 2002; Scaillet et al., 1995).

In order to test the effect of bulk S on the redox and partitioning systematics, two bulk S contents, 0.37 wt.% S (Series #1) and 0.28 wt.% S (Series #2), were used (see Table 4.1). This procedure ensures similar bulk compositions for all runs, while the oxidation state of S in the mixtures are similar to the S oxidation state(s) prevailing at the experimental redox conditions, and thus, the time required to reach redox equilibrium throughout the capsules is minimized. We highlight that even without this step, equilibrium in terms of fO_2 between the vessel and experimental capsule (i.e., the center) is reached within a few hours (cf. Fiege et al. 2014). The capsules were weighed, welded

shut and placed in a drying oven (110–120 °C) for several hours, then re-weighed to check for water loss. In order to verify their mechanical integrity, capsules were placed in cold-seal pressure vessels (CSPV), pressurized to ~100 MPa, then decompressed and weighed again.

Experimental charges were run at 1000°C and 300 MPa for 3 or 5 days at 6 different imposed and controlled oxidation states, where log (fO_2) = FMQ-1, FMQ, FMQ+0.3, FMQ+1.2, and FMQ+3 (FMQ = fayalite-magnetite-quartz solid buffer; see Table 4.1 for list of experiment names and additional details). For experiments conducted at FMQ-1, FMQ, FMQ+0.3, and FMQ+1.2, the fO_2 within the IHPV was controlled by adding H_2 to the Ar-pressure medium and was monitored using a Shaw-membrane. However, the most oxidized experiment was intrinsically buffered by the IHPV at ~FMQ+3, by using pure Ar gas (Berndt et al. 2002). Both series of experiments (~0.37 and ~0.28 wt.% bulk S) were run together to ensure that the final fO_2 of both datasets were identical, with the exception being for experiments at FMQ+0.3, and the imposed fO_2 was determined to be within error of each other.

All experiments were terminated by isobaric rapid quench and were re-weighed. Capsules revealing loss of weight (i.e., of volatiles/water) during any of the experimental steps were discarded. A total of 10 successful experiments were performed and analyzed. The experimental run products were extracted from each capsule, mounted in epoxy, and fine polished for analyses.

4.4 ANALYTICAL METHODS

4.4.1 Electron Probe Micro-Analysis (EPMA)

The major and minor element abundances of apatite and co-existing glass was characterized using EPMA (CAMECA SX-100's) at: [a] University of Michigan (UM, Ann Arbor, USA), [b] the American Museum of Natural History (AMNH, New York, USA.), and [c] LUH, following the method of Konecke et al. (2017a,b). For the glass analyses we used an acceleration voltage of 15-20 keV, a beam current of 5–10 nA, and a beam size of 5–10 μm. Peak counting times of 10 s were used for major and trace elements, except 5 s for Na and 60–240 s for S. For the apatite analyses we used an acceleration voltage of 15 keV, a beam current of 10 nA and a beam size of 2 μm. Peak counting times of 20 s were used for the major and trace elements, except 5 s for F and 60-180 s for S. Previous studies (Fiege et al., 2014; 2015; Konecke et al., 2017a; 2017b) have shown that these settings minimize electron beam damage of the apatite (e.g., halogen migration; see Goldoff et al., 2012) and the glasses (e.g., diffusion of Na and Si, Al burn-in; Morgan and London, 2005). During analysis of experimental apatite, both SiO_2 and Al_2O_3 concentrations were monitored for contribution of surrounding glass and mineral phases. Analyses indicating a contribution of the glass or other mineral phases were discarded.

4.4.2 Micro X-ray absorption near edge structure (μ-XANES) at the S K-edge

In situ, μ-XANES measurements at the S *K*-edge were conducted at the GSECARS 13-ID-E beamline at Advanced Photon Source (APS), Argonne National Laboratory (USA). The beamline uses a high-flux beam (≥4.5×1010 photons/s/100

mA/mm^2) that covers an energy range of 2.4 to 28 keV, and is equipped to produce a high-spatial resolution micro-focused 2×1 μm beam using Kirkpatrick-Baez (KB) focusing mirrors. The energy of the Si(111) channel cut monochromator was calibrated to the 2481.8 (±0.2) eV white-line of the spectrum of clear double-sided adhesive tape.

We followed the procedure described by Konecke et al (2017a) for the collection and processing of S-XANES spectra. Energy ranges were collected from 2460 to 2540 eV, with step sizes of 0.1–0.3 eV at the S *K*-edge (2464 to 2484 eV), and 1 eV for the pre-and-post edge regions using 0.5–3 s scan durations per energy step. Step scan durations of 1–3 s per energy step were used to analyze experimental apatite in order to achieve high S X-ray counts; which produced high-quality spectra even for S-poor apatite (e.g., <100 μg/g S). The European Synchrotron Radiation Facility (ESRF XANES spectra database for the S K-edge was used to identify the relative S^{6+} (~2482±0.5 eV; anhydrite), sulfite S^{4+} (~2477 ±0.5 eV; sodium sulfite) and sulfide S^{2-} (~2470±0.5 eV; pyrrhotite) peak energy positions for the unknowns. Additionally, the S^{6+} (~2481.8±0.2 eV) and sulfite S^{4+} (~2477.5±0.2 eV) peak positions of Durango apatite (Lyons et al., 1988; Konecke et al., 2017a) were used as an internal reference standard to monitor session-to-session variability of peak positions. Although, the previous study of Konecke et al. (2017a) did not observe evidence for electron beam irradiation damage produced during EPMA (e.g., within the limits of current understanding of beam damage systematics; Wilke et al., 2008), S-XANES analyses were conducted prior to EPMA.

Additionally, all S-XANES analyses were monitored for contribution of S-bearing epoxy and/or adhesives, which is easily identifiable by two lines of evidence: [1] beam damage induced growth of the absorption peak at ~2473.3 eV, and reduction of the

absorption peak at ~2482.3 eV; and [2] the absence of a "nearest neighbor" feature that corresponds to oxygen, which is ubiquitous in S-XANES spectra of apatite. We stress that no indication of interaction with epoxy/adhesive during XANES analyses was observed in this study.

4.4.3 S-XANES spectra normalization and fitting

All spectra were merged and normalized using the X-ray absorption spectroscopy (XAS) data software analysis package Athena (Ifeffit package; Ravel and Newville, 2005). Normalization of merged raw spectra involves setting the pre-edge and post-edge to 0 and 1, respectively. The curve and peak fitting open source software Fityk (Wojdyr, 2010; version 0.9.8) was used for peak area integration analysis of all spectra as described by Konecke et al. (2017a). In our opinion, this integrated peak area method combined with background fitting is more robust compared to other fitting methods (e.g., Jugo et al., 2010; Brounce et al., in press), since it is less sensitive to variability of peak heights/intensities that are related, though not directly proportional, to the abundance of S in the sample.

An exponentially modified Gaussian (EMG) function was used to fit the background to eliminate contribution from the pre-and-post edges. The inflection point of the EMG function was positioned within the energy of 2478–2479 eV for all spectra, while the pre-and-post edges of the EMG function are at 0 and 1, respectively. We highlight that forced position of the inflection of the EMG function differs slightly from the method described by Konecke et al. (2017a), which used an energy range 2478–2480 eV. This adjustment produces an overall lower residual of the fitting, especially for spectra that contain a broad S^{2-} peak. However, this modification results in an absolute

integrated peak area ratio difference (Δ integrated $S^{6+}/\Sigma S$ peak area ratio) of approximately ± 0.04; i.e., below the analytical uncertainty. Gaussian area (e.g., Gaussian-A) functions were used to fit the absorption peaks within the S *K*-edge region; for further regarding fitting details, see Konecke et al. (2017a). The relative error of the integrated $S^{6+}/\Sigma S$ peak area ratios is less than ±0.1 units, based on the average results of several fittings for each S-XANES spectra. We suggest that the subtraction of the background will result in peak area ratios that closely reflect the actual fractions within the apatite because the background normalized intensities should directly reflect the abundance. Thus, the data we present are considered as semi-quantitative; whereas non-background normalized ratios provide only a qualitative measure of the S oxidation state.

4.4.4 Integrated $S^{6+}/\Sigma S$ peak area ratio and centroid position calculations

The integrated peak area ratios of the S absorption peaks (e.g., S^{6+}, S^{4+}, and sharp/broad S^{2-}) were used to evaluate relative changes in the oxidation state of S in the sample (see Konecke et al., 2017a for details). However, the integrated $S^{6+}/\Sigma S$ peak area ratio method requires that spectra contain a S^{6+} component, which may limit the applicability of this method; see discussion section 5.2 below. For this reason, centroid position energies (C_{eV}) were calculated from the Gaussian peak positions (G_i) and integrated peak area ratio (A_i) of the Gaussian, using equation (4.1):

$$C_{eV} = \frac{\Sigma\, G_i\, A_i}{\Sigma\, A_i}$$

Centroid energies (eV) that represent end-member S^{2-} and S^{6+} were calculated using pyrrhotite ($Fe_{1-X}S$; ~2474.8 eV) and anhydrite ($CaSO_4$; ~2481.8 eV) S-XANES standards (Konecke et al., 2017a; see Appendix C). The relative error of the centroid positions

energies (eV) is ±0.2 eV and was determined by the standard deviation of several fittings for each S-XANES spectra.

4.5 RESULTS

4.5.1 The S content of apatite and co-existing glass (EPMA)

The EPMA data of apatite and co-existing glass are reported in Table 4.2A and 4.2B. The S contents of apatite and glasses are plotted as a function of fO_2 in Figure 4.1. The average S contents in the glasses of the most reduced experiments (FMQ-1) are 2230 ±156 μg/g S for Series #1 (experiment LA45-IH27) and 2300 ±121 μg/g S for Series #2 (LA45-IH28). The average S content of the apatite of these run products are 44 ±25 μg/g S and 39 ±12 μg/g S for Series #1 and #2, respectively. The average S contents of glass from the reduced (FMQ) sulfide-saturated experiment ranged from 2553 ±200 μg/g S (Series #1; LA45-IH1) and 1739 ±76 μg/g S (Series #2; LA45-IH2); and the average S contents of the apatite range from 322 ±44 μg/g S to 161 ±15 μg/g S, respectively. Sulfur contents of the sulfide-saturated glasses equilibrated with reduced-intermediate redox conditions (FMQ+0.3) range from 2918 ±127 μg/g S (Series #1; LA45-IH30) to 2795 ±66 μg/g S (Series #2; LA45-IH34). The S content of the apatite from the reduced-intermediate experiments yielded values of 556 ±47 μg/g S (Series #1; LA45-IH30) and 903 ±58 μg/g S (Series #2; LA45-IH34). The S contents of intermediate-oxidized, sulfide/sulfate undersaturated experiments range from 4548 ±71 (Series #1; LA45-IH7) to 3040 ±94 (Series #2; LA45-IH8) μg/g S for the glasses, and 2982 ±174 to 2730 ±47 μg/g S for the apatite. The oxidized and sulfate undersaturated melts contained 1609±257 μg/g S (Series #1; LA45-IH13) and 1548±225 μg/g S (Series #2; LA45-IH14), whereas

the apatite S contents ranged from 4935 ±172 μg/g S (Series #1; LA45-IH13) to 4958 ±152 μg/g S (Series #2; LA45-IH14).

4.5.2 The $D_S^{ap/m}$ values of experimental run products

Apatite-melt partitioning coefficients ($D_S^{ap/m}$) were calculated for each experimental run as a function of fO_2 and are presented in Figure 4.2 and Table 4.2A and 4.2B. The Series #1 and #2 experiments performed at FMQ-1 yielded $D_S^{ap/m}$ values of 0.02 ±0.01 (LA45-IH27 and LA45-IH28; reported in 2σ standard error). The $D_S^{ap/m}$ values for experiments performed at FMQ are 0.13 ±0.02 (LA45-IH1) and 0.09 ±0.02 (LA45-IH2) for Series #1 and #2, respectively. For the reduced-intermediate redox conditions (FMQ+0.3), the $D_S^{ap/m}$ range from 0.19 ±0.02 to 0.32 ±0.02 for the Series #1 (LA45-IH30) and Series #2 (LA45-IH34) experiments. The intermediate-oxidized experiments performed at FMQ+1.2 yielded a range of $D_S^{ap/m}$ values of 0.66 ±0.04 (Series #1; LA45-IH7) and 0.90 ±0.04 (Series #2; LA45-IH8). The oxidized experiments yielded $D_S^{ap/m}$ values of 3.07 ±0.19 and 3.20 ±0.19 for Series #1 (LA45-IH13) and Series #2 (LA45-IH14), respectively.

4.5.3 Sulfur oxidation states of experimental apatite

The merged and normalized S-XANES spectra from the apatite experiments as a function of fO_2 are presented in Figure 4.3A (Series #1) and 3B (Series #2), and the measured oxidation states of S are listed in Table 4.3. The S-XANES spectra of Series #1 and #2 are reported in Appendix C. The following observations are made for the different redox conditions:

[FMQ-1] (LA45-IH27: Series #1; LA45-IH28: Series #2)*:* The apatite of the experiments performed at FMQ-1 exhibit dominant S^{2-} (~2469.8 eV sharp peak and ~2476.3 eV broad peak), and minor S^{6+} (~2481.8 eV) peaks.

[FMQ] (LA45-IH1: Series #1; LA45-IH2: Series #2)*:* Apatite from experiments performed at FMQ exhibit dominant S^{2-} (~2469.8 eV sharp peak and ~2476.7 eV broad peak), and S^{6+} (~2481.8 eV) peaks (LA45-IH1 data from Konecke et al., 2017a).

[FMQ+0.3] (LA45-IH30: Series #1; LA45-IH34: Series #2)*:* The apatite of the FMQ+0.3 experiments exhibit dominant S^{2-} (~2469.7 eV sharp peak, and ~2476.7 eV broad peak), S^{1+} (~2472.9 eV), S^{4+} (~2477.5 eV), and S^{6+} (~2481.8 eV) peaks.

[FMQ+1.2] (LA45-IH7: Series #1; LA45-IH8: Series #2): The merged XANES spectra for experimental apatite crystallized from intermediate lamproitic melt exhibit dominant S^{4+} (~2477.5 eV), and S^{6+} (~2481.8 eV) peaks.

[FMQ+3] (LA45-IH13: Series #1; LA45-IH14: Series #2): The merged XANES spectra for experimental apatite crystallized from intermediate lamproitic melt exhibit dominant S^{4+} (~2477.5 eV), and S^{6+} (~2481.8 eV) peaks. Crystallographic orientation effects were not observed for the experiments performed at FMQ+1.2 and FMQ+3; see Konecke et al., 2017a for discussion.

4.5.4 Integrated $S^{6+}/\Sigma S$ peak area ratio and centroid energies of apatite experiments

The integrated $S^{6+}/\Sigma S$ peak area ratios and centroid positions (eV) of S in experimental apatite were constrained over the broad range of redox conditions; e.g., FMQ-1 to FMQ+3 (see Table 4.3). The following observations are made for the different redox conditions:

*[FMQ-1] (*LA45-IH27: Series #1; LA45-IH28: Series #2)*:* The integrated $S^{6+}/\Sigma S$ peak area ratios for Series #1 and Series#2 are 0.134 and 0.086, respectively; whereas the centroid positions are 2476.291 eV and 2475.645 eV.

[FMQ] (LA45-IH1: Series #1; LA45-IH3: Series #2): The integrated $S^{6+}/\Sigma S$ peak area ratios for Series #1 and Series#2 apatite are 0.137 and 0.140. We note that the integrated $S^{6+}/\Sigma S$ peak area ratio of 0.137 differs slightly from the value reported by Konecke et al. (2017A; 0.168) and is due to the restriction of the position of the inflection point of the EMG function to a narrower energy range (e.g. from 2478-2480 eV to 2478-2479 eV; see section 3.3). The centroid positions (eV) for Series #1 and Series#2 are 2476.657 eV and 2476.123 eV, respectively.

[FMQ+0.3] (LA45-IH30: Series #1; LA45-IH34: Series #2): The integrated $S^{6+}/\Sigma S$ peak area ratios of Series #1 and Series #2 apatite are 0.504 and 0.549, respectively; and have centroid energies of 2478.443 eV and 2478.313 eV, respectively.

[FMQ+1.2] (LA45-IH7: Series #1; LA45-IH8: Series #2): Apatite from Series #1 and Series #2 have integrated $S^{6+}/\Sigma S$ peak area ratios of 0.958 and 0.925, respectively; and centroid energies of 2481.623 eV and 2481.472 eV). The integrated $S^{6+}/\Sigma S$ peak area ratios data for LA45-IH7 is from Konecke et al. (2017a).

[FMQ+3] (LA45-IH13: Series #1; LA45-IH14: Series #2): The integrated $S^{6+}/\Sigma S$ peak area ratios for Series #1 and #2 are 0.964 (data from Konecke et al., 2017a) and 0.964, respectively; whereas, the centroid positions are 2481.674 and 2481.641 eV, respectively.

4.6 DISCUSSION

4.6.1 Redox effects on $D_S^{ap/m}$

Previous studies (Baker and Rutherford, 1996; Peng et al., 1997; Parat and Holtz, 2004, 2005; Parat et al., 2008; Parat et al., 2011a, b) experimentally determined $D_S^{ap/m}$ values to be >1 for elevated fO_2 systems (e.g., where S^{6+} is the dominant oxidation state of S in the silicate melt). However, there are limited experimental data in the literature that investigate the $D_S^{ap/m}$ values under relatively intermediate-reducing conditions (e.g., <FMQ+1; Konecke et al., 2017b).

The $D_S^{ap/m}$ results for oxidized systems (e.g., $D_S^{ap/m}$ = 3.07 ±19 [Series #1] and 3.20 ±19 [Series #2] at ~FMQ+3) are consistent with previous studies; e.g., $D_S^{ap/m}$ >>1 (see Table 4.2A and 4.2B and Figure 4.2). However, the $D_S^{ap/m}$ decreases systematically with decreasing fO_2 (Figure 4.2). This observation is consistent with the presumption that apatite favors coupled-substitution mechanisms involving oxidized S compared to intermediate and/or reduced oxidation states, where: S^{6+} >> S^{2-}, while S^{4+} and S^{1+} can be incorporated in low abundances. We hypothesize that the progressive transition from incompatible (i.e., $D_S^{ap/m}$ = < 1) to compatible (i.e., $D_S^{ap/m}$ = > 1) behavior of S-in-apatite occurs once S^{6+} becomes increasingly abundant within the melt (e.g., increasing $S^{6+}/\sum S$; Jugo et al., 2010).

4.6.2 Fitting of integrated $S^{6+}/\Sigma S$ peak area ratios vs. ΔFMQ

The integrated $S^{6+}/\Sigma S$ peak area ratios were fitted as a function of fO_2 (FMQ-1 to FMQ+3) using a Boltzmann-type sigmoidal function (Figure 4.4), resulting in an R^2 = 0.99 (Figure 4.4). The fitting of the sigmoid was evaluated by plotting the calculated

integrated $S^{6+}/\Sigma S$ peak area ratios versus the measured integrated $S^{6+}/\Sigma S$ peak area ratios (Figure 4.4, insert), using equation (4.2):

$$S^{6+}/\Sigma S = 0.952\,[\pm 0.01] + \frac{(0.102\ [\pm 0.0.01] - 0.952\ [\pm 0.01])}{1 + exp^{\left(\frac{FMQ - 0.277\ [\pm 0.01]}{0.098\ [\pm 0.01]}\right)}}$$

All of the data points plot within error of the 1:1 line, and the linear regression has a R^2 value of 0.99. Hence, the calibration attempt using the integrated $S^{6+}/\Sigma S$ peak area ratio was successful. However, this integrated peak area ratio method can only yield semi-quantitative results. The application of this method becomes problematic when evaluating apatite spectra that do not contain a S^{6+} peak (e.g., $S^{6+}/\Sigma S = 0$), which precludes its applicability to natural systems (Brounce et al., in press).

4.6.3 Fitting of centroid positions (C_{eV}) vs. ΔFMQ

Here, we test centroid position (C_{eV}) as the calibration method to constrain the variability of the oxidation states of S-in-apatite as a function of the imposed fO_2 of the system. The centroid energies (C_{eV}) were fitted as a function of fO_2 (ΔFMQ) using a Boltzmann-type sigmoidal function (see equation (2); Figure 4.5), resulting in a R^2 = >0.99. The centroid calculation method, which is commonly used for Fe-XANES analyses, is the preferred method to evaluate our XANES results considering its proven robustness (Wilke et al., 2004; see Fiege et al., 2017; and references therein). The fitting of the centroid energy versus fO_2 (FMQ) can be expressed by equation (4.4):

$$C_{eV} = C_2 + \frac{(C_1 - C_2)}{1 + exp^{\left(\frac{FMQ - FMQ_0}{dFMQ}\right)}}$$

Where C_1 (2475.989 ±0.16) and C_2 (2481.659 ±0.11) are the minimum and maximum values of centroid energies calculated in this study, respectively; FMQ_0 (0.303 ±0.017) is defined by the FMQ value of the sigmoid midpoint; and dFMQ (0.114 ±0.026) defines the slope of the curve.

The fitting parameters (with 1σ error) can be substituted into equation (4.2), to define the calibration equation (4.3), where:

$$C_{eV} = 2481.659\,[\pm 0.11] + \frac{(2475.989\ [\pm 0.16] - 2481.659\,[\pm 0.11])}{1 + exp^{\left(\frac{FMQ - 0.303\ [\pm 0.017]}{0.114\ [\pm 0.026]}\right)}}$$

The calibration (eq. 3) is applicable to the reduced to intermediate fO_2 (e.g., ~FMQ-0.5 to ~FMQ+1), where centroid energies sharply increase from ~2476 eV towards higher centroid energies of ~2481 eV. The measured C_{eV} (S-XANES) versus calculated C_{eV} (calibration; eq. 3) was compared to evaluate the overall fitting (see insert in Figure 4.5). All data plot on a 1:1 line and was fit using a linear regression with a R^2 value of 0.99.

Here, we highlight that the calibration applies to measured centroid energies between ~2476.0 > C_{eV} < ~2481.6, whereas values outside this range approach end-member S^{2-} (<2476.0 eV) and S^{6+} (>2481.8 eV) centroid energies, respectively. End-member (S^{2-}: ~2474.8 eV; and S^{6+}: ~2481.8 eV) spectra were not observed in this study. Furthermore, centroid positions normalized to 0 and 1, similar to the method used by Jugo et al., (2010), as expressed by equation (4.4):

$$C_{eV} = \frac{1}{1 + exp^{\left(\frac{FMQ - FMQ_0}{dFMQ}\right)}}$$

However, it is stressed that the 0 and 1 values do not explicitly represent end-member C_{eV} conditions. Therefore, measured centroid positions that are outside of the observed range in this study cannot be used to constrain the redox conditions.

The intermediate to oxidizing experiments indicate a minor effect of the bulk S content on the centroid energy. However, a slight effect of the bulk S content on C_{eV} was observed under reducing redox conditions. This observation may be explained by the fact that in S^{2-} dominated systems, where the $S^{6+}/\Sigma S$ ratio of the melt approaches 0 (Jugo et al., 2010; Konecke et al., 2017a), sulfide is less compatible in the apatite compared to the melt based on $D_S^{ap/m}$ values (Figure 4.2; see section 5.4 for further discussion). However, when evaluating the fitting by comparing the measured C_{eV} (S-XANES) versus the calculated C_{eV} (calibration curve; equation 3), the reducing experiment performed at FMQ plots within error (e.g., where the ~±0.10 log unit error of the fO_2 determination was used to estimate the error of the calculation) of the 1:1 line (Figure 5, insert).

4.6.4 Incorporation of intermediate oxidation states (S^{1+} and S^{4+}) in apatite

Konecke et al. (2017a) first reported the presence of S^{4+} in experimental and natural apatite. Those authors demonstrated that S^{4+} observed in apatite was not due to irradiation and/or beam damage and suggested that the incorporation of S^{4+} into the apatite structure is plausibly due to a local redox reaction between apatite and silicate melt upon crystallization, where:

$$SO_4^{2-}{}_{(melt)} \Leftrightarrow SO_3^{2-}{}_{(ap)} + 0.5O_{2\,(melt)}.$$

This scenario is favored because a contribution of S^{4+} from the melt is not required, and S^{4+} incorporation into the apatite structure may serve as a mechanism to

charge balance the incorporation of S^{6+}, via: $2P^{5+} \Leftrightarrow S^{6+} + S^{4+}$ (Konecke et al., 2017a; Kim et al., 2017).

The experimental apatite that crystallized at FMQ+0.3 exhibits the presence of an intermediate S^{1+} peak (see Figure 4.3A and 4.3B). The incorporation of S^{1+} in apatite may be due to a partial oxidation of S^{2-} within the melt, and incorporated into the apatite structure similarly to other monovalent cations:

$$P^{5+} + Ca^{2+} = S^{6+} + S^{1+}$$

However, this incorporation is expected to be minor and occur over a narrow redox range. The observation that apatite incorporates two intermediate oxidation states of S (i.e., S^{1+} and S^{4+}) is consistent with, but does not directly reflect the existence of intermediate oxidation state(s) of S (S^0 and/or S^{4+}) in Fe-bearing silicate melts, as proposed by Matjuschkin et al. (2016) and Métrich et al. (2002; 2009). In other words, the incorporation of the various oxidation states of S and their relative proportions (i.e., integrated $S^{6+}/\Sigma S$ peak area ratio) in apatite likely responds to the overall redox of the melt but does not reflect the molar $S^{6+}/\Sigma S$ of the melt.

The study of Matjuschkin et al. (2016) proposed that a relatively insoluble, intermediate S oxidation state (i.e., S^0) can be present in silicate melts over a narrow range of fO_2 (~FMQ+0.2 to ~FMQ+1, depending on pressure). The authors suggest that the intermediate S^0 oxidation state does not survive upon quench, and therefore cannot be measured directly in silicate glasses.

Despite the observation that the experimentally imposed redox conditions (FMQ+0.3) fall within the range of which S^0 is theoretically stable in silicate melts (Matjuschkin et al., 2016), none of the apatite showed evidence of contribution from a S^0

peak (~2472 eV). Since the apatite structure is unlikely to incorporate S^0 due to a net neutral charge, it is plausible that S^0 is oxidized to disulfur oxide (S_2O) and incorporated in apatite following the reaction:

$$2S^0 + 0.5\ O_2 \Leftrightarrow S_2O_{(apatite)}.$$

A similar reaction has been proposed to explain the origin of volcanic S_2O emissions on Jupiter's moon Io (Zolotov and Fegley, 1998). It is noted here that the peak position of the inferred S^{1+} peak (~2472.9 eV) does not overlap with the shoulder of the broad S^{2-} peak (~2476.3 eV). Alternatively, the presence of S^{1+} in the apatite structure may indicate that the "insoluble" S species responsible for the "sulfur solubility minimum" in silicate melts (Matjuschkin et al., 2016) is also S^{1+}. We suggest that incorporation of a SO_2^+ complex in the melt structure is more likely than the incorporation of a neutral S^0 species.

4.6.5 Incorporation of S^{6+} in apatite under reducing conditions

The abundance and stability of S^{6+} and S^{2-} in a silicate melt is a function of the P-T-fO_2 (Jugo et al., 2010; Matjuschkin et al., 2016; and references therein). However, the observation that apatite incorporates S^{6+} under reducing conditions, e.g., where $S^{6+}/\sum S$ of the melt approaches 0, has interesting implications for the behavior of S between apatite and melt. A first order explanation is that exceedingly low abundances of S^{6+} (i.e., below the limit of detection for S-XANES analyses of glasses) can be present in reduced silicate melts (≤FMQ). Given the preference of $S^{6+} >> S^{2-}$, apatite will incorporate greater proportions of S^{6+} compared to S^{2-}. The presence of S^{6+} in apatite that crystallizes from a reduced silicate melt may reflect a non-zero, but nominal abundance of S^{6+}. This behavior is plausibly explained by the compatible behavior of sulfate ($D_S^{ap/m} >> 1$) and

the incompatible behavior of sulfide ($D_S^{ap/m} < 0.1$). Thus, even in the presence of increasingly low, undetectable fractions of sulfate in the melt, the sulfate is often still abundant in apatite. As a fortunate consequence, the ability of apatite to contain S^{6+} at lower oxygen fugacities compared to what can be measured in the melt, allows for a more precise oxybarometer for relatively more reducing conditions (~FMQ-0.5 to ~FMQ+1).

4.6.6 Application of S-in-apatite oxybarometer to natural systems

At fixed oxygen fugacity, the difference between the stability of mineral buffers such as nickel-nickel oxide (ΔNNO) and fayalite-magnetite-quartz (ΔFMQ) is defined by T, and to a minor degree P (Candela, 1986; Jugo et al., 2005). While numerous experimental studies have investigated the solubility of S in silicate melts as a function of T-P-X-fO_2-fS_2-H_2O (see Fortin et al., 2015; Baker and Moretti, 2011, and references therein), the oxidation states of S in silicate melts are more strongly affected by P, compared to T (Matjuschkin et al., 2016). Matjuschkin et al. (2016) modeled literature and experimental data and concluded that increasing pressure (from 200 MPa to 1500 MPa) results in a shift of the stability of S^{2-} in the melt to more oxidizing conditions.

Considering that the experiments in this study were conducted at a single pressure (300 MPa), they do not directly constrain whether this observed pressure effect for silicate glasses could be extrapolated to the S-in-apatite oxybarometer. In a scenario where the P effect observed in silicate glass is proportional for S-in-apatite, then a pressure shift from 200 MPa to 500 MPa would result in a maximum deviation of a ΔFMQ of ~0.4 log units fO_2. However, until a S-in-apatite calibration is developed over a range of pressures, the results should be interpreted with caution if the pressure conditions of the natural systems deviate significantly from this study.

The accurate estimation of fO_2 in magmatic environments constitutes a difficult geochemical challenge, and is compounded for systems that either: [1] do not contain the necessary constituents for fO_2 determination (e.g., Fe-Ti oxide pairs and/or silicate glass); and/or [2] have undergone S degassing, which has been shown by several studies to modify the fO_2 (Burgisser and Scaillet, 2007; Kelley and Cottrell, 2012; De Moor et al., 2013). However, considering that apatite can be a near liquidus and/or near solidus phase in silicate melts, combined with the ability to preserve inter-and-intra zonation with respect to S signatures (Streck and Dilles 1998; Konecke et al., 2017a, b; Economos et al., 2017), the S-in-apatite oxybarometer is a powerful alternative for estimating the redox conditions and evolution of magmatic systems.

When applied to natural systems of similar T-P-X conditions used in this study, the experimentally calibrated S-in-apatite oxybarometer is highly sensitive to the redox conditions that span from ~FMQ-0.5 to ~FMQ+1 (Figure 4.6). This redox range is particularly relevant for mid ocean ridge basalt (MORB), and relatively reducing ocean island basalt (OIB) and backarc basin basalt (BABB) systems (Jugo et al., 2010; Evans et al., 2012). However, despite the relatively limited range of precision (~1.5 log units fO_2), the calibration can provide a minimum redox estimate for the system; e.g., <FMQ-0.5 or >FMQ+1.

4.7 CONCLUSIONS

The S content of apatite, $D_S^{ap/m}$, and centroid values (C_{eV}) increase systematically with increasing fO_2, indicating that apatite favors substitution mechanisms involving oxidized S compared to intermediate and reduced oxidation states. These results show that the concentration of S and the oxidation state(s) in apatite can be used as a proxy for

the redox conditions, and to constrain the S content of the melt at the time of apatite crystallization. The high spatial resolution of S-XANES analyses (2 x 1 um) combined with the high precision estimation of the oxidation states of S and the inter-and-intra crystalline zonation of S-in-apatite can be used to trace the evolution of redox and S content in magmatic systems. The S-in-apatite oxybarometer presented here is particularly sensitive for mafic systems where the fO_2 ranges from ~FMQ-0.5 to ~FMQ+1, such as MORB, as well as relatively reduced OIB and BABB systems. Ultimately, coupling of redox and substitution mechanisms requires that the fO_2 of the system be constrained *before* applying $D_S^{ap/m}$ to accurately determine the S content of a pre-degassed melt. Alternatively, the S concentration of apatite can be used as a first order constraint on the prevailing oxygen fugacity when using solubility models to estimate the sulfide or sulfate solubility in coexisting melts (Konecke et al., 2017b).

Table 4.1: Experimental conditions

Series #	Run name	T (°C)	P (MPa)	fO_2 (ΔFMQ)	Duration (hr)	Bulk S (wt. %)	Source of S
1	LA45-IH27	1,000	300	-1	120	0.37	1 wt.% po.
	LA45-IH1	1,000	300	0	72	0.37	1 wt.% po.
	LA45-IH30	1,000	300	0.3	120	0.37	1 wt.% po.
	LA45-IH7	1,000	300	1.2	120	0.37	1 wt.% po.*
	LA45-IH13	1,000	300	3	120	0.37	1 wt.% po.*
2	LA45-IH28	1,000	300	-1	120	0.28	0.75 wt.% po.
	LA45-IH2	1,000	300	0	72	0.28	0.75 wt.% po.
	LA45-IH34	1,000	300	0.3	120	0.28	0.75 wt.% po.
	LA45-IH8	1,000	300	1.2	120	0.28	0.75 wt.% po.**
	LA45-IH14	1,000	300	3	120	0.28	0.75 wt.% po.**

Starting glass material compostions from Konecke et al. (2017a)

*~0.37 wt.% S (elemental) + ~0.92 wt.% Fe_2O_3, where the Fe/S ratio corresponds to pyrrhotite (po.)

**~0.27 wt.% S (elemental) + ~0.69 wt.% Fe_2O_3, where the Fe/S ratio corresponds to pyrrhotite (po.)

Table 4.2A: EPMA results for experimental Series #1 apatites & glass

	LA45-IH27	LA45-IH27	LA45-IH1 §	LA45-IH1 §	LA45-IH30	LA45-IH30	LA45-IH7§	LA45-IH7§	LA45-IH13§	LA45-IH13§
wt.%	Ap	Glass	Ap	Glass	Ap	Glass	Ap	Glass	Ap	Glass
SiO_2	1.50 ±0.23	46.26 ±0.58	1.73 ±0.22	43.50 ±0.22	1.18 ±0.18	46.36 ±0.46	1.55 ±0.02	46.98 ±0.12	1.79 ±0.07	49.71 ±0.53
TiO_2	0.10 ±0.04	2.82 ±0.10	0.04 ±0.01	2.64 ±0.05	0.03 ±0.01	2.04 ±0.05	0.09 ±0.02	2.33 ±0.07	0.05 ±0.01	1.47 ±0.29
Al_2O_3	0.12 ±0.06	14.12 ±.26	0.47 ±0.28	12.71±0.17	0.02 ±0.02	13.99 ±0.01	0.13 ±0.04	13.27 ±0.05	0.05 ±0.01	14.31 ±0.63
FeO	0.56 ±0.04	9.12 ±0.17	0.59 ±0.06	9.30 ±0.17	0.50 ±0.03	10.18 ±0.28	0.53 ±0.04	8.81 ±0.08	0.38 ±0.02	4.32 ±0.38
MgO	0.14 ±0.03	2.33 ±0.63	0.25 ±0.11	1.68 ±0.10	0.13 ±0.04	1.00 ±0.05	0.17 ±0.02	1.97 ±0.05	0.24 ±0.06	3.70 ±0.72
MnO	b.d.	0.31 ±0.02	b.d.	0.30 ±0.02	b.d.	0.36 ±0.01	0.01 ±0.01	0.28 ±0.02	0.01 ±0.01	0.15 ±0.02
CaO	53.09 ±0.30	8.91 ±0.51	53.00 ±0.32	9.00 ±0.23	53.50 ±0.25	8.09 ±0.29	53.34 ±0.20	8.64 ±0.07	53.49 ±0.15	0.89 ±0.28
K_2O	0.28 ±0.03	7.37 ±0.20	0.29 ±0.03	8.93 ±0.04	0.20 ±0.02	8.18 ±0.09	0.29 ±0.03	7.28 ±0.09	0.20 ±0.01	10.99 ±0.66
Na_2O	b.d.	1.36 ±0.05	0.01 ±0.01	1.58 ±0.04	b.d.	1.31 ±0.05	0.01 ±0.01	1.30 ± 0.04	b.d.	1.35 ± 0.07
P_2O_5	39.65 ±0.25	0.38 ±0.03	39.30 ±0.17	0.91 ±0.22	40.14 ±0.21	0.44 ±0.12	39.32 ±0.20	0.57 ±0.02	38.17 ±0.19	5.18 ±1.40
Ce_2O_3	0.57 ±0.03	n.a.	0.54 ±0.02	n.a.	0.53 ±0.03	n.a.	0.35 ±0.02	n.a.	0.47 ±0.03	n.a.
La_2O_3	b.d.	n.a.	0.23 ±0.01	n.a.	b.d.	n.a.	0.11 ±0.03	b.d.	0.21 ±0.01	n.a.
F	1.26 ±0.07	b.d.	1.43 ±0.05	0.39 ±0.11	1.41 ±0.07	b.d.	1.37 ±0.04	0.30 ±0.11	1.34 ±0.04	0.05 ±0.05
Cl	b.d.	b.d.	b.d.	0.01 ±0.01	b.d.	b.d.	b.d.	b.d.	b.d.	b.d.
SO_3	-	0.55 ±0.04	-	0.64 ±0.05	-	0.73 ±0.03	-	1.14 ±0.02	-	0.40 ±0.06
S (ap)	0.004 ±0.001	0.22 ±0.01	0.03 ±0.00	-	0.06 ±0.00	-	0.30 ±0.02	-	0.49 ±0.02	-
SrO	1.17 ±0.02	n.a.	0.94 ±0.02	n.a.	0.93 ±0.03	n.a.	0.76 ±0.04	n.a.	1.11 ±0.02	n.a.
BaO	n.a.	n.a.	0.02 ±0.01	0.50 ±0.04	n.a.	n.a.	b.d.	0.07 ±0.03	b.d.	0.54 ±0.13
O=F, Cl	0.53	-	0.6	-	0.59	-	0.58	-	0.56	-
Total	100.09 ±0.36	93.57 ±0.30	100.44 ±0.26	92.08 ±0.26	100.13 ±0.22	93.69 ±0.46	100.35 ±0.17	92.93 ±0.15	100.30 ±0.15	93.05 ±0.28
H_2O (mass balance)	2.17*	6.43 ±0.30	2.12*	7.92 ±0.26	2.04*	6.31 ±0.46	2.17*	7.07 ±0.15	2.20*	6.95 ±0.28
S (µg/g)	44 ±25	2230 ±156	322 ±44	2553 ±200	556 ±47	2918 ±127	2982 ±174	4548 ±71	4935 ±172	1609 ±257
$D_s^{ap/m}$	0.02 ±0.01		0.13 ±0.02		0.19 ±0.02		0.66 ±0.04		3.07 ±0.19	
# of analyses	9	12	10	7	10	10	11	10	7	7

Notes: b.d. is below detection limit; n.a. is not analyzed
*Calculated assuming halogen site filled with F + Cl + OH (Ketchum, 2015)

Analyses given in 1σ standard error of mean

O=F, Cl is correction factor
**~0.35 wt.% S (elemental) + ~0.92 wt.% Fe_2O_3, where the Fe/S ratio corresponds to po.
§ Data from Konecke et al., 2017a
S (ap) = S reported in wt.%

Table 4.2B: EPMA results for experimental Series #2 apatites & glass

wt.%	LA45-IH28 Ap	LA45-IH28 Glass	LA45-IH2 Ap	LA45-IH2 Glass	LA45-IH34 Ap	LA45-IH34 Glass	LA45-IH8 Ap	LA45-IH8 Glass	LA45-IH14 Ap	LA45-IH14 Glass
SiO_2	1.19 ±0.08	45.86 ±0.30	1.31 ±0.10	45.21 ±0.27	1.00 ±0.03	44.71 ±0.17	1.52 ±0.13	47.20 ±0.20	1.81 ±0.28	53.61 ±0.82
TiO_2	0.04 ±0.01	2.82 ±0.05	0.04 ±0.01	2.56 ±0.01	0.04 ±0.01	3.09 ±0.02	0.03 ±0.02	2.73 ±0.11	0.05 ±0.03	0.48 ±0.04
Al_2O_3	0.05 ±0.01	13.71 ±0.27	0.07 ±0.02	14.55 ±0.34	0.02 ±0.01	12.90 ±0.06	0.06 ±0.04	13.19 ±0.32	0.11 ±0.10	18.25 ±0.90
FeO	0.46 ±0.01	9.34 ±0.18	0.47 ±0.01	9.48 ±0.19	0.48 ±0.01	10.59 ±0.11	0.52 ±0.03	8.58 ±0.08	0.44 ±0.08	2.22 ±0.08
MgO	0.09 ±0.01	2.15 ±0.30	0.13 ±0.02	1.35 ±0.06	0.11 ±0.01	1.91 ±0.03	0.19 ±0.04	2.29 ±0.34	0.29 ±0.16	0.43 ±0.29
MnO	b.d.	0.30 ±0.03	0.01 ±0.01	0.32 ±.02	b.d.	0.33 ±0.01	b.d.	0.29 ±0.03	b.d.	0.02 ±0.02
CaO	52.84 ±0.12	10.00 ±0.36	52.70 ±0.15	9.04 ±0.14	54.11 ±0.41	9.53 ±0.10	53.74 ±0.34	8.81 ±0.46	52.79 ±0.36	3.15 ± 0.82
K_2O	0.23 ±0.02	6.49 ±0.21	0.26 ±0.03	7.22 ±0.18	0.25 ±0.02	7.14 ±0.08	0.23 ±0.03	7.23 ±0.18	0.20 ±0.06	10.75 ±0.45
Na_2O	b.d.	1.23 ± 0.04	b.d.	1.28 ±.05	b.d.	1.10 ± 0.03	b.d.	1.34 ±0.04	b.d.	1.22 ±0.04
P_2O_5	40.21 ±0.12	0.45 ±0.03	39.74 ±0.15	0.47 ±0.03	40.13 ±0.26	0.52 ±0.03	39.30 ±0.27	0.51 ±0.02	38.79 ±0.31	1.01 ±0.63
Ce_2O_3	0.61 ±0.02	n.a.	0.58 ±0.03	n.a.	0.48 ±0.03	b.d.	0.45 ±0.03	n.a.	0.49 ±0.02	n.a.
La_2O_3	b.d.	n.a.	0.24 ±0.02	n.a.	b.d.	b.d.	b.d.	n.a.	0.23 ±0.04	n.a.
F	1.28 ±0.05	b.d.	1.45 ±0.06	b.d.	1.43 ±0.05	b.d.	1.44 ±0.05	0.23 ±0.10	1.38 ±0.05	n.a.
Cl	b.d.	b.d.	b.d.	b.d.	0.01 ±0.01	0.01 ±0.01	b.d.	0.01 ±0.01	b.d.	b.d.
SO_3	-	0.57 ±0.03	-	0.43 ±0.02	-	0.70 ±0.01	-	0.76 ±0.02	-	0.39 ±0.06
S (ap)	0.004 ±0.00	-	0.01 ±0.01	-	0.09 ±0.01	-	0.27 ±0.02	-	0.49 ±0.01	-
SrO	1.05 ±0.03	n.a.	1.01 ±0.03	n.a.	0.92 ±0.04	n.a.	0.74 ±0.03	n.a.	1.11 ±0.04	n.a.
BaO	n.a.	n.a.	n.a.	0.57 ±0.03	n.a.	n.a.	n.a.	0.10 ±0.04	b.d.	0.27 ±0.08
O=F, Cl	0.54	-	0.61	-	0.61	-	0.61	-	0.58	-
Total	99.45 ±0.25	93.73 ±0.65	99.40 ±0.22	92.51 ±0.35	100.64 ±0.50	92.52 ±0.21	98.48 ±0.51	93.31 ±0.42	99.68 ±0.35	91.70 ±1.05
H_2O (mass balance)	2.15*	6.27 ±0.65	1.99*	7.49 ±0.35	2.02*	7.05 ±0.21	2.01	6.69 ±0.42	2.07*	8.30 ±1.05
S (µg/g)	39 ±12	2300 ±121	161 ±15	1739 ±76	903 ±58	2795 ±66	2730 ±212	3040 ±94	4958 ±152	1548 ±225
$D_s^{ap/m}$	0.02 ±0.01		0.09 ±0.02		0.32 ±0.02		0.90 ±0.04		3.20 ±0.19	
# of analyses	10	8	8	11	8	16	8	10	12	5

Notes: b.d. is below detection limit; n.a. is not analyzed
*Calculated assuming halogen site filled with F + Cl + OH (Ketchum, 2015)
Analyses given in 1σ standard error of mean
O=F, Cl is correction factor
**~0.35 wt.% S (elemental) + ~0.92 wt.% Fe_2O_3, where the Fe/S ratio corresponds to po.
§ Data from Konecke et al., 2017a
S (ap) = S reported in wt.%

Table 4.3: Sulfur XANES results for experimental apatite

Run name	fO_2 (ΔFMQ)	$S^{6+}/\Sigma S$	C_{eV}	Oxidation States
LA45-IH27	-1	0.134	2476.291	S^{2-}, S^{6+}
LA45-IH1	0	0.137	2476.657	S^{2-}, S^{6+}
LA45-IH30	0.3	0.504	2478.443	S^{2-}, S^{1+}, S^{4+}, S^{6+}
LA45-IH7	1.2	0.958	2481.623	S^{4+}, S^{6+}
LA45-IH13	3	0.964	2481.675	S^{4+}, S^{6+}
LA45-IH28	-1	0.086	2475.645	S^{2-}, S^{6+}
LA45-IH2	0	0.14	2476.123	S^{2-}, S^{6+}
LA45-IH34	0.3	0.549	2478.313	S^{2-}, S^{1+}, S^{4+}, S^{6+}
LA45-IH8	1.2	0.925	2481.472	S^{4+}, S^{6+}
LA45-IH14	3	0.964	2481.641	S^{4+}, S^{6+}

Note: C_{eV} = centroid position

Oxidation states determined from S-XANES absorption peaks

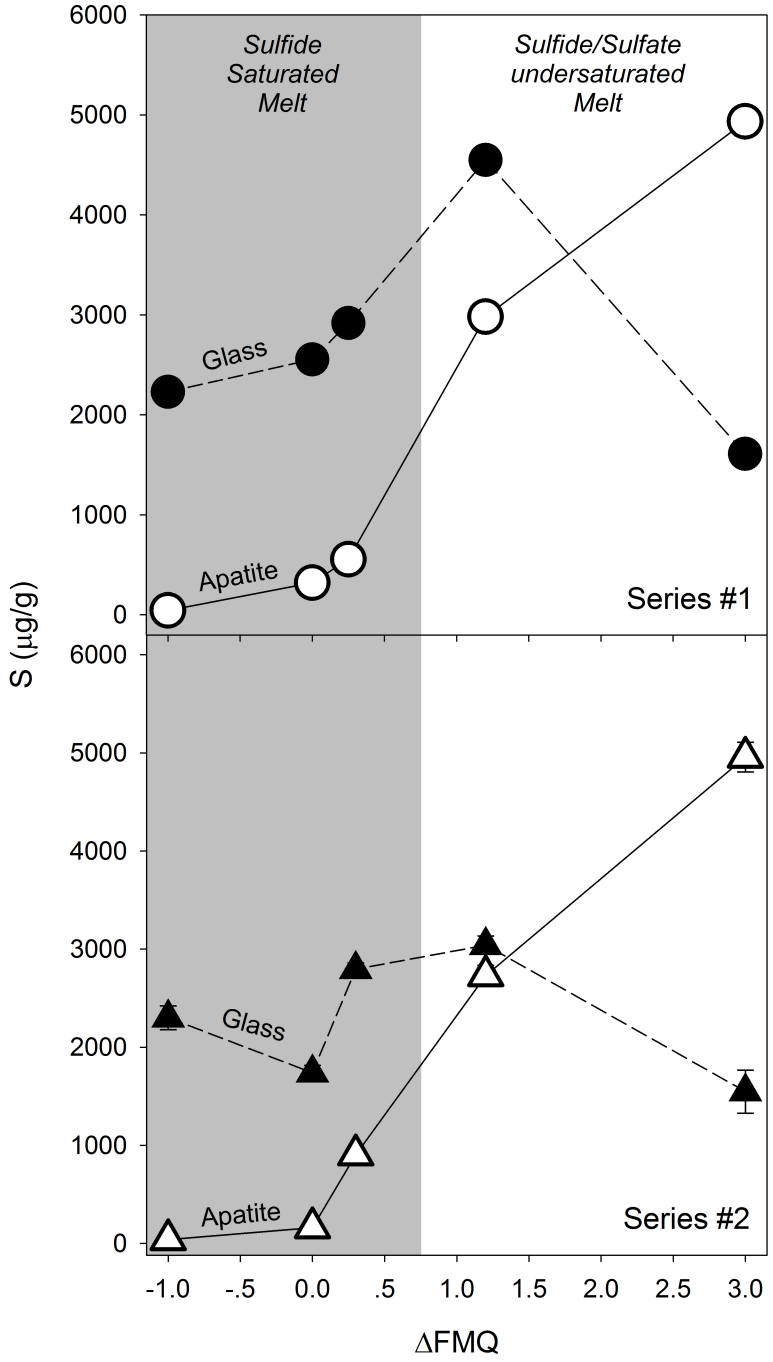

Figure 4.1: Sulfur contents (µg/g S) of experimental apatite and co-existing glass versus fO_2 (ΔFMQ). Panel A: The open circles and closed circles represent the apatite and glass data for Series #1, respectively. Panel B: The open triangles and closed triangles represent the apatite and glass data for Series #1, respectively. The gray box indicates the range of fO_2 of which the experiments where the melt was sulfide saturated. Error bars represent 1σ standard error.

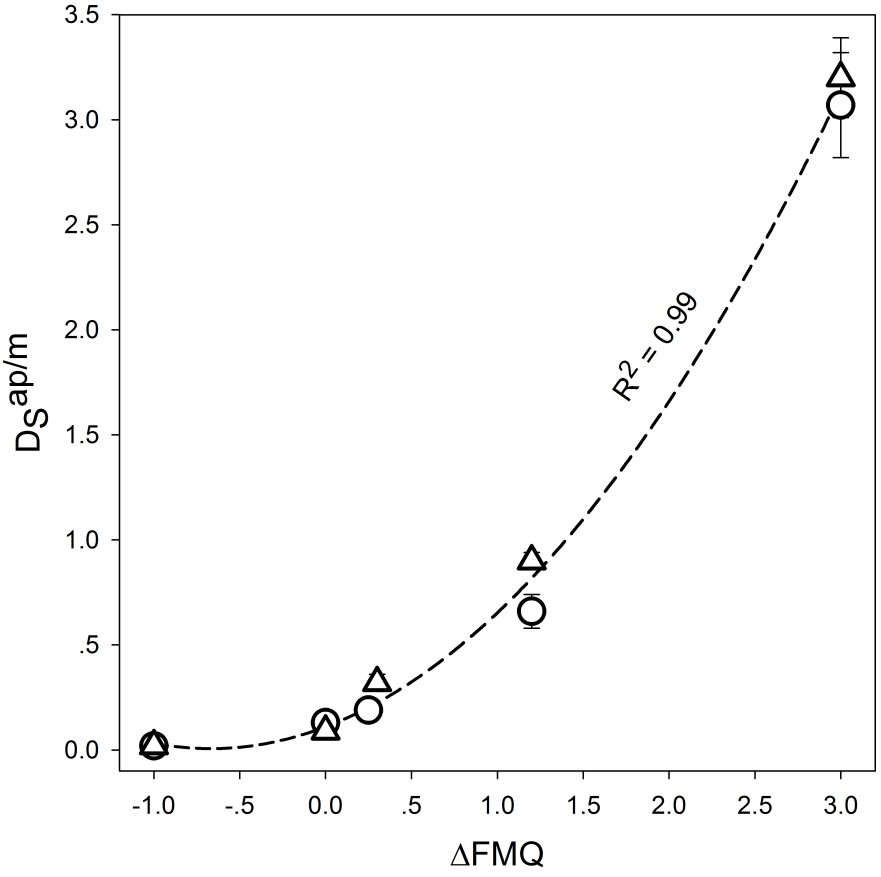

Figure 4.2: Partition coefficients for S between apatite and melt ($D_S^{ap/m}$) as a function of fO_2 (ΔFMQ). The open circles and open triangles denote the Series #1 and Series #2 experiments, respectively. The $D_S^{ap/m}$ increases systematically with increasing ΔFMQ. A polynomial function was used to fit the data (R^2 value of 0.99). Error bars represent 2σ standard error (see Table 4.2A and 4.2B).

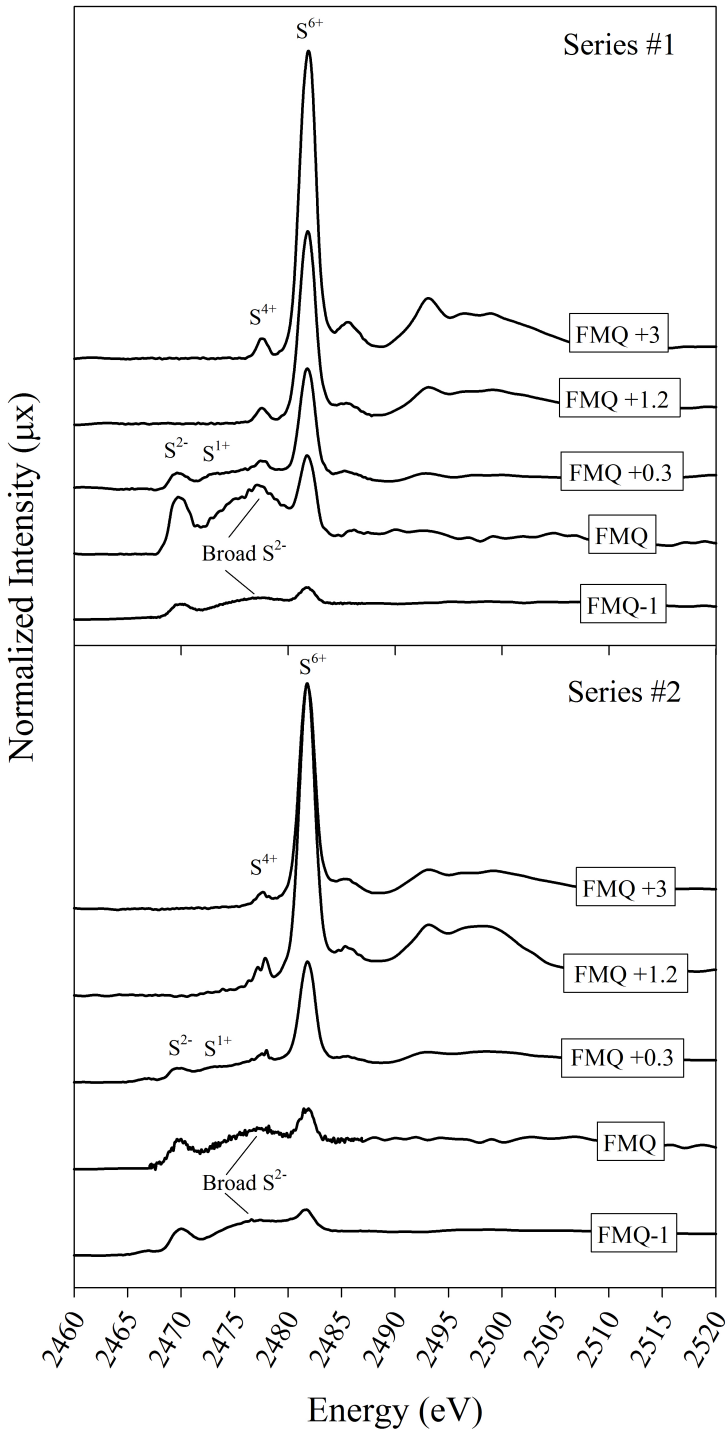

Figure 4.3: Sulfur μ-XANES spectra of apatite from experiments performed at different redox conditions. Normalized and merged S-XANES spectra of Series #1 (panel A) and Series #2 (panel B) apatite arranged by the imposed fO_2 conditions. Spectra of experimental apatite crystallized at FMQ-1 and FMQ both contain S^{2-} (sharp peak: ~2469.8 eV; broad peaks: ~2476.5 eV), and S^{6+} (~2481.8 eV) peaks. Spectra from apatite crystallized at slightly reducing-intermediate redox conditions of FMQ+0.3 exhibit S^{2-}

(2469.7 eV, sharp; and 2476.7, broad), S^{6+} (2481.8 eV), S^{4+}(~2477.5 eV), and a minor peak consistent with the peak position of S^{1+} (2472.9 eV). Apatite crystallized under slightly oxidized (FM+1.2) and oxidized conditions (FMQ+3) reveal S^{6+} (~2481.8 eV), and S^{4+} (~2477.5 eV). Apatite data from experiments performed at FMQ are from Konecke et al., (2017a and b), while data at FMQ+1.2, and FMQ+3 are from Konecke et al. (2017a).

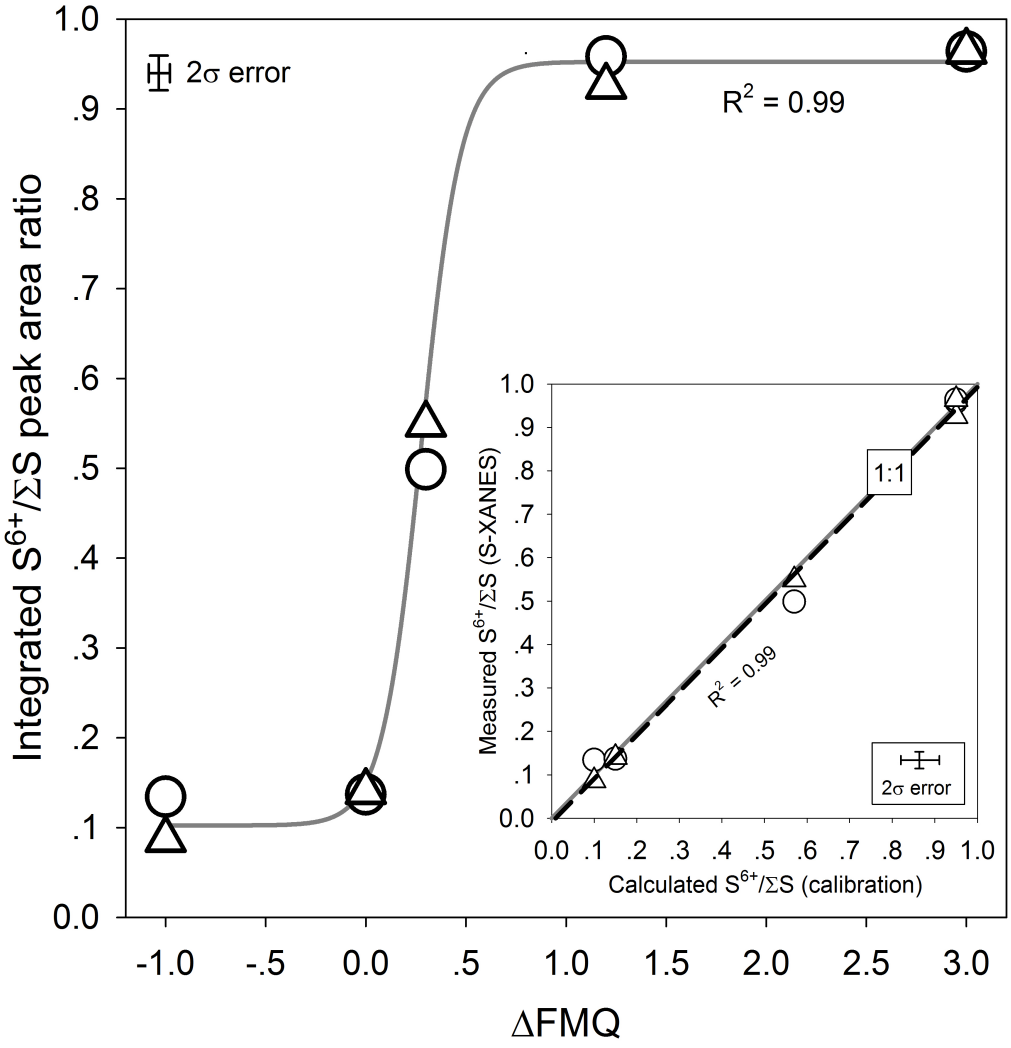

Figure 4.4: Integrated $S^{6+}/\sum S$ peak area ratios plotted versus fO_2 (ΔFMQ). The open circles and open triangles denote the Series #1 and Series #2 experiments, respectively. The data were fitting using a sigmoidal calibration function (R^2 = 0.99), and the error bars represent 2σ standard error. Insert: The measured integrated $S^{6+}/\sum S$ peak area ratios are plotted against the calculated integrated $S^{6+}/\sum S$ peak area ratios derived from the sigmoidal function. The solid black line represents a 1:1 relationship, whereas the dashed black line is the linear fitting of the data (R^2 = 0.99). All data points plot within error of the 1:1 line. Error bars are 2σ standard error.

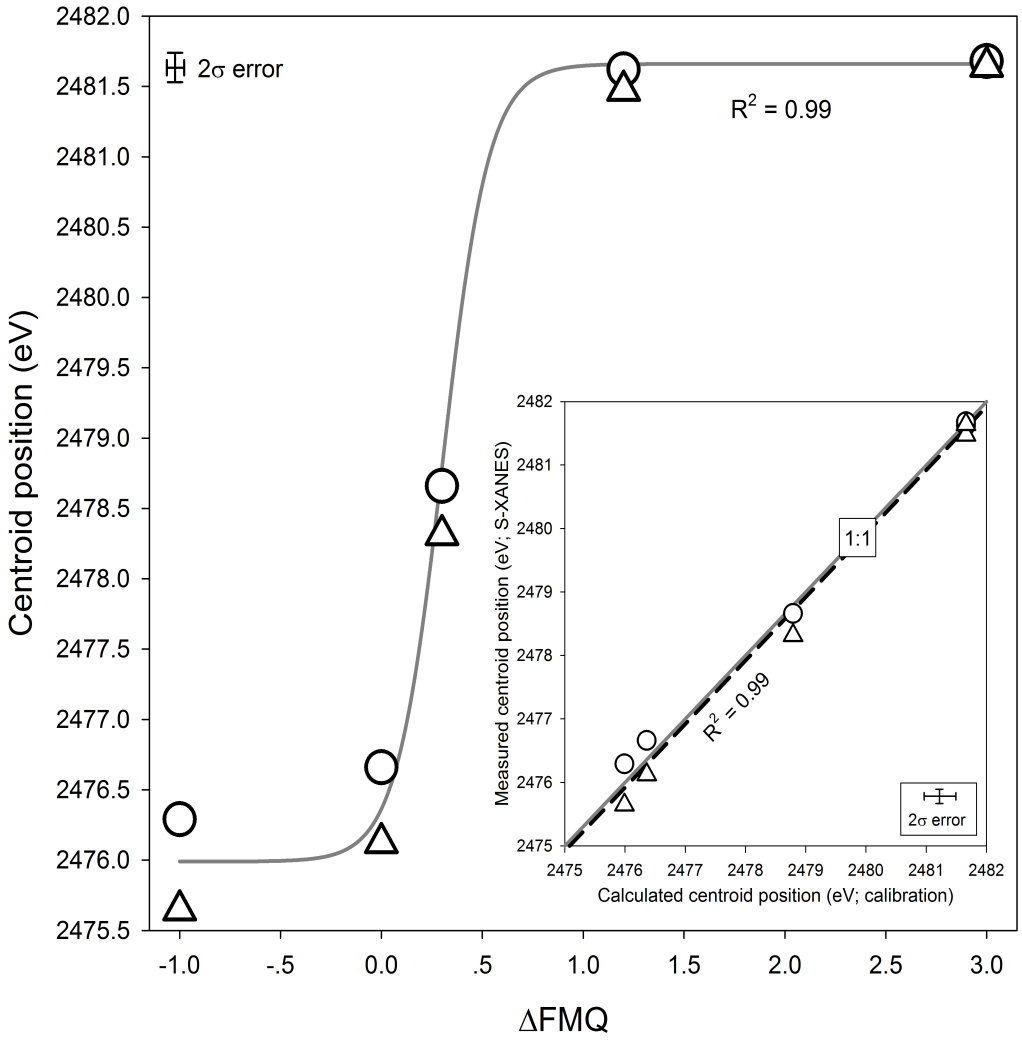

Figure 4.5: Centroid positions (C_{eV}) versus ΔFMQ. The open circles and open triangles denote the Series #1 and Series #2 experiments, respectively. The data were fitting using a sigmoidal calibration function (R^2 = 0.99), and the error bars represent 2σ standard error. Insert: The measured centroid positions are plotted against the calculated centroid positions derived from the sigmoidal function. The solid black line represents a 1:1 relationship, whereas the dashed black line is the linear fitting of the data (R^2 = 0.99). Error bars are 2σ standard error.

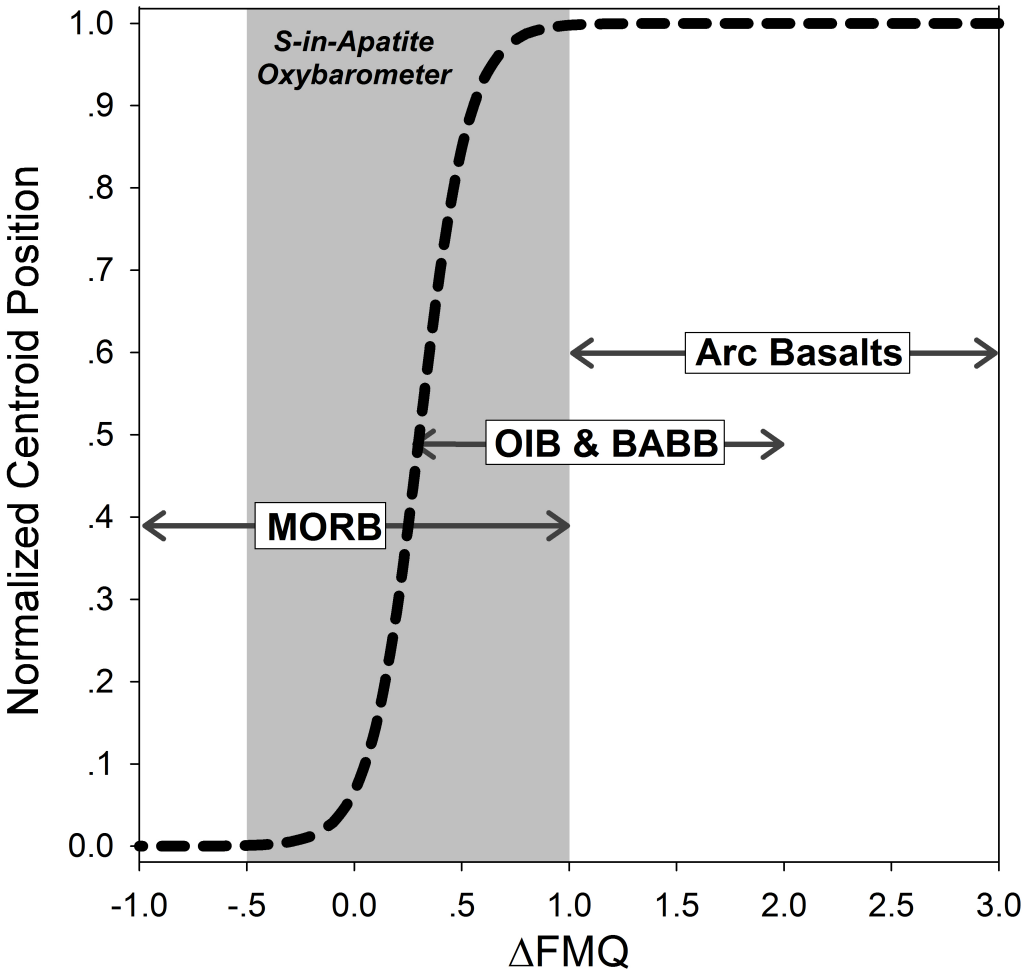

Figure 4.6: Applicability of S-in-apatite oxybarometer, using normalized centroid position versus fO_2 (ΔFMQ). The arrows denote the redox range for mid-ocean ridge basalt (MORB), ocean island basalt (OID), backarc basin basalt (BABB), and arc basalts (redox ranges from Jugo et al., 2010 and Evans et al., 2012). The gray box represents the redox range of which the S-in-apatite oxybarometer is sensitive to constraining the fO_2 of mafic systems. Note: the normalized centroid positions that plot outside this range can provide minimum/maximum constraints of the fO_2.

4.8 REFERENCES

Baker D. R. and Moretti R. (2011) Modeling the Solubility of Sulfur in Magmas: A 50-Year Old Geochemical Challenge. Rev. Mineral. Geochemistry 73, 167–213.

Barré G., Truche L., Bazarkina E. F., Michels R. and Dubessy J. (2017) First evidence of the trisulfur radical ion S 3 − and other sulfur polymers in natural fluid inclusions. Chem. Geol. 462, 1–14.

Bell, Shearer, Burger, Ren, Newville and Lanzirotti (2017) Quantifying and correcting the effects of anisotropy in XANES measurements of chromium valence in olivine: Implications for a new olivine oxybarometer. Am. Mineral. 102, 1165-1172.

Berndt J., Liebske C., Holtz F., Freise M., Nowak M., Ziegenbein D., Hurkuck W. and Koepke J. (2002) A combined rapid-quench and H2-membrane setup for internally heated pressure vessels: Description and application for water solubility in basaltic melts. Am. Mineral. 87, 1717–1726.

Berry A. J., O'Neill H. S. C., Jayasuriya K. D., Campbell S. J. and Foran G. J. (2003) XANES calibrations for the oxidation state of iron in a silicate glass. Am. Mineral. 88, 967–977.

Berry A. J., Stewart G. A., O'Neill H. S. C., Mallmann G. and Mosselmans J. F. W. (2018) A re-assessment of the oxidation state of iron in MORB glasses. Earth Planet. Sci. Lett. 483, 114–123.

Brounce M., Boyce J., McCubbin F., Humphreys J., Reppart J., Stolper E. and Eiler J. (in press) The oxidation state of sulfur in lunar apatite. Am. Mineral.

Burgisser A., Alletti M. and Scaillet B. (2015) Simulating the behavior of volatiles belonging to the C–O–H–S system in silicate melts under magmatic conditions with the software D-Compress. Comput. Geosci. 79, 1–14.

Burgisser A. and Scaillet B. (2007) Redox evolution of a degassing magma rising to the surface. Nature 445, 194–197.

Candela P. A. (1986) The evolution of aqueous vapor from silicate melts: Effect on oxygen fugacity. Geochim. Cosmochim. Acta 50, 1205–1211.

Chelle-Michou C. and Chiaradia M. (2017) Amphibole and apatite insights into the evolution and mass balance of Cl and S in magmas associated with porphyry copper deposits. Contrib. to Mineral. Petrol. 172, 105.

Cottrell E., Lanzirotti A., Mysen B., Birner S., Kelley K. A., Botcharnikov R. E., Davis F. A. and Newville M. (2018) A mossbauer-based XANES calibration for

hydrous basalt glasses reveals radiation-induced oxidation of Fe. Am. Mineral, 489–501.

Cottrell E., Kelley K. A., Lanzirotti A. and Fischer R. A. (2009) High-precision determination of iron oxidation state in silicate glasses using XANES. Chem. Geol. 268, 167–179.

De Moor J. M., Fischer T. P., Sharp Z. D., King P. L., Wilke M., Botcharnikov R. E., Cottrell E., Zelenski M., Marty B., Klimm K., Rivard C., Ayalew D., Ramirez C. and Kelley K. A. (2013) Sulfur degassing at Erta Ale (Ethiopia) and Masaya (Nicaragua) volcanoes: Implications for degassing processes and oxygen fugacities of basaltic systems. Geochemistry, Geophys. Geosystems 14, 4076–4108.

Dyar M. D., Gunter M. E., Delany J. S., Lanzarotti A. A. and Sutton S. R. (2002) Systematics in the structure and XANES spectra of pyroxenes, amphiboles, and micas as derived from oriented single crystals. Can. Mineral. 40, 1375–1393.

Economos R., Boehnke P. and Burgisser A. (2017) Sulfur isotopic zoning in apatite crystals: A new record of dynamic sulfur behavior in magmas. Geochim. Cosmochim. Acta 215, 387–403.

Evans K. A. (2006) Redox decoupling and redox budgets: Conceptual tools for the study of earth systems. Geology 34, 489–492.

Evans K. A., Dyar M. D., Reddy S. M., Lanzirotti A., Adams D. T. and Tailby N. (2014) Variation in XANES in biotite as a function of orientation, crystal composition, and metamorphic history. Am. Mineral. 99, 443–457.

Fiege A., Behrens H., Holtz F. and Adams F. (2014) Kinetic vs. thermodynamic control of degassing of H2O–S±Cl-bearing andesitic melts. Geochim. Cosmochim. Acta 125, 241–264.

Fiege A., Ruprecht P., Simon A. C., Bell A. S., Göttlicher J., Newville M., Lanzirotti T. and Moore G. (2017) Calibration of Fe XANES for high-precision determination of Fe oxidation state in glasses: Comparison of new and existing results obtained at different synchrotron radiation sources. Am. Mineral. 102, 369–380.

Fortin M. A., Riddle J., Desjardins-Langlais Y. and Baker D. R. (2015) The effect of water on the sulfur concentration at sulfide saturation (SCSS) in natural melts. Geochim. Cosmochim. Acta 160, 100–116.

Ghiorso M. S. and Evans B. W. (2008) Thermodynamics of Rhombohedral Oxide Solid Solutions and a Revision of the FE-TI Two-Oxide Geothermometer and Oxygen-Barometer. Am. J. Sci. 308, 957–1039.

Goldoff B., Webster J. D. and Harlov D. E. (2012) Characterization of fluor-chlorapatites by electron probe microanalysis with a focus on time-dependent intensity variation of halogens. Am. Mineral. 97, 1103–1115.

Harlov D. E. (2015) Apatite: A Fingerprint for Metasomatic Processes. Elements 11, 171–176.

Head E., Lanzirotti A., Newville M. and Sutton S. (2018) Vanadium, sulfur, and iron valences in melt inclusions as a window into magmatic processes: A case study at Nyamuragira volcano, Africa. Geochim. Cosmochim. Acta 226, 149–173.

Huston D. L., Pehrsson S., Eglington B. M. and Zaw K. (2010) The geology and metallogeny of volcanic-hosted massive sulfide deposits: Variations through geologic time and with tectonic setting. Econ. Geol. 105, 571–591.

Jugo P. J. (2004) An Experimental Study of the Sulfur Content in Basaltic Melts Saturated with Immiscible Sulfide or Sulfate Liquids at 1300C and 1 GPa. J. Petrol. 46, 783–798.

Jugo P. J., Luth R. W. and Richards J. P. (2005) Experimental data on the speciation of sulfur as a function of oxygen fugacity in basaltic melts. Geochim. Cosmochim. Acta 69, 497–503.

Jugo P. J., Wilke M. and Botcharnikov R. E. (2010) Sulfur K-edge XANES analysis of natural and synthetic basaltic glasses: Implications for S speciation and S content as function of oxygen fugacity. Geochim. Cosmochim. Acta 74, 5926–5938.

Kelley K. A. and Cottrell E. (2009) Water and the Oxidation State of Subduction Zone Magmas. Science (80-) 325.

Kim Y., Konecke B., Fiege A., Simon A. and Becker U. (2017) An ab-initio study of the energetics and geometry of sulfide, sulfite and sulfate incorporation into apatite: The thermodynamic basis for using this system as an oxybarometer.

Konecke B. A., Fiege A., Simon A. C., Parat F. and Stechern A. (2017a) Co-variability of S^{6+}, S^{4+}, and S^{2-} in apatite as a function of oxidation state: Implications for a new oxybarometer. Am. Mineral. 102, 548–557.

Konecke B. A., Fiege A., Simon A. C., and Holtz F. (2017b) Cryptic metasomatism during late-stage lunar magmatism implicated by sulfur in apatite. Geology 45, 739–742.

Liu Y. and Comodi P. (1993) Some aspects of the crystal-chemistry of apatites. Mineral. Mag. 57, 709–719.

Lyons J. I. (1988) Volcanogenic iron oxide deposits, Cerro de Mercado and vicinity, Durango. Econ. Geol. 83, 1886–1906.Mandeville C. W. (2010) Sulfur: A Ubiquitous and Useful Tracer in Earth and Planetary Sciences. Elements 6, 75–80.

Manning C. E. (2011) Sulfur Surprises in Deep Geological Fluids. Science (80-). 331, 1018–1019.

Mao M., Rukhlov A. S., Rowins S. M., Spence J. and Coogan L. A. (2016) Apatite Trace Element Compositions: A Robust New Tool for Mineral Exploration. Econ. Geol. 111, 1187–1222.

Matjuschkin V., Blundy J. D. and Brooker R. A. (2016) The effect of pressure on sulphur speciation in mid- to deep-crustal arc magmas and implications for the formation of porphyry copper deposits. Contrib. to Mineral. Petrol, 171, 1-25.

Metrich N. and Mandeville C. W. (2010) Sulfur in Magmas. Elements, 6, 81–86.

Morgan G. and London D. (2005) Effect of current density on the electron microprobe analysis of alkali aluminosilicate glasses. Am. Mineral. 90, 1131–1138.

Neill H. S. C. O., Berry A. J. and Mallmann G. (2018) The oxidation state of iron in Mid-Ocean Ridge Basaltic (MORB) glasses : Implications for their petrogenesis and oxygen fugacities. Earth Planet. Sci. Lett. 504, 152–162.

Parat F., Holtz F. and Streck M. J. (2011) Sulfur-bearing Magmatic Accessory Minerals. Rev. Mineral. Geochemistry 73, 285–314.

Parat F. and Holtz F. (2005) Sulfur partition coefficient between apatite and rhyolite: The role of bulk S content. Contrib. to Mineral. Petrol. 150, 643–651.

Parat F., Holtz F. and Klügel A. (2011) S-rich apatite-hosted glass inclusions in xenoliths from La Palma: constraints on the volatile partitioning in evolved alkaline magmas. Contrib. to Mineral. Petrol. 162, 463–478.

Parat F. and Holtz F. (2004) Sulfur partitioning between apatite and melt and effect of sulfur on apatite solubility at oxidizing conditions. Contrib. to Mineral. Petrol. 147, 201–212.

Peng G., Luhr J. J. F. and Mcgee J. J. J. (1997) Factors controlling sulfur concentrations in volcanic apatite. Am. Mineral. 82, 1210–1224.

Pokrovski G. S. and Dubrovinsky L. S. (2011) The S3- Ion Is Stable in Geological Fluids at Elevated Temperatures and Pressures. Science (80-). 331, 1052–1054.

Pokrovski G. S. and Dubessy J. (2015) Stability and abundance of the trisulfur radical ion S3- in hydrothermal fluids. Earth Planet. Sci. Lett. 411, 298–309.

Ravel B. and Newville M. (2005) ATHENA, ARTEMIS, HEPHAESTUS: Data analysis for X-ray absorption spectroscopy using IFEFFIT. J. Synchrotron Radiat. 12, 537–541.

Righter K., Sutton S. R., Danielson L., Pando K. and Newville M. (2016) Redox variations in the inner solar system with new constraints from vanadium XANES in spinels. Am. Mineral. 101, 1928–1942.

Rouse R. C. and Dunn P. J. (1982) A contribution to the crystal chemistry of ellestadite and the silicate sulfate apatites. Am. Mineral. 67, 90–96.

Scaillet B., Pichavant M. and Roux J. (1995) Experimental crystallization of leucogranite magmas. J. Petrol. 36, 663–705.

Simon A. C. and Ripley E. M. (2011) The Role of Magmatic Sulfur in the Formation of Ore Deposits. Rev. Mineral. Geochemistry 73, 513–578.

Streck M. J. and Dilles J. H. (1998) Sulfur evolution of oxidized arc magmas as recorded in apatite from a porphyry copper batholith. Geology 26, 523–526.

Tepper J. and Kuehner S. (1999) Complex zoning in apatite from the Idaho batholith: A record of magma mixing and intracrystalline trace element diffusion. Am. Mineral. 84, 581–595.

Villiger S., Müntener O. and Ulmer P. (2007) Crystallization pressures of mid-ocean ridge basalts derived from major element variations of glasses from equilibrium and fractional crystallization experiments. J. Geophys. Res. Solid Earth 112, 1–18.

Webster J. D. and Piccoli P. M. (2015) Magmatic Apatite: A Powerful, Yet Deceptive, Mineral. Elements 11, 177–182. Wilke M., Jugo P. J., Klimm K., Susini J., Botcharnikov R., Kohn S. C. and Janousch M. (2008) The origin of S^{4+} detected in silicate glasses by XANES. Am. Mineral. 93, 235–240.

Wilke, M., Partzsch, G.M., Bernhardt, R., and Lattard, D. (2004) Determination of the iron oxidation state in basaltic glasses using XANES at the K-edge: Chemical Geology, 213, 71–87.

Wilke, M., Jugo, P.J., Klimm, K., Susini, J., Botcharnikov, R., Kohn, S.C., and Janousch, M. (2008) The origin of S^{4+} detected in silicate glasses by XANES: American Mineralogist, 93, 235–240.

Wojdyr M. (2010) Fityk: A general-purpose peak-fitting program. J. Appl. Crystallogr. 43, 1126–1128.

Zolotov M. and Fegley B. (1998) Volcanic Origin of Disulfur Monoxide (S2 O) on Io. Icarus, 293–297.

CHAPTER 5: CONCLUSIONS

Apatite is a ubiquitous mineral in terrestrial and extraterrestrial systems and serves as a useful geochemical tool owing to the ability of the apatite structure to incorporate halogens, water, redox sensitive elements, radionuclides, and rare earth elements (Webster and Piccoli, 2015; Hughes and Rakovan, 2015; McCubbin and Jones, 2015). This dissertation evaluates the ability of apatite to record the abundance and oxidation state(s) of S in magmatic systems and provides novel insight into the behavior of S in magmatic systems.

Chapter 2 combined experimental techniques with spectroscopic analyses to understand the incorporation of different oxidation states of S over a broad range of fO_2 (FMQ to FMQ+3), which covers the transition from a S^{2-} to a S^{6+}-dominated silicate melt. The incorporation of three oxidation states of S (e.g., S^{6+}, S^{4+}, and S^{2-}) in apatite likely explains the non-Henrian $D_S^{ap/m}$ behavior that has been observed in the literature (c.f. Parat et al., 2011). Hence, the results presented in chapter II indicate that spectroscopic studies of igneous apatite have the potential to trace S signatures during the evolution of magmatic systems. Upon calibration, the S signatures of apatite can be used to estimate the fO_2, and potentially, the fS_2 of magmatic systems.

Chapter 3 evaluates the published measurements of S in lunar apatite, which crystallized from late-stage felsic (rhyolitic) melts and contain elevated concentrations of S (up to ~430 μg/g S in apatite rims), despite forming from a reduced, anhydrous, and (interstitial rhyolitic) melt containing <<100 μg/g S (Boyce et al., 2014). Due to the

dearth of experimental data that constrains partitioning behavior of S for lunar systems, I performed apatite crystallization experiments equilibrated at conditions relevant to late-stage lunar magmatism. The data indicate that S behaves incompatibly (e.g., $D_S^{ap/m}$ <<1) with respect to apatite that crystallizes in low fO_2 conditions (e.g., ≤FMQ), suggesting that fractional crystallization processes alone cannot reconcile the elevated S contents in lunar apatite. Thus, we proposed testable two hypotheses: (1) >5 orders of magnitude higher fO_2 conditions, and (2) cryptic metasomatic reactions involving apatite, and S-Cl-bearing, F-poor volatile phase(s) perhaps released during degassing of the underlying magma. These results indicate that information regarding the oxidation state of the late stage lunar melt, coupled with incorporation mechanisms of S into apatite, are crucial to fully understand and interpret the major and volatile element (e.g., Cl, F, H_2O, S, and potentially C) zonation recorded by lunar apatite.

Chapter 4 experimentally investigated the influence of fO_2 and bulk S contents on the oxidation states of S-in-apatite, and the distribution of S between apatite and melt (i.e., $D_{S,}^{ap/m}$). The data indicate that the partitioning of S between apatite and melt, as well as the proportion of S^{6+} in apatite (represented as centroid energy (eV) and integrated $S^{6+}/\Sigma S$ peak area ratios), increase systematically with increasing fO_2. This outcome is consistent with apatite favoring (coupled-)substitution mechanisms involving oxidized S compared to intermediate and reduced oxidation states, where: S^{6+} >> (S^{4+}, S^{1+}, S^{2-}). This supports the hypothesis that the concentration of S-in-apatite, and the oxidation state(s) of S-in-apatite can be used as a proxy for the redox conditions and S content of the silicate melt at the time of apatite crystallization. The S-in-apatite oxybarometer presented in Chapter IV is applicable to mafic systems where the fO_2 ranges from ~FMQ-0.5 to

~FMQ+1, such as mid ocean ridge basalt (MORB) as well as relatively reduced ocean island basalts (OIB) and back-arc basin basalt (BABB) systems.

The compilation of this dissertation highlights the ability of S-in-apatite to serve as a powerful geochemical proxy for the behavior of S in magmatic (and probably hydrothermal) systems. Future experimental and theoretical studies are required in order to expand the applicability of the oxy- and sulfur-barometer to a broader range of T-P-X-fO_2-fS_2; including but not limited to, magmatic-hydrothermal, hydrothermal, and high T-P systems. Ultimately, this endeavor would be of high interest to the petrology, geochemistry, volcanology, ore geology and broader earth science community, as it will improve our understanding of large and small-scale geochemical processes here on Earth, and on other planetary bodies.

5.1 REFERENCES

Boyce J. W., Tomlinson S. M., McCubbin F. M., Greenwood J. P. and Treiman A. H. (2014) The Lunar Apatite Paradox. Science (80). 344, 400–402.

Hughes J. M. and Rakovan J. F. (2015) Structurally Robust, Chemically Diverse: Apatite and Apatite Supergroup Minerals. Elements 11, 165–170.

McCubbin F. M. and Jones R. H. (2015) Extraterrestrial Apatite: Planetary Geochemistry to Astrobiology. Elements 11, 183–188.

Parat F., Holtz F. and Streck M. J. (2011) Sulfur-bearing Magmatic Accessory Minerals. Rev. Mineral. Geochemistry 73, 285–314.

Webster J. D. and Piccoli P. M. (2015) Magmatic Apatite: A Powerful, Yet Deceptive, Mineral. Elements 11, 177–182.

APPENDICES

APPENDIX A

SUPPLEMENTARY FIGURE AND TABLE FOR CHAPTER 2

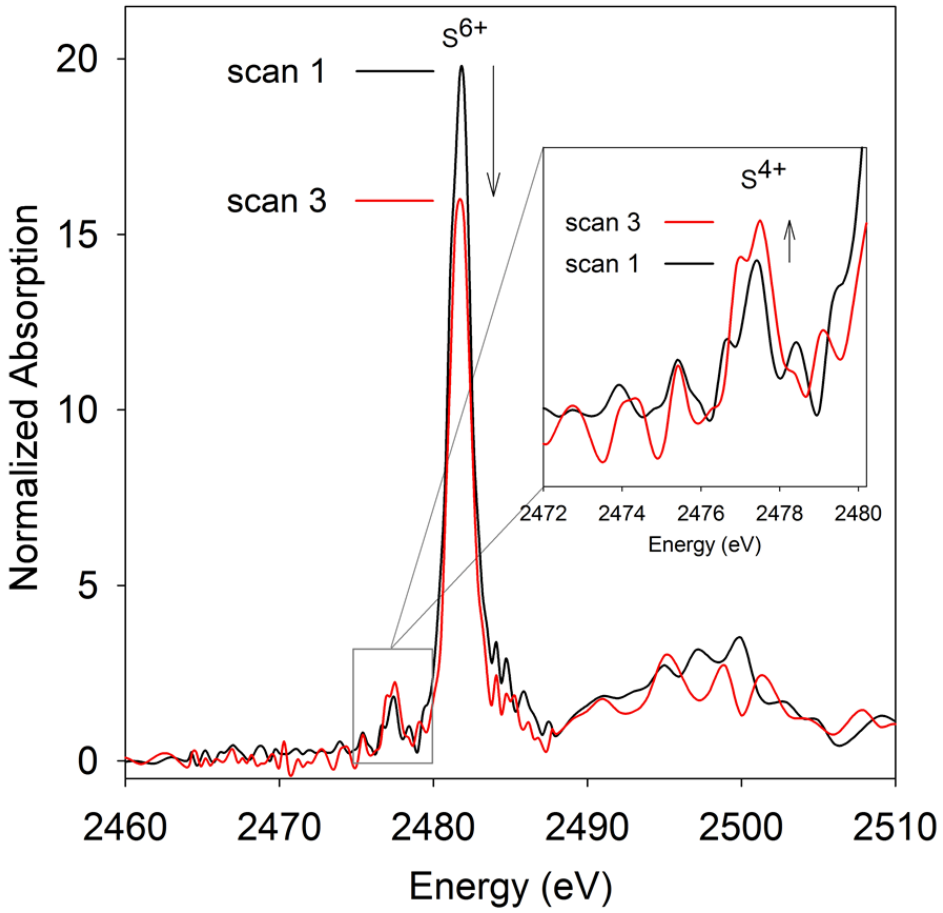

Appendix Figure A1: Sulfur XANES spectra of hydrous lamproitic glass demonstrating beam damage, which is characterized by the systematic reduction of the S^{6+} peak and development of a S^{4+} peak with increasing analytical time (e.g., from scan 1 to scan 3).

Appendix Table A1: EPMA results of Mina Carmen transect.

	Distance (µm) from cavity rim*										
wt.%	**40**	**35**	**30**	**25**	**20**	**15**	**10**	**5**	**0**	**Average**	**l.o.d**
SiO_2	b.d.	b.d.	b.d.	b.d.	b.d.	b.d.	0.17	0.14	0.12	0.05 ±0.02	0.05
TiO_2	b.d.	b.d.	b.d.	b.d.	b.d.	b.d.	b.d.	b.d.	b.d.	0.00 ±0.00	0.02
Al_2O_3	0.07	b.d.	b.d.	b.d.	b.d.	b.d.	b.d.	b.d.	0.17	0.03 ±0.02	0.04
FeO	b.d.	b.d.	b.d.	b.d.	b.d.	b.d.	b.d.	b.d.	b.d.	b.d.	0.07
MgO	b.d.	b.d.	b.d.	b.d.	b.d.	b.d.	b.d.	b.d.	b.d.	b.d.	0.03
MnO	b.d.	b.d.	b.d.	b.d.	b.d.	b.d.	b.d.	b.d.	b.d.	b.d.	0.07
CaO	54.71	55.19	55.08	54.87	54.97	54.89	54.34	54.21	53.55	54.65 ±0.17	0.08
K_2O	b.d.	b.d.	b.d.	b.d.	b.d.	b.d.	b.d.	b.d.	0.09	0.01 ±0.01	0.05
Na_2O	b.d.	b.d.	b.d.	b.d.	b.d.	b.d.	0.11	0.19	0.21	0.06 ±0.03	0.04
P_2O_5	41.84	42.17	41.63	42.17	41.89	42.10	41.17	40.44	40.41	41.54 ±0.23	0.19
Ce_2O_3	b.d.	b.d.	b.d.	b.d.	b.d.	b.d.	b.d.	b.d.	b.d.	b.d.	0.10
La_2O_3	b.d.	b.d.	b.d.	b.d.	b.d.	b.d.	b.d.	b.d.	b.d.	b.d.	0.12
F	3.57	3.92	3.80	3.71	3.70	3.72	3.92	1.62	2.18	3.35 ±0.28	0.51
Cl	0.27	0.23	0.37	0.25	0.20	0.29	0.49	2.60	2.33	0.78 ±0.32	0.02
SO_3	b.d.	b.d.	b.d.	b.d.	b.d.	0.09	0.26	0.52	0.44	0.15 ±0.07	0.01
SrO	0.01	b.d.	b.d.	b.d.	0.01	b.d.	0.02	b.d.	b.d.	b.d.	0.14
BaO	b.d.	0.01	b.d.	b.d.	0.08	0.03	b.d.	b.d.	b.d.	0.01 ±0.01	0.13
O=F, Cl	1.56	1.70	1.68	1.62	1.60	1.63	1.76	1.27	1.44	1.59 ±0.05	-
Total	98.92	99.81	99.19	99.39	99.25	99.47	98.67	98.36	97.97	99.00 ±0.19	-
S (µg/g)	b.d.	b.d.	b.d.	b.d.	b.d.	347.33	1057.01	2095.50	1763.68	585 ±280	-

Notes: b.d. is below detection limit

*EPMA and XANES transect started aproximately ±10-15 um from rim

Analyses given in 1σ standard error of mean

L.O.D is limit of detection

Appendix Table A2: EPMA results of Durango apatite transect.

		wt.%																	
	(µm)	SiO_2	Al_2O_3	FeO	MgO	MnO	CaO	K_2O	Na_2O	P_2O_5	Ce_2O_3	La_2O_3	F	Cl	SO_3	SrO	O=F, Cl	Total	S (µg/g)
Durango Transect Distance (µm) // c-axis	0	0.34	b.d.	b.d.	b.d.	b.d.	55.15	b.d.	0.20	40.41	0.49	0.29	3.57	0.36	0.22	b.d.	1.59	99.45	872
	100	0.44	b.d.	b.d.	b.d.	b.d.	54.29	b.d.	0.18	40.30	0.51	0.30	3.52	0.40	0.21	0.07	1.57	98.66	859
	200	0.44	b.d.	b.d.	b.d.	b.d.	54.94	b.d.	0.19	41.79	0.53	0.30	3.44	0.41	0.22	b.d.	1.54	100.73	884
	300	0.46	b.d.	b.d.	b.d.	b.d.	54.88	b.d.	0.21	40.64	0.46	0.35	3.53	0.40	0.23	b.d.	1.58	99.59	909
	400	0.47	b.d.	b.d.	b.d.	b.d.	54.97	b.d.	0.23	41.00	0.66	0.44	3.69	0.40	0.21	0.02	1.64	100.45	858
	500	0.42	b.d.	b.d.	b.d.	b.d.	55.27	b.d.	0.20	40.67	0.52	0.39	3.34	0.35	0.27	0.01	1.48	99.96	1090
	600	0.40	b.d.	b.d.	b.d.	b.d.	54.13	b.d.	0.22	40.97	0.59	0.42	3.40	0.33	0.23	0.04	1.51	99.22	940
	700	0.40	b.d.	b.d.	b.d.	b.d.	55.10	b.d.	0.20	40.58	0.58	0.36	3.54	0.34	0.20	b.d.	1.57	99.74	781
	800	0.46	b.d.	b.d.	b.d.	b.d.	54.66	b.d.	0.16	41.00	0.71	0.45	3.84	0.36	0.21	0.05	1.70	100.21	846
	900	0.41	b.d.	b.d.	b.d.	b.d.	54.57	b.d.	0.20	40.75	0.76	0.34	3.61	0.38	0.21	0.01	1.61	99.63	847
	1000	0.39	b.d.	b.d.	b.d.	b.d.	54.65	b.d.	0.22	41.09	0.63	0.46	3.45	0.35	0.18	0.04	1.53	99.94	733
	1100	0.40	b.d.	b.d.	b.d.	b.d.	55.36	b.d.	0.21	41.20	0.58	0.42	3.83	0.35	0.20	b.d.	1.69	100.86	787
	1200	0.47	b.d.	b.d.	b.d.	b.d.	54.75	b.d.	0.21	41.29	0.64	0.44	3.71	0.34	0.19	b.d.	1.64	100.41	742
	1300	0.46	b.d.	b.d.	b.d.	b.d.	54.80	b.d.	0.18	40.65	0.72	0.49	3.68	0.34	0.21	b.d.	1.62	99.90	859
	1400	0.42	b.d.	b.d.	b.d.	b.d.	54.98	b.d.	0.23	40.90	0.63	0.48	3.27	0.35	0.20	0.05	1.45	100.05	808
	1500	0.47	b.d.	b.d.	b.d.	b.d.	55.17	b.d.	0.21	40.56	0.71	0.46	3.64	0.34	0.20	0.06	1.61	100.21	820
	1600	0.45	b.d.	b.d.	b.d.	b.d.	54.93	b.d.	0.19	41.54	0.72	0.47	3.44	0.35	0.22	0.07	1.53	100.83	872
	1700	0.44	b.d.	b.d.	b.d.	b.d.	54.83	b.d.	0.20	40.54	0.73	0.48	3.26	0.35	0.19	0.06	1.45	99.63	753
	1800	0.40	b.d.	b.d.	b.d.	b.d.	54.68	b.d.	0.21	40.68	0.71	0.43	3.81	0.39	0.20	0.06	1.69	99.88	817
	1900	0.45	b.d.	b.d.	b.d.	b.d.	54.59	b.d.	0.20	41.00	0.64	0.43	3.54	0.38	0.22	b.d.	1.57	99.86	861
	2000	0.44	b.d.	b.d.	b.d.	b.d.	55.13	b.d.	0.17	40.59	0.72	0.45	3.46	0.35	0.21	b.d.	1.53	99.98	847
	2100	0.46	b.d.	b.d.	b.d.	b.d.	55.42	b.d.	0.23	40.80	0.74	0.39	3.65	0.36	0.26	b.d.	1.62	100.70	1031
	2200	0.47	b.d.	b.d.	b.d.	b.d.	55.06	b.d.	0.23	41.07	0.58	0.40	3.20	0.34	0.22	b.d.	1.42	100.15	893
	2300	0.43	b.d.	b.d.	b.d.	b.d.	55.05	b.d.	0.21	40.57	0.57	0.41	3.64	0.35	0.19	0.10	1.61	99.91	748
	2400	0.46	b.d.	b.d.	b.d.	b.d.	54.75	b.d.	0.22	40.42	0.65	0.48	3.62	0.38	0.23	b.d.	1.61	99.60	913
	2500	0.45	b.d.	b.d.	b.d.	b.d.	54.86	b.d.	0.25	41.05	0.68	0.56	3.36	0.36	0.24	0.10	1.50	100.42	943
	2600	0.41	b.d.	b.d.	b.d.	b.d.	53.13	b.d.	0.27	39.09	0.51	0.41	3.30	0.35	0.29	0.07	1.47	96.35	1151
	2700	0.41	b.d.	b.d.	b.d.	b.d.	55.16	b.d.	0.24	41.61	0.59	0.51	3.56	0.33	0.23	0.04	1.57	101.11	934
	2800	0.42	b.d.	b.d.	b.d.	b.d.	55.05	b.d.	0.25	40.93	0.71	0.52	3.33	0.36	0.23	b.d.	1.48	100.32	915
	2900	0.44	b.d.	b.d.	b.d.	b.d.	54.90	b.d.	0.22	41.12	0.65	0.40	3.59	0.36	0.24	0.01	1.59	100.34	947
	3000	0.44	b.d.	b.d.	b.d.	b.d.	55.34	b.d.	0.22	41.03	0.65	0.46	3.55	0.35	0.21	0.04	1.57	100.73	858
	Average	**0.43**	**b.d.**	**b.d.**	**b.d.**	**b.d.**	**54.86**	**b.d.**	**0.21**	**40.83**	**0.63**	**0.43**	**3.53**	**0.36**	**0.22**	**0.05**	**1.57**	**99.98**	**875**
	l.o.d	0.05	0.04	0.07	0.03	0.07	0.08	0.05	0.04	0.19	0.10	0.12	0.51	0.02	0.01	0.14	-	-	-

Notes: l.o.d is limit of detection in elemental wt.%

Appendix Table A3: EPMA results of Durango apatite reference from Young et al. (1969) compared to the Durango apatite reference used in this study.

wt.%	Durango F-Apatite (Young et al., 1969)	Durango F-Apatite Perpendicular c-axis
SiO_2	0.34	0.35 ±0.02
Al_2O_3	0.07	b.d.
FeO	0.01	b.d.
MgO	0.01	b.d.
MnO	0.01	b.d.
CaO	54.02	54.17 ±0.07
K_2O	0.01	b.d.
Na_2O	0.23	0.20 ±0.05
P_2O_5	40.78	41.53 ±0.07
RE_2O_3	1.43	0.92 ±0.02**
F	3.53	3.52 ±0.29
Cl	0.41	0.49 ±0.02
SO_3	0.36	0.34 ±0.01
SrO	0.07	b.d.
O=F, Cl	1.58	1.59
Total	99.94*	99.88 ±0.10
S (µg/g)	1451	1357 ±27

*Reported totals include: ThO_2, As_2O_3, V_2O_3, CO_2, and H_2O

**Only includes Ce_2O_3 and La_2O_3

n=15; this study

APPENDIX B

MODELING PROCEDURE, EXPERIMENTAL METHODS AND EXTENDED DISCUSSION FOR CHAPTER 3

B1 EXPERIMENTAL APPROACH

Gold capsules (3.8 mm O.D., 0.12 mm wall thickness, 10 mm length) were loaded stepwise with ~37 mg of anhydrous rhyolitic or lamproitic glass (Table B2 and B3), ~3 μL H_2O (or ~1.8 μL H_2O for the ΔFMQ-1 experiment), and either: 0.2, 0.4, or 0.8 mg pyrrhotite. The elevated water contents (>4 wt.%) are required to promote crystal growth; however, as mentioned in the main text, the results are applicable to lunar magmas and allow us to evaluate the S signature in apatite from lunar mare basalts. The capsules were weighed, welded shut, and placed in a drying oven (110-120°C) for several hours, then re-weighed to check for water loss. Charges were pressurized to ~100 MPa and rapidly decompressed to confirm the mechanical integrity of the welds and capsule. Apatite crystallization experiments were run at 1,000°C and 300 MPa for 3-5 days at the oxygen fugacity (fO_2) values of ΔFMQ-1, ΔFMQ and ΔFMQ+3, where FMQ is the fayalite-magnetite-quartz oxygen fugacity buffer. The fO_2 was controlled by adding H_2 to the Ar-pressure medium and was monitored by using a Shaw-membrane (Berndt et al., 2002).

I highlight that ΔFMQ-1 is the lowest fO_2 conditions that can feasibly be achieved in the IHPV apparatus used in this study at 300 MPa, 1,000°C, and >4 wt% H_2O. After

rapid quench (Berndt et al., 2002): (a) the capsules were re-weighed to confirm their mechanical integrity at run conditions, and (b) the run products were then carefully recovered from the capsules. Capsules revealing loss of weight (i.e., of volatiles/water) during any of the experimental steps were discarded. Mafic experiments were performed to test the melt compositional effect on S partitioning between apatite and melt, but are of lower importance for this study as discussed below (Appendix 1); note: the mafic sulfide saturated experiment was performed Konecke et al. (2017). The compositions of the (anhydrous) starting glasses are provided in Table B1.

All experiments produced a homogenous glass and un-zoned, coexisting apatite grains >5 um in diameter. The presence of sulfides (or sulfates) within the nominally sulfide (or sulfate) saturated runs was confirmed via energy dispersive spectroscopy (EDS). The lamproite runs are characterized by a high crystallinity with clinopyroxene (cpx), amphibole (amp), and ± iron sulfide (po; e.g., depending on the fO_2 of the system) as mineral phases in addition to apatite; mineral phases identified via EDS. The analytical results of the felsic and mafic apatite crystallization experiments are provided in Table B2 and B3, respectively.

B2 ANALYTICAL APPROACH

The experimental run products (glass and apatite) and natural apatite from the terrestrial Carmen iron oxide – apatite ore deposit, Chile, were characterized quantitatively by wavelength dispersive electron probe microanalysis (EPMA) by using a CAMECA SX-100 at the University of Michigan (UM), American Museum of Natural History (AMNH), and at the Leibniz University Hannover (LUH). An acceleration voltage of 15 keV, a beam current of 10 nA and a beam size of 2 μm was used for all

element analysis of apatite (except for S); a second beam condition (15 keV, 35 nA, ~1-2 μm beam) was used for S to achieve limits of detection of ~30 μg/g S. Counting times for the apatite analyses were: 5 s for F; 20 s for Cl; and 240 s for S. An acceleration voltage of 15 keV, a beam current of 5-10 nA and a beam size of 5-10 μm beam was used for EPMA of the glasses. Counting times for the glass analyses were: 10 s for F; 20 s for Cl; and 240 s for S. Precautions were taken to prevent beam damage of glass (e.g., Cl, Na diffusion and Al, Si burn-in) and apatite (e.g., F migration owing to crystallographic orientation effects; Goldoff et al., 2012) during EPMA. Monitoring of Durango apatite (a fluorapatite) during the EPMA sessions confirmed the suitability of our analytical approach for high-precision apatite analysis (e.g., the F content was reproduced within ~5 % relative to the known content in Durango apatite; cf. Jarosewich et al. 1980). Both SiO_2 and Al_2O_3 concentrations were monitored in experimental apatite to determine possible contribution from the surrounding glass and mineral assemblages.

Fourier transform infrared (FTIR) spectroscopy was performed at the American Museum of Natural History (AMNH) to quantify the water content of experimental rhyolitic glasses (mafic glass pockets were too small to measure with FTIR) using the instrumentation and methods described by Mandeville et al. (2002), and using the molar absorption coefficients of Ohlhorst et al. (2001). The H_2O contents measured via FTIR were within analytical error of the contents estimated from mass balance calculations (see SI Table 2.2).

B3 EXTENDED DISCUSSION

B3.1 Fractional Crystallization of Mafic Melt Scenario

In addition to the scenarios discussed in the main text, an empirically testable hypothesis invokes early crystallization of lunar apatite from a mafic silicate melt. As for the lunar rhyolitic system, we followed Liu et al. (2007) to calculate the theoretical SCSS for mare basalt 12039 (Rhodes et a., 1977) using the following parameters: $T_{Solidus}$= 1,100°C (see main text for discussion; c.f. Taylor et al., 1991 and references therein); H_2O contents ranging from 1-100 μg/g H_2O, fO_2 of ΔIW iron-wüstite = -1 to +4, and 0.1 MPa. The model results coupled with the experimental $D_S^{ap/m}$ values (Table B2) suggest that the low S contents reported for the core of the lunar apatite (<200 μg/g; Greenwood et al., 2011; Boyce et al., 2014) are consistent with crystallization of apatite from a H_2O poor (~10 μg/g H_2O), S rich mafic melt (~1,200 μg/g S). However, this scenario for the apatite core is highly unlikely considering the low P_2O_5 content in the bulk mare basalt (~900 μg/g P_2O_5; Rhodes et al., 1977), where apatite saturation is only achieved once the residual melt in the mare basalt reached a rhyolitic composition (≥88% crystallization; Sha, 2000). Furthermore, crystallization of apatite containing ~430 μg/g S (i.e., rims of lunar apatite) would require an implausible amount of ~3,300 μg/g S in a H_2O poor (~10 μg/g H_2O) mafic melt.

B3.2 Volatile signatures in terrestrial and extraterrestrial apatite

An alternative approach to decipher the lunar apatite volatile signatures is to compare them with the volatile signature systematics of terrestrial apatite. Apatite from iron oxide-apatite (IOA) ore deposits—which occur globally and are produced by magmatic-hydrothermal processes in volcanic systems (Knipping et al., 2015)—fingerprint textural and chemical reactions related to metasomatism (Treloar and Colley, 1996; Harlov, 2015; Figures B1 and B2). Similar F-Cl-(H)-S trends (Figure B1) and

textural observations (e.g., volatile pathways; Nadeau et al., 2010) observed for lunar apatite and terrestrial Mina Carmen apatite perhaps reflect similar mechanisms; e.g., a metasomatic (i.e., modal and/or cryptic) reaction of fluorapatite to fluor-chlorapatite via replacement of F by Cl in the apatite structure (Figure B2). We stress that despite the difference in the core-to-rim length scales of volatile concentrations in terrestrial Mina Carmen apatite and lunar apatite, the similarities with respect to the overall trends, and not the absolute concentrations, can be used to infer that similar processes affected the apatite in both systems (e.g., length scales can differ depending on T-X of the volatile phase and duration of exposure).

Secondary REE-phosphate (e.g., monazite; $[Ce,LREE,Th]PO_4$) inclusions in apatite from the Mina Carmen IOA deposit (Treloar and Colley, 1996) in the Chilean iron belt evince chemical alteration via metasomatism (Harlov et al., 2015; this study). Volatile trends for F and Cl from the Mina Carmen and lunar apatite (Appendix Figure B1) record the reaction of fluorapatite to fluor-chlorapatite via replacement of F by Cl in the apatite structure. Fluorapatite to chlorapatite metasomatic alteration (e.g., where ap-X_{Cl} > ap-X_F) via $CaCl_2$-rich brines has been observed in nepheline-bearing clinopyroxenites from the Ural Mountains, Russia; Krause et al., 2013). Similarly, extraterrestrial basalts (e.g., lunar basalts) that show evidence of metasomatism tend to contain relatively more Cl enriched apatite than non-metasomatized basalts (Hovis and Harlov, 2010; McCubbin et al., 2011; McCubbin and Jones, 2015).

High-contrast backscattered electron (BSE) images of 12039,42 apatite grain 9 (Appendix Figure B2) in the study by Greenwood et al. (2011) provide evidence for complex chemical zoning in lunar apatite (e.g., heterogeneous concentrations of volatiles

and rare-earth elements such as Ce). Lunar apatite from the Greenwood et al. (2011) and Boyce et al. (2014) studies show evidence of incompatible element enrichment near the rims and along cracks (fractures) within the apatite grain.

Some results reported by Greenwood et al. (2011) for lunar apatite were interpreted by the authors as being a cross-axial heterogeneity zoning effect and excluded from further considerations (open circles in Figure 1). However, the BSE image of apatite 12039,42 grain 12 from Greenwood et al. (2011) shows that the analytical spots represented by the open circles are adjacent to cracks in the apatite crystal that are bordered by incompatible element enrichment. These analytical spots are consistent with F-Cl-OH-S concentrations measured near the apatite rims, further suggesting that the volatiles signatures were induced by metasomatic alteration, post apatite crystallization.

In terrestrial volcanic systems, Nadeau et al. (2010) reported petrographic evidence for the exsolution of an aqueous phase that could produce sufficient overpressure-induced hydrofracturing and create pathways for fluid mobility upon decompression of an ascending magma. This indicates that the incompatible element enrichment of the lunar apatite rim and proximal to cracks (i.e., fluid pathways) within apatite may have formed after the formation of the apatite core, since the pathways crosscut the preexisting core of the apatite grains (see Figure B2).

Similar fluid pathways are observed in apatite from the terrestrial Carmen deposit, where fluid infiltration and alteration is evidenced by the presence of REE-phosphate inclusions (e.g., monazite; $(Ce,LREE,Th)(PO_4)$; see Figure B2). Formation of nano- and micro-porosity in metasomatically altered regions of apatite enhances fluid permeation, which promotes rapid diffusive mass transfer of cations and anions between the fluid and

the apatite (Harlov et al., 2005; Kusebauch et al., 2015). The presence of REE-phosphate inclusions in Carmen apatite provides further evidence that the porosity (e.g., fluid pathways; see Figure B2) was sufficient enough to allow fluid-induced dissolution and re-precipitation of REE-phosphates. However, hydrothermal fluids containing aqueous Na (e.g., NaCl brines) discourage the dissolution-reprecipitation of REE-phosphate inclusions, since Na is less prone to leave the apatite structure because charge balance is retained (Harlov et al., 2015), and plausibly explains the absence of REE-phosphates adjacent to lunar apatite 12039,42.

The similar trends observed for F, Cl and S (Figure DR1) indicate an incorporation of S on the column anions site of apatite, consistent with Konecke et al. (2017) and also indicating similar processes. Finally, although probably less likely, the volatile signatures in both Carmen and lunar apatite could also be explained by dissolution and reprecipitation reactions of the apatite in the presence of a metasomatic fluid (e.g., Engvik et al., 2009).

B3.3 Absence of glass alteration

EPMA of the evolved glass believed to be in equilibrium with lunar apatite 12039,42 (Greenwood et al., 2011; Boyce et al., 2014) revealed exceedingly low S-content (e.g., below a reasonable limit of detection of <100 μg/g S for the reported EPMA conditions). Thus, as discussed above and in the main text, we argue that the volatile signature in lunar apatite is related to metasomatism in the presence of a free volatile phase. Our observations and interpretations beg the question as to why the apatite exhibits evidence of hydrothermal alteration, whereas the evolved and late-stage glass does not. A first order explanation is provided by the fact that glass analyses are often

performed near the center of the glass using, e.g., a defocused ion/electron beam (typically 5 to 20 μm; i.e., relatively low spatial resolution) in order to avoid contribution from surrounding mineral assemblages, while minimizing the impact on the sample (e.g., Na migration, see Devine et al., 1995). However, the consequence of this technique is that it cannot yield much chemical information regarding the edge or rim of the glass. In other words, if the element diffusion length scales into the glass are short, the interaction volume of the probe will not detect elevated S-concentrations.

We further suggest that the lack of alteration signatures in the residual glass of 12039 lunar mare basalt is directly related to the high fluid-melt partition coefficients for S (especially in reduced systems; Zajacz et al., 2012), as well as due to a kinetically sluggish uptake of S by the evolved felsic lunar glass when compared to the apatite. In relatively more oxidizing systems (unrealistic for lunar magmas), where anhydrite ($CaSO_4$) is the predominant S-bearing phase, tephra can sequester S (e.g., specifically SO_2) at T > 600°C (Aryis et al., 2013). The scavenging ability of tephra is controlled by the rate at which Ca^{2+} diffuses towards the glass interface, where it forms Ca-S complexes (Aryis et al., 2013). However, at the low fO_2 of lunar systems (i.e., ~ΔFMQ-4), S^{2-} is the only relevant oxidation state of S in the melt and it most likely forms complexes with Fe^{2+} in the melt structure (Zajacz et al., 2012; Fiege et al., 2015). Thus, the uptake of S into the quenched residual felsic melt from a hydrothermal fluid is presumably controlled by Fe diffusion. In turn, the low Fe contents in the residual lunar melt (<0.3 wt.% FeO) will further limit the potential uptake of S explaining the sluggish (not detected) uptake of S by the residual felsic glass in the mare basalts when compared to apatite.

Alternatively, as briefly discussed in the main text, the lunar apatite signatures could reflect high water concentrations in a residual felsic melt of the lunar mare basalts (>>10,000 μg/g H_2O), where the residual melt degassed after apatite formation and solidifies soon after; i.e. the apatite has no time to re-equilibrate. Although there is some recent evidence for elevated water contents in some lunar rhyolites (Mills et al., 2017), the absence of vesicles in the lunar mare basalt contradicts this scenario.

B3.3 Stable Isotope Systematics

Previous studies have used stable isotope systematics to investigate degassing of lunar magmas (cf. McCubbin et al., 2015B, and references therein). Recently, it has been demonstrated that the applicability of Cl isotopes to the "water-on-moon-debate" remains controversial (Ustunisik et al., 2015). Boyce et al. (2015) propose early degassing of the Moon's magma ocean; such degassing may "alter" the signature in lunar apatite (in particular those samples closer to the surface that were collected during the Apollo missions), consistent with the cryptic metasomatism hypothesis proposed in this study for apatite in lunar mare basalt (see main text).

B3.4 Brief petrographic description of Mina Carmen

The Mina Carmen iron oxide apatite (IOA) deposit is located ~20 km E of the Atacama fault system in northern Chile (26.346993°S; 70.143110°W). The deposit is hosted within porphyritic andesite of the Los Cerros Florida formation and is dominated by massive iron oxide ore bodies consisting of magnetite and patches of modally minor hematite and minor apatite (Treloar and Colley, 1996). Apatite occurs as coarse-grained crystals up to 50 cm in length within the magnetite matrix and also within planar zones of

magnetite. Halogen (F, Cl) and volatile (S) element zonation observed in Carmen apatite (Treloar and Colley, 1996; Konecke et al., 2017) is interpreted to represent primary magmatic fluorapatite that was subsequently metasomatically overprinted to chlorapatite ($ap\text{-}X_{Cl} > ap\text{-}X_F$) by an aqueous Cl-S-rich, F-poor phase.

B3.5 Apollo 12 low Ti-mare basalt 12039

Lunar sample 12039 is characterized as pigeonite basalt containing mm-sized pyroxene, plagioclase and tridymite (Rhodes et al., 1977; Baldridge et al., 1979; Neal et al., 1994). Apatite found within the mesostasis and is interpreted to have been associated with late-stage crystallization features such as high K, Si glass, pyroxferroite and Ba-rich feldspar (Greenwood et al., 2011). Sample 12039,42 contains minor apatite that is relatively enriched in S (e.g., up to 430 μg/g S) and OH (up to ~1.1 wt% H_2O; Greenwood et al., 2011; Boyce et al., 2014).

Appendix Table B1: Starting glass compositions

wt.%	SiO_2	TiO_2	Al_2O_3	FeO	MnO	MgO	CaO	Na_2O	K_2O	P_2O_5	H_2O	F	Total
Felsic (*AP1008)	72.83	0.05	13.68	1.12	0.01	0.17	2.21	3.30	4.55	1.47	n.d.	0.14	99.53
Mafic (**LA45)	40.13	4.37	8.57	8.75	0.20	9.21	16.24	0.50	5.29	3.81	n.d.	n.d.	97.07

Notes: *AP1008: Granite from the Krŭsné Hory Mts. (Europe) + 3 Wt.% P_2O_5; fused at 1,500°C for 3 hours
**LA45: Lamproite (sample AL/KB6-98) from Luttinen et al. (2002); Loss of ignition at 1,200°C = 8.40%.
Felsic glass analyzed by EPMA at UM; mafic glass by XRF at LUH; n.d. not detected

Appendix Table B2: EMPA of experimental AP1008-IH apatite & glass

AP1008	IH1	IH1	IH2	IH2	IH24	IH24	IH17	IH17
	Ap	Glass	Ap	Glass	Ap	Glass	Ap	Glass
wt.%	Sulfide-saturated		Sulfide-undersaturated		Sulfide-saturated		Sulfate-saturated	
SiO_2	1.03 ±0.20	68.58 ±0.13	0.75 ±0.15	68.43 ±0.16	0.88 ±0.17	71.44 ±0.20	0.40 ±0.08	69.15 ±0.31
Al_2O_3	0.21 ±0.05	12.74 ±0.03	0.15 ±0.03	12.68 ±0.05	0.14 ±0.04	13.69 ±0.20	0.05 ±0.03	13.36 ±0.06
FeO	0.69 ±0.01	1.17 ±0.02	0.67 ±0.03	1.31 ±0.03	0.74 ±0.02	1.18 ±0.03	0.48 ±0.01	1.75 ±0.03
MgO	0.19 ±0.01	0.16 ±0.00	0.18 ±0.01	0.16 ±0.00	0.21 ±0.01	0.17 ±0.01	0.19 ±0.01	0.17 ±0.01
MnO	0.15 ±0.01	b.d.	0.16 ±0.01	b.d.	0.17 ±0.01	0.05 ±0.01	0.16 ±0.01	0.05 ±0.01
CaO	52.16 ±0.30	1.83 ±0.08	52.71 ±0.28	1.81 ±0.13	53.02 ±0.28	1.26 ±0.02	53.21 ±0.10	1.39 ±0.01
K_2O	0.21 ±0.01	4.18 ±0.02	0.20 ±0.02	4.17 ±0.02	0.18 ±0.01	3.97 ±0.03	0.14 ±0.01	3.51 ±0.18
Na_2O	0.18 ±0.02	2.86 ±0.01	0.17 ±0.03	2.64 ±0.03	0.15 ±0.01	2.78 ±0.05	0.18 ±0.01	1.82 ±0.15
P_2O_5	41.40 ±0.12	1.16 ±0.06	41.28 ±0.25	1.21 ±0.10	41.10 ±0.18	0.76 ±0.02	41.60 ±0.19	0.91 ±0.02
Ce_2O_3	0.43 ±0.02	b.d.	0.43 ±0.01	b.d.	0.37 ±0.03	b.d.	0.32 ±0.01	b.d.
La_2O_3	0.27 ±0.01	b.d.	0.21 ±0.02	b.d.	0.27 ±0.03	b.d.	0.19 ±0.01	b.d.
Cl	0.12 ±0.00	b.d.	0.10 ±0.00	b.d.	0.01 ±0.01	b.d.	0.01 ±0.01	b.d.
F	2.16 ±0.03	b.d.	2.15 ±0.11	b.d.	1.82 ±0.01	b.d.	2.00 ±0.06	b.d.
SO_3	0.02 ±0.00	0.05 ±0.00	0.01 ±0.00	0.05 ±0.00	0.02 ±0.00	0.05 ±0.00	0.14 ±0.01	0.10 ±0.00
O=F, Cl	0.94	-	0.93	-	0.77	-	0.84	-
OH wt.%	1.36*	-	1.37*	-	1.71*	-	1.54*	-
Mass Balance H_2O	-	7.29 ±0.11	-	7.56 ±0.10	-	4.55 ±0.23	-	7.38 ±0.17
FTIR	-	7.69 ±0.31	-	7.59 ±0.31	-	n.a.	-	n.a.
Total	99.64 ±0.34	92.73 ±0.11	99.61 ±0.35	92.46 ±0.10	100.05 ±0.32	92.46 ±0.10	99.75 ±0.09	92.49 ±0.17
S (µg/g)	88 ±8	193 ±8	33 ±5	176 ±9	84 ±21	220 ±6	571 ±46	405 ±5
# of analyses	6	15	5	18	6	10	5	19
T°C	1000		1000		1000		1000	
P (MPa)	300		300		300		300	
ΔFMQ	0		0		-1		3	
Pyrrhotite (wt.%)	1.00		0.50		2.00		1.00**	
Run Duration (hrs)	72		72		111		150	
$Ds^{ap/m}$	**0.46 ±0.04**		**0.18 ±0.03**		**0.38 ±0.09**		**1.41 ±0.11**	

Notes: b.d. is below detection limit; n.a. is not analyzed

O=F, Cl is correction factor

*Calculated using Ketcham (2015)

**~0.35 wt.% S (elemental) + ~0.92 wt.% Fe_2O_3, where the Fe/S ratio corresponds to po.

Analyses given in 1σ standard error of mean

$Ds^{ap/m}$ error given in 1σ standard error of mean

Appendix Table B3: EMPA of experimental LA45-IH apatites & glass

wt.%	LA45-IH1 Ap	LA45-IH1 Glass	LA45-IH3 Ap	LA45-IH3 Glass
	Sulfide-saturated		Sulfide-undersaturated	
SiO_2	1.73 ±0.22	43.50 ±0.22	1.15 ±0.09	44.44 ±0.36
TiO_2	0.04 ±0.01	2.64 ±0.05	0.04 ±0.01	2.71 ±0.03
Al_2O_3	0.47 ±0.28	12.71±0.17	0.10 ±0.02	12.91 ±0.15
FeO	0.59 ±0.06	9.30 ±0.17	0.46 ±0.02	9.37 ±0.13
MgO	0.25 ±0.11	1.68 ±0.10	0.24 ±0.06	1.78 ±0.03
MnO	b.d.	0.30 ±0.02	b.d.	0.35 ±0.02
CaO	53.00 ±0.32	9.00 ±0.23	53.52 ±0.12	8.74 ±0.15
K_2O	0.29 ±0.03	8.93 ±0.04	0.26 ±0.02	8.39 ±0.46
Na_2O	0.01 ±0.01	1.58 ±0.04	b.d.	1.42 ± 0.08
P_2O_5	39.30 ±0.17	0.91 ±0.22	40.43 ±0.10	0.66 ±0.19
Ce_2O_3	0.54 ±0.02	b.d.	0.48 ±0.02	b.d.
La_2O_3	0.23 ±0.01	b.d.	0.22 ±0.01	b.d.
F	1.43 ±0.05	0.39 ±0.11	1.56 ±0.04	0.45 ±0.08
Cl	b.d.	0.01 ±0.01	b.d.	b.d.
SO_3	0.08 ±0.01	0.64 ±0.05	0.04 ±0.01	0.32 ±0.01
SrO	0.94 ±0.02	n.a.	1.01 ±0.04	n.a.
BaO	0.02 ±0.01	0.50 ±0.04	0.02 ±0.01	0.52 ±0.04
O=F, Cl	0.60	-	0.65	-
Total	100.31 ±0.26	92.08 ±0.26	100.79 ±0.19	92.05 ±0.51
H_2O (mass balance)	2.05*	7.92	1.95*	7.95
S (µg/g)	322 ±44	2553 ±200	164 ±49	1270 ±47
# of analyses	10	7	9	8
T°C	1000	-	1000	-
P (MPa)	300	-	300	-
ΔFMQ	0	-	0	-
Pyrrhotite (wt.%)	1.00	-	0.50	-
Run Duration (hours)	120.65	-	120.65	-
$D_S^{ap/m}$	**0.13 ±0.03**		**0.13 ±0.08**	

Notes: b.d. is below detection limit; n.a. is not analyzed

O=F, Cl is correction factor

*Calculated using Ketcham (2015)

Analyses given in 1σ standard error of mean

$D_S^{ap/m}$ error given in 2σ standard error of mean

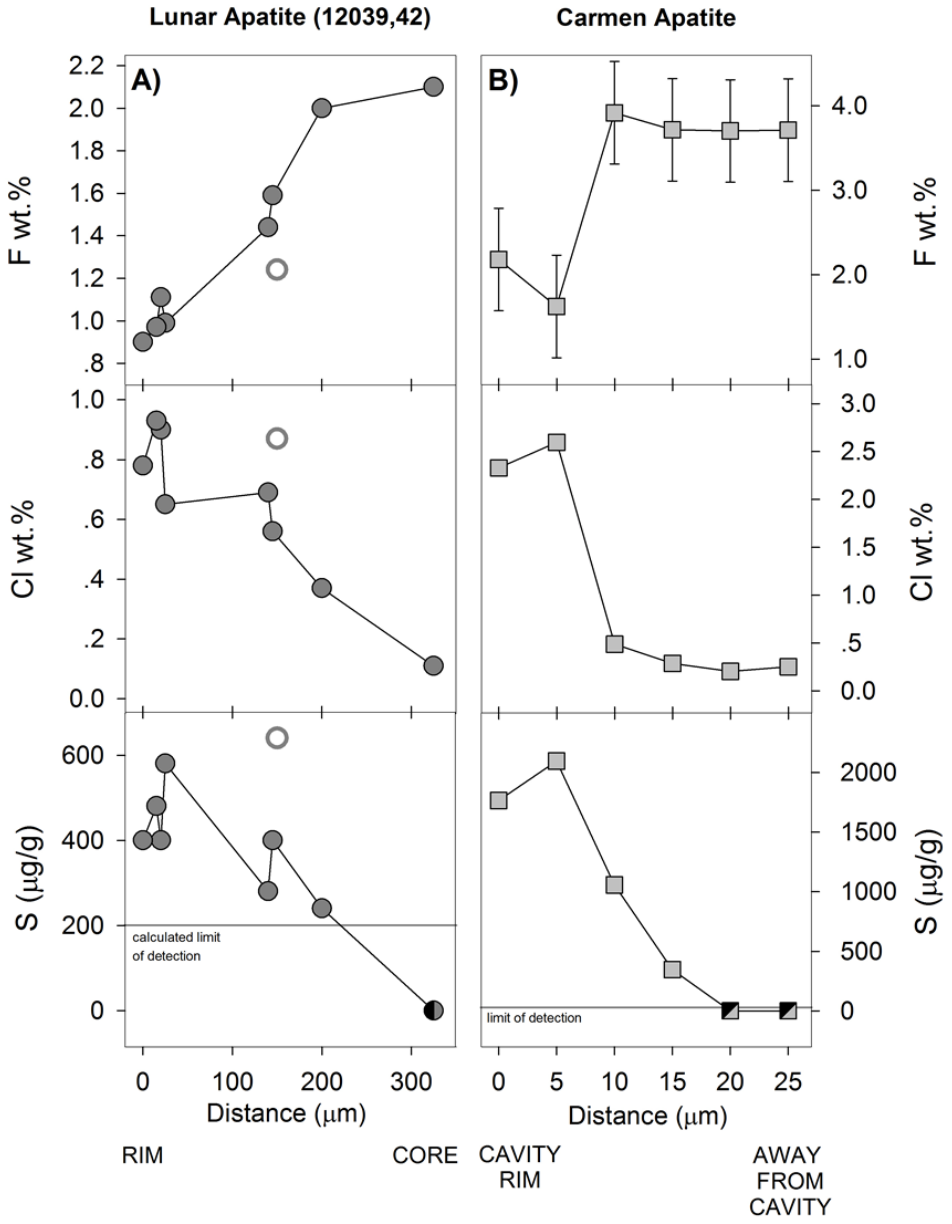

Appendix Figure B1 A-B: Volatile element zonation in lunar (sample 12039,42 grain 12 from Boyce et al., 2014) and terrestrial (Mina Carmen; this study) apatite. Both apatite samples show a systematic increase in S and Cl, and decrease in F, from core to rim (lunar) and proximity to a (formerly) volatile bearing cavities (terrestrial; see Figure 2B). Greenwood et al. (2011) reported S contents of the apatite core as below their (unpublished) limit of detection (l.o.d); we calculated a limit of detection of <200 µg/g S based on their reported analytical conditions (solid gray line). Symbols: Square: Mina Carmen apatite (IOA deposit, Chile); circles: lunar apatite data (Greenwood et al., 2011); semi-filled circle/square below limit of detection for S: ~30 µg/g S (solid gray line; Mina Carmen) and <200 µg/g S (solid gray line); open circles: data excluded by Boyce et al. (2014; see section B3.2). Errors bars: 2σ (some smaller than symbol size).

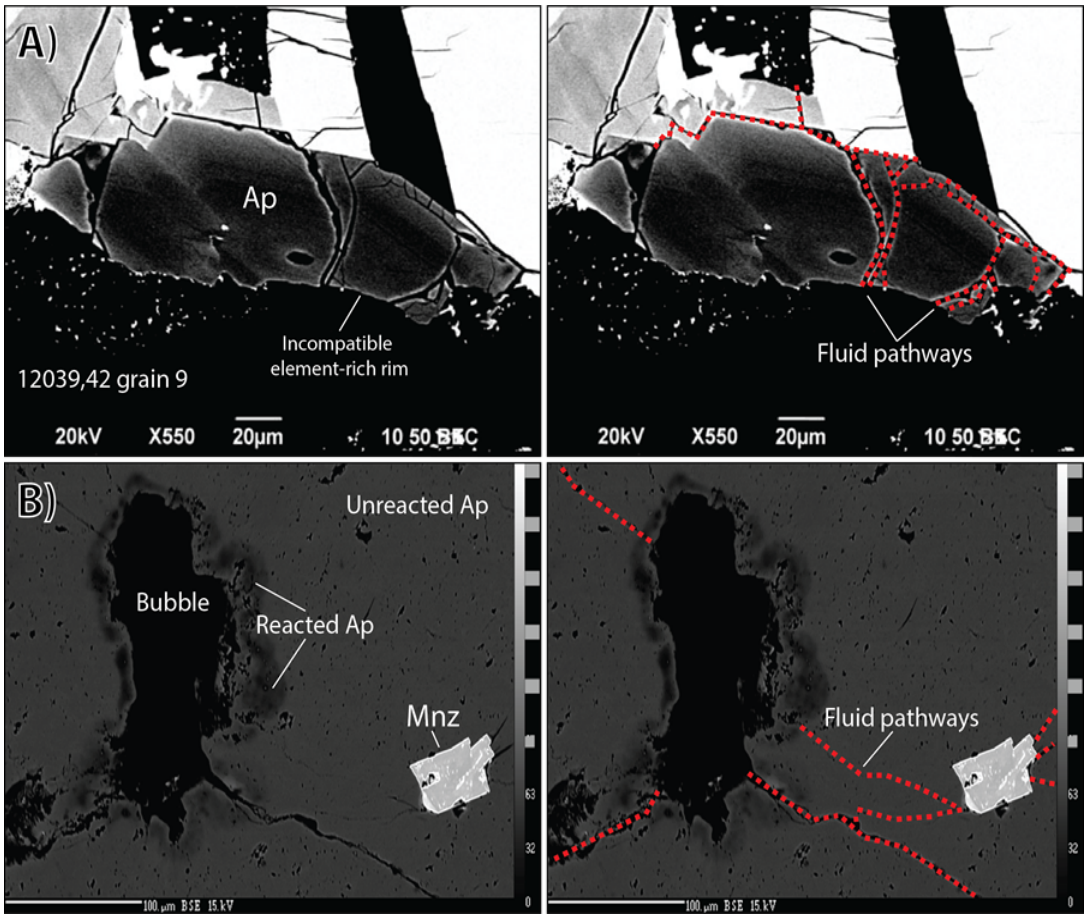

Appendix Figure B2 A-B: Images of terrestrial and lunar apatite. (A) High-contrast backscattered electron (BSE) images of lunar sample 12039,42 apatite grain 9 (note: different apatite grain than in Figure 1; BSE image modified from Greenwood et al., 2011). (B) BSE image of Mina Carmen apatite; scale bar in (B) is 100 µm. The potential volatile pathways (Nadeau et al., 2010; red dotted lines) that crosscut the apatite grain in (A) and radiate from the fluid/vapor cavity in (B) coupled with, incompatible element enriched apatite rims (A) and the presence of monazite (Mnz) inclusions (B; Harlov, 2015) infer volatile-induced metasomatic alteration of apatite.

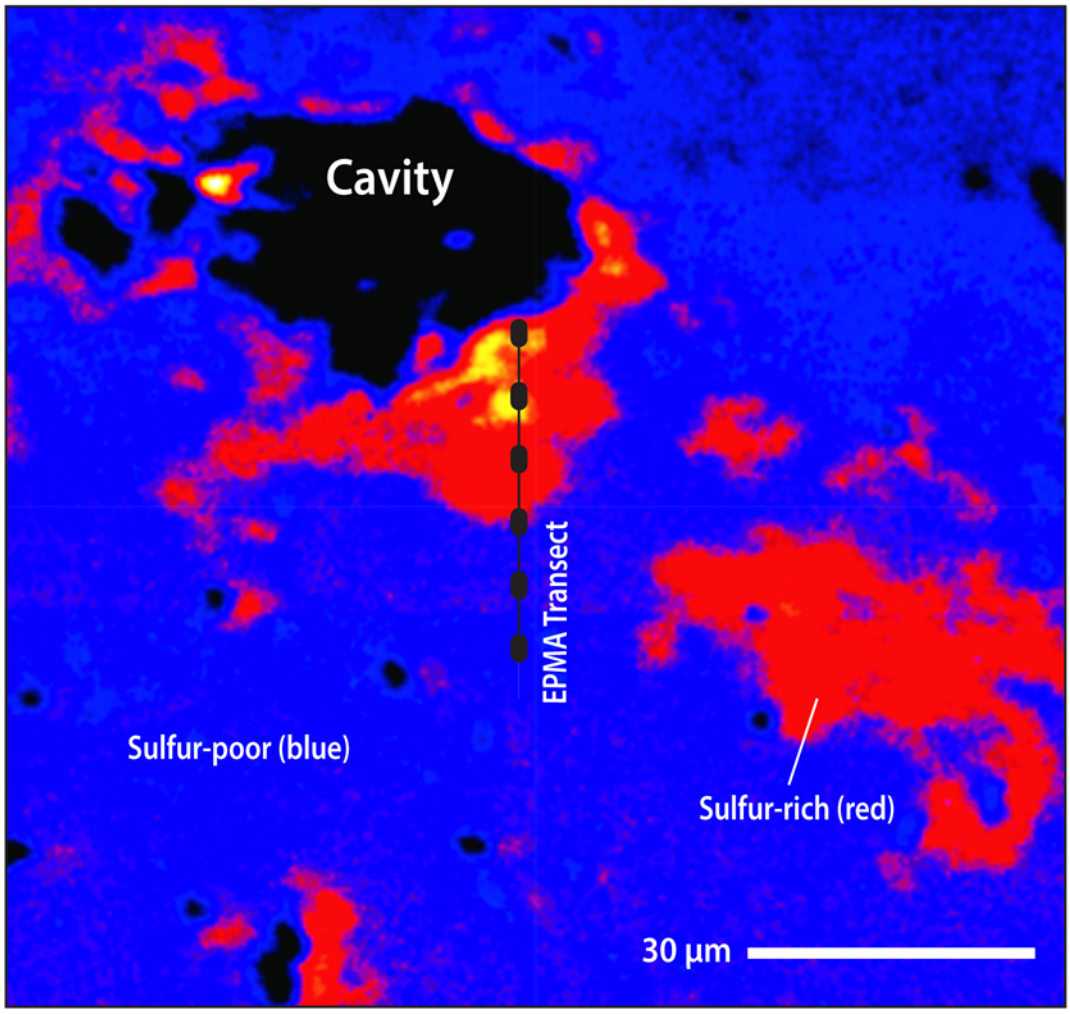

Appendix Figure B3: X-ray fluorescence (XRF) map of apatite from Mina Carmen (Treloar and Colley, 1996). The F-Cl-S contents measured along the EPMA transect are reported in Table A1. The appearance of the map is biased by the 45° angle of the incoming beam; i.e., areas on the right side of the cavity appear overexposed. Scale bar represents 30 µm.

REFERENCES

Anand, M., Tartèse, R., and Barnes, J.J. (2014) Understanding the origin and evolution of water in the Moon through lunar sample studies. Philosophical transactions. Series A, Mathematical, physical, and engineering sciences. 372, 224-252.

Ayris, P.M., Lee, a. F., Wilson, K., Kueppers, U., Dingwell, D.B., and Delmelle, P. (2013) SO2 sequestration in large volcanic eruptions: High-temperature scavenging by tephra. Geochimica et Cosmochimica Acta, 110, 58–69.

Baldridge W. S., Beaty D. W., Hill S. M. R., and Albee A. (1979) The petrology of the Apollo 12 pigeonite basalt suite. Proc. Lunar Planet. Sci. Conf. 10th, 141–179.

Berndt, J., Liebske, C., Holtz, F., Freise, M., Nowak, M., Ziegenbein, D., Hurkuck, W., and Koepke, J. (2002) A combined rapid-quench and H_2-membrane setup for internally heated pressure vessels: Description and application for water solubility in basaltic melts. American Mineralogist, 87, 1717–1726.

Boyce, J.W., Tomlinson, S.M., McCubbin, F.M., Greenwood, J.P., and Treiman, A.H. (2014) The lunar apatite paradox. Science (New York, N.Y.), 344, 400–402.

Boyce, J.W., Treiman, A.H., Guan, Y., Ma, C., Eiler, J.M., Gross, J., Greenwood, J.P., and Stolper, E.M., (2015) The chlorine isotope fingerprint of the lunar magma ocean. Science Advances, 1, 1-8.

Devine, J.D., Gardner, J.E., Brack, H.P., Layne, G.D., and Rutherford, M.J. (1995) Comparison of microanalytical methods for estimating H2O contents of silicic volcanic glasses. American Mineralogist, 80, 319–328.

Engvik, A.K., Golla-Schindler, U., Berndt, J., Austrheim, H., and Putnis, A. (2009) Intragranular replacement of chlorapatite by hydroxy-fluor-apatite during metasomatism. Lithos, 112, 236–246.

Fiege, A., Holtz, F., Behrens, H., Mandeville, C.W., Shimizu, N., Crede, L.S., and Göttlicher, J. (2015) Experimental investigation of the S and S-isotope distribution between H2O – S ± Cl fluids and basaltic melts during decompression. Chemical Geology, 393-394, 36–54.

Goldoff, B., Webster, J.D., and Harlov, D.E. (2012) Characterization of fluor-chlorapatites by electron probe microanalysis with a focus on time-dependent intensity variation of halogens. American Mineralogist, 97, 1103–1115.

Greenwood, J.P., Itoh, S., Sakamoto, N., Warren, P., Taylor, L., and Yurimoto, H. (2011) Hydrogen isotope ratios in lunar rocks indicate delivery of cometary water to the Moon. Nature Geoscience, 4, 79–82.

Harlov, D.E. (2015) Apatite: A Fingerprint for Metasomatic Processes. Elements, 11, 171–176.

Harlov, D.E., Wirth, R., and Förster, H.J. (2005) An experimental study of dissolution–reprecipitation in fluorapatite: fluid infiltration and the formation of monazite. Contributions to Mineralogy and Petrology, 150, 268–286.

Hovis, G.L., and Harlov, D.E. (2010) Solution calorimetric investigation of fluor-chlorapatite crystalline solutions. American Mineralogist, 95, 946–952.

Jarosewich E.., Nelen, J.A., and Norberg, J.A. (1980) Reference samples for electron microprobe analysis. Geostandards Newsletter, 4, 43–47.

Ketcham, R.A. (2015) Technical Note: Calculation of stoichiometry from EMP data for apatite and other phases with mixing on monovalent anion sites. American Mineralogist, 100, 1620–1623.

Knipping, J.L., Bilenker, L.D., Simon, A.C., Reich, M., Barra, F., Deditius, A.P., Lundstrom, C., Bindeman, I., and Munizaga, R. (2015) Giant Kiruna-type deposits form by efficient flotation of magmatic magnetite suspensions. Geology, 43, 591–594.

Konecke, B.A., Fiege, A., Simon, A.C., and Parat, F. (2017) Co-variability of S^{6+}, S^{4+} and S^{2-} in apatite as a function of oxidation state – implications for a new oxybarometer. American Mineralogist. 102, 548–557.

Krause, J., Harlov, D.E., Pushkarev, E. V., and Brügmann, G.E. (2013) Apatite and clinopyroxene as tracers for metasomatic processes in nepheline clinopyroxenites of Uralian-Alaskan-type complexes in the Ural Mountains, Russian Federation. Geochimica et Cosmochimica Acta, 121, 503–521.

Kusebauch, C., John, T., Whitehouse, M.J., Klemme, S., and Putnis, A. (2015) Distribution of halogens between fluid and apatite during fluid-mediated replacement processes. Geochimica et Cosmochimica Acta, 170, 225–246.

Luttinen, A. V., Zhang, X., and Foland, K.A. (2002) 159 Ma Kjakebeinet lamproites (Dronning Maud Land, Antarctica) and their implications for Gondwana breakup processes. Geological Magazine, 139, 525–539.

McCubbin, F.M., Jolliff, B.L., Nekvasil, H., Carpenter, P.K., Zeigler, R.A., Steele, A., Elardo, S.M., and Lindsley, D.H. (2011) Fluorine and chlorine abundances in lunar apatite: Implications for heterogeneous distributions of magmatic volatiles in the lunar interior. Geochimica et Cosmochimica Acta, 75, 5073–5093.

McCubbin, F.M., and Jones, R.H. (2015a) Extraterrestrial Apatite: Planetary Geochemistry to Astrobiology. Elements, 11, 183–188.

McCubbin, F.M., Kaaden, K.E. Vander, Tartèse, R., Klima, R.L., Liu, Y., Mortimer, J., Barnes, J.J., Shearer, C.K., Treiman, A.H., Lawrence, D.J., Elardo, S.M., Hurley, D.M., Boyce, J.W., and Anand, M. (2015b) Magmatic volatiles (H, C, N, F, S, Cl) in the lunar mantle, crust, and regolith: Abundances, distributions, processes, and reservoirs. American Mineralogist, 100, 1668–1707.

Nadeau, O., Williams-Jones, A.E., and Stix, J. (2010) Sulphide magma as a source of metals in arc-related magmatic hydrothermal ore fluids. Nature Geoscience, 3, 501–505.

Ohlhorst, S., Behrens, H., and Holtz, F. (2001) Compositional dependence of molar absorptivities of near-infrared OH-and H_2O bands in rhyolitic to basaltic glasses. Chemical Geology, 174, 5–20.

Rhodes, J.M, Blanchard D.P, M.A. Dungan, J.C Brannon, Rodgers, K. (1977) Chemistry of Apollo 12 mare basalts: Magma types and fractionation processes. Proc. Lunar Sci. Conf. 8th, 1305–1338.

Stormer, J.C., Pierson, M.L., and Tackler, R.C. (1993) Variation of F and Cl X-ray intensity due to anisotropic diffusion in apatite during electron microprobe analysis. American Mineralogist, 78, 641–648.

Taylor G. J., Warren P., Ryder G., Delano J., Pieters C. and Lofgren G. (1991) Chapter 6: Lunar Rocks. In Lunar Sourcebook. A User's Guide to the Moon, 183–284.

Treloar, P.J., and Colley, H. (1996) Variation in F and Cl contents in apatites from magnetite-apatite ores in northern Chile, and their ore-genetic implications: Mineralogical Magazine, 60, 285–301.

Ustunisik, G., Nekvasil, H., Lindsley, D.H., and McCubbin, F.M. (2015) Degassing pathways of Cl-, F-, H-, and S-bearing magmas near the lunar surface: Implications for the composition and Cl isotopic values of lunar apatite. American Mineralogist, 100, 1717–1727.

Zajacz, Z., Candela, P. A., Piccoli, P.M., Wälle, M., and Sanchez-Valle, C. (2012) Gold and copper in volatile saturated mafic to intermediate magmas: Solubilities, partitioning, and implications for ore deposit formation. Geochimica et Cosmochimica Acta, 91, 140–159.

APPENDIX C

SUPPLEMENTARY S-XANES DATA

Appendix Table C1: S-XANES apatite spectra of Series #1 experiments

LA45-IH27		LA45-IH1		LA45-IH30		LA45-IH7		LA45-IH13	
[eV]	Intensity	[eV]	Intensity	[eV]	Intensity	[eV]	Intensity	[eV]	Intensity
2435.000	0.016	2460.000	0.045	2445.000	-0.086	2460.000	-0.075	2460.000	-0.018
2438.200	0.002	2461.000	-0.018	2446.000	-0.015	2461.000	-0.057	2461.000	0.056
2441.400	-0.007	2462.000	-0.004	2447.000	-0.021	2462.000	0.019	2462.000	0.071
2444.600	0.008	2463.000	-0.003	2448.000	0.037	2463.000	0.058	2463.000	0.014
2447.800	0.000	2464.000	-0.013	2449.000	-0.009	2464.000	0.032	2464.000	-0.005
2451.000	-0.002	2464.300	0.031	2450.000	0.047	2464.200	-0.002	2464.200	-0.002
2454.200	0.002	2464.600	-0.008	2451.000	0.047	2464.400	0.014	2464.400	-0.032
2457.400	-0.002	2464.900	0.000	2452.000	0.058	2464.600	-0.003	2464.600	-0.021
2460.600	-0.007	2465.200	-0.018	2453.000	0.032	2464.800	-0.043	2464.800	-0.047
2463.800	0.033	2465.500	0.013	2454.000	-0.028	2465.000	0.000	2465.000	-0.028
2467.000	0.152	2465.800	0.019	2455.000	-0.099	2465.200	-0.011	2465.200	-0.048
2467.100	0.169	2466.100	-0.001	2456.000	-0.089	2465.400	-0.025	2465.400	-0.026
2467.200	0.122	2466.40	-0.001	2457.000	-0.006	2465.600	-0.004	2465.600	-0.013
2467.300	0.149	2466.700	0.024	2458.000	0.013	2465.800	0.008	2465.800	0.020
2467.400	0.142	2467.000	-0.004	2459.000	0.024	2466.000	-0.015	2466.000	-0.019
2467.500	0.153	2467.300	0.005	2460.000	0.108	2466.200	0.019	2466.200	-0.003
2467.600	0.149	2467.600	-0.019	2461.000	0.128	2466.400	0.050	2466.400	0.032
2467.700	0.135	2467.900	0.162	2462.000	0.100	2466.600	0.027	2466.600	0.003
2467.800	0.176	2468.200	0.563	2463.000	0.045	2466.800	-0.013	2466.800	0.025
2467.900	0.189	2468.500	1.026	2464.000	-0.039	2467.000	-0.038	2467.000	0.029
2468.000	0.151	2468.800	2.005	2464.200	-0.050	2467.200	-0.019	2467.200	0.047
2468.100	0.220	2469.100	3.466	2464.400	-0.011	2467.400	0.016	2467.400	0.030
2468.200	0.258	2469.400	4.105	2464.600	-0.042	2467.600	0.007	2467.600	-0.011
2468.300	0.285	2469.700	4.381	2464.800	-0.001	2467.800	0.003	2467.800	0.006
2468.400	0.315	2470.000	4.289	2465.000	-0.009	2468.000	0.010	2468.000	0.040
2468.500	0.331	2470.300	4.101	2465.200	-0.029	2468.200	0.042	2468.200	-0.048
2468.600	0.425	2470.600	3.491	2465.400	0.048	2468.400	0.028	2468.400	-0.002
2468.700	0.455	2470.900	3.001	2465.600	-0.022	2468.600	0.043	2468.600	-0.012

2468.800	0.569	2471.200	2.197	2465.800	0.001	2468.800	0.056	2468.800	0.033
2468.900	0.627	2471.500	2.213	2466.000	0.007	2469.000	0.037	2469.000	0.036
2469.000	0.718	2471.800	2.062	2466.200	0.028	2469.200	0.019	2469.200	0.013
2469.100	0.813	2472.100	2.134	2466.400	0.019	2469.400	-0.005	2469.400	0.016
2469.200	0.887	2472.400	2.210	2466.600	0.015	2469.600	0.017	2469.600	0.034
2469.300	0.960	2472.700	2.740	2466.800	0.018	2469.800	0.020	2469.800	-0.041
2469.400	1.063	2473.000	2.777	2467.000	-0.016	2470.000	-0.008	2470.000	0.016
2469.500	1.135	2473.300	3.072	2467.200	-0.001	2470.200	-0.029	2470.200	0.005
2469.600	1.115	2473.600	3.305	2467.400	-0.065	2470.400	0.011	2470.400	0.029
2469.700	1.127	2473.900	3.387	2467.600	-0.075	2470.600	0.012	2470.600	-0.002
2469.800	1.144	2474.200	3.757	2467.800	-0.048	2470.800	0.011	2470.800	0.025
2469.900	1.172	2474.500	3.928	2468.000	0.006	2471.000	0.009	2471.000	0.045
2470.000	1.145	2474.800	4.166	2468.200	0.046	2471.200	0.005	2471.200	0.059
2470.100	1.177	2475.100	4.264	2468.400	0.124	2471.400	-0.010	2471.400	0.054
2470.200	1.122	2475.400	4.265	2468.600	0.317	2471.600	0.065	2471.600	0.034
2470.300	1.169	2475.700	4.405	2468.800	0.566	2471.800	-0.003	2471.800	0.000
2470.400	1.127	2476.000	4.362	2469.000	0.823	2472.000	0.012	2472.000	0.070
2470.500	1.089	2476.300	4.933	2469.200	1.061	2472.200	-0.006	2472.200	0.040
2470.600	1.056	2476.600	4.855	2469.400	1.140	2472.400	-0.012	2472.400	-0.013
2470.700	0.999	2476.900	5.225	2469.600	1.232	2472.600	0.001	2472.600	-0.029
2470.800	0.940	2477.200	5.299	2469.800	1.192	2472.800	0.065	2472.800	0.015
2470.900	0.876	2477.500	5.202	2470.000	1.168	2473.000	-0.003	2473.000	0.013
2471.000	0.885	2477.800	5.091	2470.200	1.080	2473.200	-0.022	2473.200	-0.026
2471.100	0.837	2478.100	4.668	2470.400	0.960	2473.400	0.051	2473.400	0.030
2471.200	0.809	2478.400	4.625	2470.600	0.910	2473.600	0.007	2473.600	0.013
2471.300	0.804	2478.700	4.255	2470.800	0.748	2473.800	0.008	2473.800	0.035
2471.400	0.732	2479.000	4.156	2471.000	0.681	2474.000	0.032	2474.000	0.054
2471.500	0.721	2479.300	3.773	2471.200	0.617	2474.200	0.061	2474.200	0.046
2471.600	0.753	2479.600	3.759	2471.400	0.620	2474.400	0.047	2474.400	0.074
2471.700	0.763	2479.900	3.585	2471.600	0.618	2474.600	0.041	2474.600	0.060
2471.800	0.720	2480.200	3.535	2471.800	0.694	2474.800	0.045	2474.800	-0.004
2471.900	0.734	2480.500	3.790	2472.000	0.813	2475.000	0.016	2475.000	0.006
2472.000	0.704	2480.800	4.580	2472.200	0.886	2475.200	0.107	2475.200	0.005
2472.100	0.757	2481.100	5.652	2472.400	0.947	2475.400	0.067	2475.400	0.048
2472.200	0.778	2481.400	6.800	2472.600	1.093	2475.600	0.116	2475.600	0.026
2472.300	0.783	2481.700	7.546	2472.800	1.125	2475.800	0.124	2475.800	0.020
2472.400	0.793	2482.000	7.340	2473.000	1.168	2476.000	0.154	2476.000	0.001
2472.500	0.843	2482.300	6.453	2473.200	1.178	2476.200	0.133	2476.200	0.103
2472.600	0.838	2482.600	4.965	2473.400	1.229	2476.400	0.207	2476.400	0.176
2472.700	0.891	2482.900	3.250	2473.600	1.157	2476.600	0.312	2476.600	0.267
2472.800	0.885	2483.200	2.188	2473.800	1.196	2476.800	0.520	2476.800	0.487
2472.900	0.930	2483.500	1.901	2474.000	1.210	2477.000	0.720	2477.000	0.797
2473.000	0.941	2483.800	1.626	2474.200	1.266	2477.200	0.966	2477.200	1.168

2473.100	0.952	2484.100	1.453	2474.400	1.251	2477.400	1.166	2477.400	1.497
2473.200	1.006	2484.400	1.408	2474.600	1.300	2477.600	1.196	2477.600	1.524
2473.300	1.042	2484.700	1.469	2474.800	1.349	2477.800	1.081	2477.800	1.448
2473.400	1.023	2485.000	1.399	2475.000	1.330	2478.000	0.881	2478.000	1.134
2473.500	1.082	2485.300	1.567	2475.200	1.356	2478.200	0.707	2478.200	0.871
2473.600	1.141	2485.600	1.767	2475.400	1.398	2478.400	0.486	2478.400	0.514
2473.700	1.139	2485.900	1.792	2475.600	1.467	2478.600	0.385	2478.600	0.323
2473.800	1.154	2486.200	1.862	2475.800	1.489	2478.800	0.346	2478.800	0.326
2473.900	1.138	2486.500	1.719	2476.000	1.566	2479.000	0.350	2479.000	0.370
2474.000	1.215	2486.800	1.664	2476.200	1.466	2479.200	0.455	2479.200	0.546
2474.100	1.204	2487.100	1.581	2476.400	1.589	2479.400	0.613	2479.400	0.631
2474.200	1.276	2487.400	1.673	2476.600	1.706	2479.600	0.696	2479.600	0.850
2474.300	1.237	2487.700	1.611	2476.800	1.732	2479.800	0.925	2479.800	1.241
2474.400	1.284	2488.000	1.586	2477.000	1.858	2480.000	1.332	2480.000	1.795
2474.500	1.307	2489.000	1.598	2477.200	2.047	2480.200	1.894	2480.200	2.682
2474.600	1.285	2490.000	1.886	2477.400	2.156	2480.400	2.932	2480.400	4.170
2474.700	1.311	2491.000	1.710	2477.600	2.130	2480.600	4.321	2480.600	6.394
2474.800	1.384	2492.000	1.770	2477.800	2.130	2480.800	6.170	2480.800	9.597
2474.900	1.351	2493.000	1.790	2478.000	2.043	2481.000	8.526	2481.000	13.166
2475.000	1.376	2494.000	1.653	2478.200	1.778	2481.200	10.720	2481.200	16.749
2475.100	1.399	2495.000	1.404	2478.400	1.614	2481.400	12.794	2481.400	20.047
2475.200	1.445	2496.000	1.177	2478.600	1.554	2481.600	14.118	2481.600	22.107
2475.300	1.446	2497.000	1.264	2478.800	1.487	2481.800	14.746	2481.800	23.447
2475.400	1.427	2498.000	0.988	2479.000	1.497	2482.000	14.465	2482.000	23.459
2475.500	1.451	2499.000	1.346	2479.200	1.502	2482.200	13.182	2482.200	22.034
2475.600	1.492	2500.000	1.233	2479.400	1.477	2482.400	11.309	2482.400	18.847
2475.700	1.495	2501.000	1.264	2479.600	1.522	2482.600	8.691	2482.600	14.737
2475.800	1.505	2502.000	1.358	2479.800	1.570	2482.800	6.334	2482.800	10.499
2475.900	1.575	2503.000	1.296	2480.000	1.699	2483.000	4.448	2483.000	7.179
2476.000	1.508	2504.000	1.492	2480.200	1.899	2483.200	3.234	2483.200	5.109
2476.100	1.525	2505.000	1.606	2480.400	2.361	2483.400	2.558	2483.400	3.833
2476.200	1.540	2506.000	1.407	2480.600	3.121	2483.600	2.037	2483.600	2.941
2476.300	1.571	2507.000	1.420	2480.800	4.169	2483.800	1.709	2483.800	2.510
2476.400	1.582	2508.000	1.140	2481.000	5.416	2484.000	1.519	2484.000	2.220
2476.500	1.600	2509.000	1.197	2481.200	6.833	2484.200	1.455	2484.200	2.053
2476.600	1.626	2510.000	1.082	2481.400	8.040	2484.400	1.440	2484.400	2.005
2476.700	1.660	2511.000	0.949	2481.600	8.975	2484.600	1.438	2484.600	2.189
2476.800	1.610	2512.000	0.974	2481.800	9.235	2484.800	1.509	2484.800	2.317
2476.900	1.644	2513.000	0.863	2482.000	8.987	2485.000	1.547	2485.000	2.511
2477.000	1.607	2514.000	0.753	2482.200	8.229	2485.200	1.524	2485.200	2.596
2477.100	1.657	2515.000	0.686	2482.400	6.909	2485.400	1.584	2485.400	2.754
2477.200	1.665	2516.000	0.675	2482.600	5.411	2485.600	1.555	2485.600	2.773
2477.300	1.637	2517.000	0.896	2482.800	3.966	2485.800	1.527	2485.800	2.744

2477.400	1.629	2518.000	0.859	2483.000	2.868	2486.000	1.414	2486.000	2.546
2477.500	1.649	2519.000	0.983	2483.200	2.127	2486.200	1.292	2486.200	2.361
2477.600	1.661	2520.000	0.848	2483.400	1.854	2486.400	1.255	2486.400	2.191
2477.700	1.662	2521.000	1.028	2483.600	1.499	2486.600	1.148	2486.600	2.029
2477.800	1.668	2522.000	0.949	2483.800	1.391	2486.800	0.970	2486.800	1.837
2477.900	1.636	2523.000	1.032	2484.000	1.241	2487.000	0.924	2487.000	1.531
2478.000	1.644	2524.000	0.979	2484.200	1.154	2487.200	0.816	2487.200	1.422
2478.100	1.620	2525.000	1.175	2484.400	1.197	2487.400	0.733	2487.400	1.228
2478.200	1.645	2526.000	1.086	2484.600	1.222	2487.600	0.716	2487.600	1.109
2478.300	1.581	2527.000	1.462	2484.800	1.277	2487.800	0.596	2487.800	1.012
2478.400	1.603	2528.000	1.197	2485.000	1.313	2488.000	0.657	2488.000	0.979
2478.500	1.568	2529.000	1.062	2485.200	1.378	2489.000	0.693	2489.000	0.926
2478.600	1.547	2530.000	1.241	2485.400	1.367	2490.000	1.025	2490.000	1.469
2478.700	1.524	2531.000	0.911	2485.600	1.317	2491.000	1.489	2491.000	2.233
2478.800	1.551	2532.000	1.151	2485.800	1.272	2492.000	2.186	2492.000	3.403
2478.900	1.546	2533.000	1.141	2486.000	1.224	2493.000	2.785	2493.000	4.618
2479.000	1.555	2534.000	1.031	2486.200	1.157	2494.000	2.563	2494.000	3.956
2479.100	1.522	2535.000	1.109	2486.400	1.152	2495.000	2.285	2495.000	3.149
2479.200	1.545	2536.000	0.882	2486.600	1.061	2496.000	2.423	2496.000	3.387
2479.300	1.533	2537.000	1.197	2486.800	1.030	2497.000	2.488	2497.000	3.412
2479.400	1.521	2538.000	1.015	2487.000	0.911	2498.000	2.499	2498.000	3.321
2479.500	1.491	2539.000	0.999	2487.200	0.899	2499.000	2.604	2499.000	3.459
2479.600	1.466	2540.000	0.879	2487.400	0.784	2500.000	2.515	2500.000	3.140
2479.700	1.474			2487.600	0.786	2501.000	2.319	2501.000	2.867
2479.800	1.486			2487.800	0.733	2502.000	2.208	2502.000	2.583
2479.900	1.487			2488.000	0.680	2503.000	2.020	2503.000	2.298
2480.000	1.469			2489.510	0.591	2504.000	1.850	2504.000	1.947
2480.100	1.459			2491.020	0.804	2505.000	1.671	2505.000	1.649
2480.200	1.506			2492.540	1.177	2506.000	1.509	2506.000	1.344
2480.300	1.493			2494.050	1.069	2507.000	1.376	2507.000	1.116
2480.400	1.567			2495.560	0.894	2508.000	1.264	2508.000	0.920
2480.500	1.604			2497.070	1.047	2509.000	1.215	2509.000	0.947
2480.600	1.612			2498.590	1.039	2510.000	1.176	2510.000	0.802
2480.700	1.674			2500.100	1.075	2511.000	1.138	2511.000	0.738
2480.800	1.795			2501.610	0.985	2512.000	1.093	2512.000	0.730
2480.900	1.869			2503.120	0.934	2513.000	1.023	2513.000	0.706
2481.000	1.973			2504.630	0.904	2514.000	1.086	2514.000	0.808
2481.100	2.023			2506.150	0.866	2515.000	1.062	2515.000	0.821
2481.200	2.080			2507.660	0.892	2516.000	1.161	2516.000	0.821
2481.300	2.223			2509.170	0.877	2517.000	1.202	2517.000	0.905
2481.400	2.309			2510.680	0.928	2518.000	1.211	2518.000	0.895
2481.500	2.349			2512.200	0.910	2519.000	1.305	2519.000	0.911
2481.600	2.418			2513.710	0.939	2520.000	1.279	2520.000	0.918

2481.700	2.448	2515.220	0.928	2521.000	1.302	2521.000	0.940
2481.800	2.424	2516.730	0.903	2522.000	1.274	2522.000	0.922
2481.900	2.447	2518.240	0.976	2523.000	1.360	2523.000	0.919
2482.000	2.371	2519.760	1.068	2524.000	1.283	2524.000	0.930
2482.100	2.286	2521.270	1.016	2525.000	1.246	2525.000	0.908
2482.200	2.255	2522.780	1.061	2526.000	1.182	2526.000	0.909
2482.300	2.178	2524.290	1.134	2527.000	1.185	2527.000	0.966
2482.400	2.096	2525.800	1.101	2528.000	1.105	2528.000	0.989
2482.500	1.951	2527.320	1.217	2529.000	1.053	2529.000	0.955
2482.600	1.846	2528.830	1.158	2530.000	0.990	2530.000	0.945
2482.700	1.757	2530.340	1.174	2531.000	0.933	2531.000	0.919
2482.800	1.646	2531.850	1.166	2532.000	0.952	2532.000	0.951
2482.900	1.533	2533.370	1.204	2533.000	0.915	2533.000	0.924
2483.000	1.499	2534.880	1.156	2534.000	0.913	2534.000	0.954
2483.100	1.450	2536.390	1.101	2535.000	0.919	2535.000	0.970
2483.200	1.400	2537.900	1.102	2536.000	0.898	2536.000	0.992
2483.300	1.320	2539.410	0.989	2537.000	0.955	2537.000	0.985
2483.400	1.292	2540.930	1.043	2538.000	0.911	2538.000	0.999
2483.500	1.276	2542.440	0.907	2539.000	0.934	2539.000	1.068
2483.600	1.290	2543.950	0.850	2540.000	0.967	2540.000	1.054
2483.700	1.296	2545.460	0.860	2541.000	0.921		
2483.800	1.257	2546.980	0.843	2542.000	0.919		
2483.900	1.278	2548.490	0.834	2543.000	0.880		
2484.000	1.224	2550.000	0.813	2544.000	0.908		
2484.100	1.204			2545.000	0.926		
2484.200	1.207			2546.000	0.876		
2484.300	1.279			2547.000	0.904		
2484.400	1.215			2548.000	0.850		
2484.500	1.207			2549.000	0.807		
2484.600	1.225			2550.000	0.823		
2484.700	1.233						
2484.800	1.224						
2484.900	1.273						
2485.000	1.243						
2485.100	1.182						
2485.200	1.239						
2485.300	1.243						
2485.400	1.239						
2485.500	1.228						
2485.600	1.259						
2485.700	1.250						
2485.800	1.269						
2485.900	1.210						

2486.000	1.229
2486.100	1.237
2486.200	1.220
2486.300	1.227
2486.400	1.225
2486.500	1.179
2486.600	1.241
2486.700	1.212
2486.800	1.223
2486.900	1.250
2487.000	1.221
2488.000	1.234
2489.000	1.219
2490.000	1.187
2491.000	1.199
2492.000	1.239
2493.000	1.262
2494.000	1.276
2495.000	1.356
2496.000	1.336
2497.000	1.319
2498.000	1.359
2499.000	1.372
2500.000	1.339
2501.000	1.325
2502.000	1.256
2503.000	1.308
2504.000	1.339
2505.000	1.326
2506.000	1.314
2507.000	1.332
2508.000	1.269
2509.000	1.221
2510.000	1.192
2511.000	1.176
2512.000	1.135
2513.000	1.123
2514.000	1.064
2515.000	1.045
2516.000	1.024
2517.000	0.979
2518.000	1.003
2519.000	1.048

2520.000	0.980
2521.000	1.000
2522.000	1.006
2523.000	1.003
2524.000	1.008
2525.000	0.939
2526.000	1.003
2527.000	1.033
2528.000	0.989
2529.000	0.935
2530.000	0.987
2531.000	0.980
2532.000	1.000
2533.000	1.006
2534.000	1.003
2535.000	1.008
2536.000	0.939
2537.000	1.003
2538.000	1.033
2539.000	0.989
2540.000	0.935

Appendix Table C2: S-XANES apatite spectra of Series #2 experiments

LA45-IH28		LA45-IH2		LA45-IH34		LA45-IH8		LA45-IH14	
[eV]	Intensity	[eV]	Intensity	[eV]	Intensity	[eV]	Intensity	[eV]	Intensity
2445.000	-0.086	2450.000	-0.035	2445.000	-0.110	2455.000	0.048	2450.000	-0.015
2446.000	-0.055	2452.830	0.061	2446.000	-0.060	2456.000	0.011	2451.000	-0.007
2447.000	-0.019	2455.670	0.005	2447.000	0.001	2457.000	-0.037	2452.000	0.013
2448.000	0.001	2458.500	-0.020	2448.000	0.033	2458.000	0.011	2453.000	0.020
2449.000	0.007	2461.330	-0.030	2449.000	0.018	2459.000	-0.028	2454.000	0.039
2450.000	0.008	2464.170	0.002	2450.000	0.017	2460.000	-0.009	2455.000	0.035
2451.000	0.013	2467.000	0.017	2451.000	0.004	2461.000	-0.037	2456.000	0.050
2452.000	0.010	2467.100	0.061	2452.000	-0.003	2462.000	0.013	2457.000	0.023
2453.000	0.010	2467.200	0.204	2453.000	0.019	2463.000	-0.042	2458.000	0.023
2454.000	0.003	2467.300	0.151	2454.000	0.014	2464.000	0.015	2459.000	0.038
2455.000	0.005	2467.400	0.069	2455.000	-0.004	2464.300	0.027	2460.000	0.020
2456.000	-0.002	2467.500	0.170	2456.000	-0.006	2464.600	0.011	2461.000	-0.018
2457.000	-0.013	2467.600	-0.056	2457.000	-0.010	2464.900	0.017	2462.000	-0.010
2458.000	-0.009	2467.700	0.234	2458.000	-0.006	2465.200	0.019	2463.000	-0.011
2459.000	-0.019	2467.800	0.246	2459.000	-0.008	2465.500	0.024	2464.000	-0.060
2460.000	-0.010	2467.900	0.254	2460.000	-0.018	2465.800	-0.007	2464.200	-0.054
2461.000	-0.007	2468.000	0.311	2461.000	-0.008	2466.100	0.006	2464.400	-0.037
2462.000	-0.013	2468.100	0.199	2462.000	-0.034	2466.400	0.013	2464.600	-0.021
2463.000	-0.010	2468.200	0.248	2463.000	-0.018	2466.700	-0.029	2464.800	-0.031
2464.000	0.010	2468.300	0.296	2464.000	-0.021	2467.000	-0.002	2465.000	-0.015
2464.200	0.014	2468.400	0.355	2464.200	-0.022	2467.300	-0.013	2465.200	-0.025
2464.400	0.015	2468.500	0.484	2464.400	-0.017	2467.600	0.020	2465.400	-0.016
2464.600	0.007	2468.600	0.446	2464.600	-0.001	2467.900	-0.015	2465.600	-0.005
2464.800	0.024	2468.700	0.569	2464.800	-0.021	2468.200	0.011	2465.800	-0.007
2465.000	0.038	2468.800	0.731	2465.000	0.006	2468.500	-0.002	2466.000	-0.008
2465.200	0.034	2468.900	0.787	2465.200	0.018	2468.800	0.000	2466.200	-0.001
2465.400	0.060	2469.000	0.779	2465.400	0.027	2469.100	-0.019	2466.400	0.011
2465.600	0.074	2469.100	0.920	2465.600	0.033	2469.400	-0.066	2466.600	-0.008
2465.800	0.099	2469.200	0.943	2465.800	0.059	2469.700	-0.049	2466.800	0.001
2466.000	0.127	2469.300	0.835	2466.000	0.088	2470.000	-0.017	2467.000	0.008
2466.200	0.150	2469.400	1.190	2466.200	0.106	2470.300	-0.036	2467.200	-0.013
2466.400	0.172	2469.500	1.222	2466.400	0.123	2470.600	-0.061	2467.400	-0.048
2466.600	0.187	2469.600	1.345	2466.600	0.151	2470.900	-0.001	2467.600	-0.029
2466.800	0.199	2469.700	1.325	2466.800	0.141	2471.200	0.008	2467.800	-0.055
2467.000	0.212	2469.800	1.267	2467.000	0.167	2471.500	0.000	2468.000	-0.057
2467.200	0.189	2469.900	1.319	2467.200	0.125	2471.800	0.071	2468.200	-0.016
2467.400	0.179	2470.000	1.362	2467.400	0.140	2472.100	0.070	2468.400	-0.033
2467.600	0.181	2470.100	1.276	2467.600	0.111	2472.400	0.134	2468.600	-0.026
2467.800	0.186	2470.200	1.175	2467.800	0.099	2472.700	0.131	2468.800	-0.019

2468.000	0.204	2470.300	1.235	2468.000	0.124	2473.000	0.129	2469.000	-0.030
2468.200	0.235	2470.400	1.236	2468.200	0.155	2473.300	0.163	2469.200	0.000
2468.400	0.302	2470.500	1.094	2468.400	0.183	2473.600	0.171	2469.400	-0.009
2468.600	0.395	2470.600	1.098	2468.600	0.243	2473.900	0.289	2469.600	0.019
2468.800	0.536	2470.700	0.878	2468.800	0.352	2474.200	0.214	2469.800	-0.007
2469.000	0.706	2470.800	0.988	2469.000	0.473	2474.500	0.257	2470.000	0.014
2469.200	0.885	2470.900	0.901	2469.200	0.563	2474.800	0.258	2470.200	0.007
2469.400	1.020	2471.000	0.910	2469.400	0.604	2475.100	0.265	2470.400	0.021
2469.600	1.111	2471.100	0.994	2469.600	0.628	2475.400	0.356	2470.600	0.016
2469.800	1.186	2471.200	0.840	2469.800	0.621	2475.700	0.396	2470.800	0.013
2470.000	1.217	2471.300	0.801	2470.000	0.628	2476.000	0.428	2471.000	0.033
2470.200	1.203	2471.400	0.820	2470.200	0.617	2476.300	0.669	2471.200	0.005
2470.400	1.152	2471.500	0.775	2470.400	0.580	2476.600	0.679	2471.400	0.031
2470.600	1.099	2471.600	0.819	2470.600	0.548	2476.900	1.016	2471.600	0.046
2470.800	1.015	2471.700	0.757	2470.800	0.527	2477.200	1.295	2471.800	0.035
2471.000	0.941	2471.800	0.691	2471.000	0.494	2477.500	1.176	2472.000	0.003
2471.200	0.859	2471.900	0.875	2471.200	0.485	2477.800	1.683	2472.200	0.037
2471.400	0.809	2472.000	0.784	2471.400	0.502	2478.100	1.498	2472.400	0.005
2471.600	0.756	2472.100	0.776	2471.600	0.521	2478.400	1.004	2472.600	-0.003
2471.800	0.747	2472.200	0.787	2471.800	0.532	2478.700	0.850	2472.800	0.032
2472.000	0.743	2472.300	0.889	2472.000	0.569	2479.000	0.946	2473.000	0.044
2472.200	0.766	2472.400	0.866	2472.200	0.605	2479.300	1.100	2473.200	0.056
2472.400	0.818	2472.500	0.772	2472.400	0.630	2479.600	1.410	2473.400	0.058
2472.600	0.843	2472.600	0.835	2472.600	0.655	2479.900	1.754	2473.600	0.049
2472.800	0.890	2472.700	1.003	2472.800	0.680	2480.200	2.415	2473.800	0.081
2473.000	0.942	2472.800	1.008	2473.000	0.696	2480.500	3.943	2474.000	0.083
2473.200	1.004	2472.900	0.937	2473.200	0.707	2480.800	6.389	2474.200	0.089
2473.400	1.060	2473.000	1.155	2473.400	0.696	2481.100	9.637	2474.400	0.067
2473.600	1.106	2473.100	0.910	2473.600	0.719	2481.400	12.584	2474.600	0.076
2473.800	1.147	2473.200	1.168	2473.800	0.706	2481.700	14.306	2474.800	0.089
2474.000	1.197	2473.300	1.103	2474.000	0.723	2482.000	13.978	2475.000	0.091
2474.200	1.248	2473.400	0.989	2474.200	0.724	2482.300	11.724	2475.200	0.112
2474.400	1.292	2473.500	1.213	2474.400	0.732	2482.600	8.271	2475.400	0.083
2474.600	1.322	2473.600	1.034	2474.600	0.745	2482.900	5.544	2475.600	0.116
2474.800	1.359	2473.700	1.147	2474.800	0.760	2483.200	3.554	2475.800	0.150
2475.000	1.391	2473.800	1.197	2475.000	0.799	2483.500	2.576	2476.000	0.168
2475.200	1.422	2473.900	1.218	2475.200	0.819	2483.800	2.163	2476.200	0.201
2475.400	1.448	2474.000	1.272	2475.400	0.827	2484.100	2.029	2476.400	0.222
2475.600	1.459	2474.100	1.305	2475.600	0.857	2484.400	1.988	2476.600	0.265
2475.800	1.509	2474.200	1.225	2475.800	0.899	2484.700	2.079	2476.800	0.385
2476.000	1.544	2474.300	1.281	2476.000	0.919	2485.000	2.076	2477.000	0.448
2476.200	1.561	2474.400	1.295	2476.200	0.944	2485.300	2.257	2477.200	0.601
2476.400	1.577	2474.500	1.513	2476.400	0.958	2485.600	2.193	2477.400	0.686

2476.600	1.648	2474.600	1.409	2476.600	1.046	2485.900	2.144	2477.600	0.757
2476.800	1.577	2474.700	1.328	2476.800	1.024	2486.200	2.064	2477.800	0.720
2477.000	1.593	2474.800	1.469	2477.000	1.082	2486.500	1.891	2478.000	0.546
2477.200	1.604	2474.900	1.467	2477.200	1.187	2486.800	1.840	2478.200	0.571
2477.400	1.633	2475.000	1.508	2477.400	1.245	2487.100	1.696	2478.400	0.496
2477.600	1.605	2475.100	1.372	2477.600	1.310	2487.400	1.632	2478.600	0.461
2477.800	1.588	2475.200	1.445	2477.800	1.253	2487.700	1.590	2478.800	0.489
2478.200	1.586	2475.300	1.567	2478.000	1.466	2488.000	1.585	2479.000	0.485
2478.400	1.581	2475.400	1.575	2478.200	1.149	2489.000	1.595	2479.200	0.571
2478.600	1.586	2475.500	1.684	2478.400	1.108	2490.000	1.769	2479.400	0.613
2478.800	1.567	2475.600	1.551	2478.600	1.059	2491.000	2.197	2479.600	0.735
2479.000	1.570	2475.700	1.640	2478.800	1.040	2492.000	2.708	2479.800	0.903
2479.200	1.571	2475.800	1.554	2479.000	1.063	2493.000	3.241	2480.000	1.109
2479.400	1.581	2475.900	1.619	2479.200	1.078	2494.000	3.056	2480.200	1.519
2479.600	1.597	2476.000	1.776	2479.400	1.115	2495.000	2.855	2480.400	2.133
2479.800	1.604	2476.100	1.529	2479.600	1.158	2496.000	3.032	2480.600	3.119
2480.000	1.622	2476.200	1.654	2479.800	1.229	2497.000	3.157	2480.800	4.303
2480.200	1.667	2476.300	1.703	2480.000	1.318	2498.000	3.189	2481.000	5.972
2480.400	1.678	2476.400	1.760	2480.200	1.472	2499.000	3.163	2481.200	7.643
2480.600	1.710	2476.500	1.742	2480.400	1.733	2500.000	2.950	2481.400	9.032
2480.800	1.761	2476.600	1.755	2480.600	2.112	2501.000	2.595	2481.600	10.018
2481.000	1.854	2476.700	1.760	2480.800	2.661	2502.000	2.201	2481.800	10.341
2481.200	1.956	2476.800	1.820	2481.000	3.346	2503.000	1.919	2482.000	10.044
2481.400	2.063	2476.900	1.790	2481.200	4.145	2504.000	1.553	2482.200	9.246
2481.600	2.092	2477.000	1.754	2481.400	4.821	2505.000	1.359	2482.400	7.634
2481.800	2.095	2477.100	1.893	2481.600	5.326	2506.000	1.235	2482.600	5.964
2482.000	2.001	2477.200	1.840	2481.800	5.553	2507.000	1.054	2482.800	4.318
2482.200	1.854	2477.300	1.864	2482.000	5.424	2508.000	0.962	2483.000	3.075
2482.400	1.715	2477.400	1.829	2482.200	5.041	2509.000	0.960	2483.200	2.319
2482.600	1.574	2477.500	1.863	2482.400	4.382	2510.000	0.928	2483.400	1.909
2482.800	1.435	2477.600	1.825	2482.600	3.531	2511.000	0.911	2483.600	1.607
2483.000	1.362	2477.700	1.762	2482.800	2.741	2512.000	0.906	2483.800	1.419
2483.200	1.287	2477.800	1.805	2483.000	2.110	2513.000	0.963	2484.000	1.324
2483.400	1.227	2477.900	1.797	2483.200	1.722	2514.000	0.999	2484.200	1.296
2483.600	1.195	2478.000	1.879	2483.400	1.478	2515.000	1.016	2484.400	1.269
2483.800	1.177	2478.100	1.645	2483.600	1.337	2516.000	1.080	2484.600	1.269
2484.000	1.138	2478.200	1.973	2483.800	1.212	2517.000	1.121	2484.800	1.318
2484.200	1.125	2478.300	1.717	2484.000	1.157	2518.000	1.094	2485.000	1.342
2484.400	1.131	2478.400	1.771	2484.200	1.119	2519.000	1.117	2485.200	1.367
2484.600	1.120	2478.500	1.620	2484.400	1.124	2520.000	1.178	2485.400	1.370
2484.800	1.109	2478.600	1.701	2484.600	1.136	2521.000	1.105	2485.600	1.355
2485.000	1.121	2478.700	1.631	2484.800	1.125	2522.000	1.035	2485.800	1.328
2485.200	1.112	2478.800	1.686	2485.000	1.151	2523.000	0.963	2486.000	1.232

2485.400	1.115	2478.900	1.669	2485.200	1.178	2524.000	0.916	2486.200	1.178
2485.600	1.112	2479.000	1.678	2485.400	1.173	2525.000	0.876	2486.400	1.133
2485.800	1.111	2479.100	1.685	2485.600	1.186	2526.000	0.831	2486.600	1.055
2486.000	1.117	2479.200	1.570	2485.800	1.152	2527.000	0.809	2486.800	0.990
2486.200	1.116	2479.300	1.641	2486.000	1.118	2528.000	0.713	2487.000	0.919
2486.400	1.106	2479.400	1.570	2486.200	1.114	2529.000	0.685	2487.200	0.858
2486.600	1.116	2479.500	1.464	2486.400	1.074	2530.000	0.719	2487.400	0.810
2486.800	1.126	2479.600	1.591	2486.600	1.042	2531.000	0.693	2487.600	0.775
2487.000	1.107	2479.700	1.514	2486.800	1.027	2532.000	0.734	2487.800	0.731
2487.200	1.109	2479.800	1.526	2487.000	1.012	2533.000	0.699	2488.000	0.719
2487.400	1.112	2479.900	1.634	2487.200	0.985	2534.000	0.705	2489.000	0.728
2487.600	1.120	2480.000	1.448	2487.400	0.946	2535.000	0.720	2490.000	0.868
2487.800	1.108	2480.100	1.517	2487.600	0.923	2536.000	0.782	2491.000	1.177
2488.000	1.113	2480.200	1.456	2487.800	0.909	2537.000	0.777	2492.000	1.513
2489.510	1.076	2480.300	1.697	2488.000	0.893	2538.000	0.763	2493.000	1.793
2491.020	1.087	2480.400	1.627	2489.510	0.902	2539.000	0.908	2494.000	1.692
2492.540	1.070	2480.500	1.749	2491.020	1.104	2540.000	0.939	2495.000	1.547
2494.050	1.112	2480.600	1.776	2492.540	1.354			2496.000	1.632
2495.560	1.161	2480.700	1.768	2494.050	1.339			2497.000	1.641
2497.070	1.174	2480.800	1.896	2495.560	1.296			2498.000	1.660
2498.590	1.178	2480.900	2.105	2497.070	1.368			2499.000	1.742
2500.100	1.170	2481.000	2.206	2498.590	1.403			2500.000	1.700
2501.610	1.140	2481.100	2.270	2500.100	1.375			2501.000	1.602
2503.120	1.137	2481.200	2.286	2501.610	1.314			2502.000	1.510
2504.630	1.140	2481.300	2.362	2503.120	1.203			2503.000	1.385
2506.150	1.131	2481.400	2.637	2504.630	1.163			2504.000	1.288
2507.660	1.116	2481.500	2.762	2506.150	1.090			2505.000	1.199
2509.170	1.097	2481.600	2.583	2507.660	1.039			2506.000	1.100
2510.680	1.073	2481.700	2.710	2509.170	1.023			2507.000	1.014
2512.200	1.055	2481.800	2.681	2510.680	0.996			2508.000	1.009
2513.710	1.021	2481.900	2.765	2512.200	0.983			2509.000	0.948
2515.220	1.015	2482.000	2.726	2513.710	0.969			2510.000	0.942
2516.730	0.997	2482.100	2.663	2515.220	0.974			2511.000	0.918
2518.240	0.991	2482.200	2.590	2516.730	1.014			2512.000	0.895
2519.760	0.986	2482.300	2.409	2518.240	1.000			2513.000	0.884
2521.270	0.976	2482.400	2.302	2519.760	0.997			2514.000	0.867
2522.780	0.983	2482.500	2.114	2521.270	0.998			2515.000	0.890
2524.290	0.999	2482.600	1.990	2522.780	1.009			2516.000	0.906
2525.800	0.990	2482.700	1.801	2524.290	1.010			2517.000	0.905
2527.320	1.026	2482.800	1.681	2525.800	1.061			2518.000	0.925
2528.830	1.006	2482.900	1.662	2527.320	1.049			2519.000	0.911
2530.340	0.995	2483.000	1.576	2528.830	1.029			2520.000	0.896
2531.850	1.011	2483.100	1.469	2530.340	1.015			2521.000	0.894

2533.370	0.992	2483.200	1.360	2531.850	0.984	2522.000	0.879
2534.880	1.015	2483.300	1.330	2533.370	0.993	2523.000	0.886
2536.390	1.012	2483.400	1.453	2534.880	0.953	2524.000	0.881
2537.900	1.011	2483.500	1.497	2536.390	0.963	2525.000	0.868
2539.410	1.002	2483.600	1.351	2537.900	0.968	2526.000	0.897
2540.930	0.979	2483.700	1.297	2539.410	0.950	2527.000	0.883
2542.440	0.993	2483.800	1.339	2540.930	0.966	2528.000	0.897
2543.950	0.992	2483.900	1.283	2542.440	0.957	2529.000	0.888
2545.460	0.992	2484.000	1.335	2543.950	0.971	2530.000	0.916
2546.980	1.015	2484.100	1.225	2545.460	0.993	2531.000	0.869
2548.490	1.026	2484.200	1.346	2546.980	1.035	2532.000	0.864
2550.000	1.014	2484.300	1.409	2548.490	1.069	2533.000	0.848
		2484.400	1.217	2550.000	1.108	2534.000	0.863
		2484.500	1.182			2535.000	0.848
		2484.600	1.257			2536.000	0.882
		2484.700	1.381			2537.000	0.854
		2484.800	1.215			2538.000	0.833
		2484.900	1.296			2539.000	0.839
		2485.000	1.389			2540.000	0.837
		2485.100	1.294				
		2485.200	1.338				
		2485.300	1.200				
		2485.400	1.356				
		2485.500	1.398				
		2485.600	1.396				
		2485.700	1.322				
		2485.800	1.350				
		2485.900	1.282				
		2486.000	1.370				
		2486.100	1.284				
		2486.200	1.379				
		2486.300	1.358				
		2486.400	1.345				
		2486.500	1.369				
		2486.600	1.321				
		2486.700	1.330				
		2486.800	1.318				
		2486.900	1.406				
		2487.000	1.244				
		2488.000	1.437				
		2489.000	1.312				
		2490.000	1.410				
		2491.000	1.354				

2492.000	1.449
2493.000	1.315
2494.000	1.407
2495.000	1.388
2496.000	1.355
2497.000	1.317
2498.000	1.195
2499.000	1.352
2500.000	1.212
2501.000	1.292
2502.000	1.418
2503.000	1.451
2504.000	1.396
2505.000	1.389
2506.000	1.435
2507.000	1.464
2508.000	1.377
2509.000	1.297
2510.000	1.362
2511.000	1.280
2512.000	1.385
2513.000	1.300
2514.000	1.246
2515.000	1.076
2516.000	1.089
2517.000	0.947
2518.000	1.037
2519.000	1.078
2520.000	0.972
2521.000	0.917
2522.000	1.092
2523.000	0.978
2524.000	0.941
2525.000	1.081
2526.000	0.955
2527.000	0.950
2528.000	1.052
2529.000	0.983
2530.000	0.842

Appendix Table C3: S-XANES spectra of S-bearing standards

Pyrrhotite [S^{2-}]		Gypsum [S^{6+}]		Sodium Sulfite [S^{4+}]	
[eV]	**Intensity**	**[eV]**	**Intensity**	**[eV]**	**Intensity**
2460.20	-0.01275	2460.16	-0.01242	2460.17	0.00112
2460.30	-0.01412	2460.40	-0.01140	2460.40	0.00176
2460.50	-0.01040	2460.63	-0.01248	2460.63	0.00053
2460.70	-0.01093	2460.87	-0.01397	2460.87	-0.00007
2460.90	-0.01634	2461.10	-0.01070	2461.10	0.00104
2461.10	-0.01311	2461.34	-0.01425	2461.34	0.00360
2461.30	-0.01197	2461.57	-0.01351	2461.58	-0.00016
2461.50	-0.01377	2461.81	-0.01146	2461.82	0.00388
2461.70	-0.01123	2462.05	-0.01430	2462.05	0.00108
2461.90	-0.00893	2462.28	-0.01171	2462.29	-0.00007
2462.10	-0.01138	2462.52	-0.01275	2462.51	-0.00117
2462.20	-0.01066	2462.75	-0.01412	2462.77	-0.00295
2462.40	-0.00864	2462.99	-0.01040	2463.00	-0.00547
2462.60	-0.00943	2463.23	-0.01093	2463.22	-0.00415
2462.80	-0.01203	2463.46	-0.01634	2463.46	-0.00131
2463.00	-0.01550	2463.70	-0.01311	2463.69	-0.00141
2463.20	-0.00845	2463.93	-0.01197	2463.93	-0.00146
2463.40	-0.01204	2464.17	-0.01377	2464.15	-0.00460
2463.60	-0.00857	2464.41	-0.01123	2464.40	-0.00123
2463.80	-0.00815	2464.65	-0.00893	2464.63	-0.00301
2464.00	-0.01099	2464.88	-0.01138	2464.86	-0.00284
2464.20	-0.00820	2465.12	-0.01066	2465.11	-0.00281
2464.40	-0.00891	2465.36	-0.00864	2465.35	-0.00482
2464.60	-0.00768	2465.59	-0.00943	2465.62	-0.00300
2464.70	-0.00858	2465.83	-0.01203	2465.85	-0.00320
2464.90	-0.00497	2466.07	-0.01550	2466.08	-0.00582
2465.10	-0.00766	2466.31	-0.00845	2466.32	-0.00446
2465.30	-0.00790	2466.54	-0.01204	2466.56	-0.00237
2465.50	-0.00374	2466.78	-0.00857	2466.79	-0.00350
2465.70	-0.00392	2467.02	-0.00815	2467.02	-0.00443
2465.90	-0.00372	2467.26	-0.01099	2467.28	-0.00278
2466.10	-0.00267	2467.50	-0.00820	2467.50	-0.00554
2466.30	-0.00476	2467.74	-0.00891	2467.72	-0.00264
2466.50	-0.00120	2467.98	-0.00768	2467.95	-0.00265
2466.70	-0.00021	2468.21	-0.00858	2468.20	-0.00031
2466.90	-0.00364	2468.45	-0.00497	2468.44	-0.00082
2467.10	-0.00038	2468.69	-0.00766	2468.68	0.00462
2467.30	-0.00072	2468.93	-0.00790	2468.92	0.00291
2467.40	0.00474	2469.17	-0.00374	2469.15	0.00420

2467.60	0.00064	2469.40	-0.00392	2469.42	0.00461
2467.80	0.00497	2469.64	-0.00372	2469.69	0.00819
2468.00	0.00688	2469.88	-0.00267	2469.91	0.00989
2468.20	0.00984	2470.12	-0.00476	2470.14	0.00634
2468.40	0.00926	2470.36	-0.00120	2470.36	0.00749
2468.60	0.01666	2470.60	-0.00021	2470.60	0.00734
2468.80	0.01525	2470.84	-0.00364	2470.84	0.00869
2469.00	0.01944	2471.08	-0.00038	2471.07	0.00952
2469.20	0.02292	2471.32	-0.00072	2471.31	0.01208
2469.40	0.02211	2471.56	0.00474	2471.56	0.01480
2469.60	0.02239	2471.80	0.00064	2471.83	0.02097
2469.80	0.02413	2472.04	0.00497	2472.06	0.02542
2470.00	0.02610	2472.28	0.00688	2472.28	0.02805
2470.10	0.02671	2472.52	0.00984	2472.52	0.03498
2470.40	0.03241	2472.76	0.00926	2472.76	0.04005
2470.50	0.03242	2473.00	0.01666	2473.00	0.04270
2470.70	0.03605	2473.24	0.01525	2473.24	0.04823
2470.90	0.04131	2473.48	0.01944	2473.45	0.05991
2471.10	0.04766	2473.72	0.02292	2473.72	0.05949
2471.30	0.04943	2473.96	0.02211	2473.96	0.06456
2471.50	0.05642	2474.20	0.02239	2474.22	0.07068
2471.70	0.06173	2474.44	0.02413	2474.47	0.07850
2471.90	0.06676	2474.68	0.02610	2474.71	0.08720
2472.10	0.07764	2474.92	0.02671	2474.95	0.09757
2472.30	0.08362	2475.17	0.03241	2475.19	0.11463
2472.50	0.09438	2475.41	0.03242	2475.43	0.13030
2472.70	0.10992	2475.65	0.03605	2475.67	0.15090
2472.90	0.12720	2475.89	0.04131	2475.91	0.17818
2473.10	0.14478	2476.13	0.04766	2476.15	0.21170
2473.30	0.16190	2476.37	0.04943	2476.42	0.25664
2473.50	0.18844	2476.61	0.05642	2476.65	0.32068
2473.70	0.22217	2476.86	0.06173	2476.86	0.41677
2473.90	0.26621	2477.10	0.06676	2477.11	0.56125
2474.10	0.31934	2477.34	0.07764	2477.34	0.76288
2474.30	0.39823	2477.58	0.08362	2477.59	0.97607
2474.40	0.50512	2477.82	0.09438	2477.83	1.11936
2474.60	0.67143	2478.07	0.10992	2478.06	1.16825
2474.80	0.94509	2478.31	0.12720	2478.34	1.13777
2475.00	1.41387	2478.55	0.14478	2478.59	1.04706
2475.20	2.18812	2478.79	0.16190	2478.81	0.93720
2475.40	3.30030	2479.04	0.18844	2479.05	0.86566
2475.60	4.65381	2479.28	0.22217	2479.30	0.86764
2475.80	6.05040	2479.52	0.26621	2479.50	0.92583

2476.00	7.30354	2479.77	0.31934	2479.76	1.00371
2476.20	8.07890	2480.01	0.39823	2480.02	1.08271
2476.40	8.04529	2480.25	0.50512	2480.25	1.17492
2476.60	7.24269	2480.49	0.67143	2480.52	1.28690
2476.80	5.92945	2480.74	0.94509	2480.75	1.40830
2477.00	4.49395	2480.98	1.41387	2481.00	1.53493
2477.20	3.28811	2481.23	2.18812	2481.25	1.64678
2477.40	2.41739	2481.47	3.30030	2481.46	1.74510
2477.60	1.83250	2481.71	4.65381	2481.70	1.84220
2477.80	1.49306	2481.96	6.05040	2481.94	1.93029
2478.00	1.32680	2482.20	7.30354	2482.17	1.98225
2478.20	1.27678	2482.44	8.07890	2482.45	1.99071
2478.40	1.29668	2482.69	8.04529	2482.69	1.95907
2478.60	1.36716	2482.93	7.24269	2482.92	1.89370
2478.80	1.45224	2483.17	5.92945	2483.17	1.78821
2479.00	1.49436	2483.42	4.49395	2483.41	1.64992
2479.20	1.45191	2483.66	3.28811	2483.66	1.49674
2479.40	1.33122	2483.91	2.41739	2483.90	1.35642
2479.50	1.18762	2484.15	1.83250	2484.18	1.24784
2479.70	1.05972	2484.40	1.49306	2484.41	1.16258
2479.90	0.96876	2484.64	1.32680	2484.63	1.10135
2480.10	0.91649	2484.89	1.27678	2484.91	1.06519
2480.30	0.89505	2485.13	1.29668	2485.15	1.04572
2480.50	0.89505	2485.38	1.36716	2485.40	1.03309
2480.70	0.91745	2485.62	1.45224	2485.64	1.02161
2480.90	0.93788	2485.87	1.49436	2485.89	1.02014
2481.10	0.97239	2486.11	1.45191	2486.13	1.01387
2481.30	1.00355	2486.36	1.33122	2486.35	1.00785
2481.50	1.03074	2486.60	1.18762	2486.62	1.00138
2481.70	1.05135	2486.85	1.05972	2486.85	0.98874
2481.90	1.07141	2487.09	0.96876	2487.08	0.97850
2482.10	1.08764	2487.34	0.91649	2487.36	0.96633
2482.30	1.11605	2487.58	0.89505	2487.60	0.95829
2482.50	1.15845	2487.83	0.89505	2487.85	0.95077
2482.70	1.21714	2488.08	0.91745	2488.09	0.95101
2482.90	1.29126	2488.32	0.93788	2488.30	0.95442
2483.10	1.36940	2488.57	0.97239	2488.56	0.96416
2483.30	1.44152	2488.81	1.00355	2488.85	0.97604
2483.50	1.48984	2489.06	1.03074	2489.06	0.99041
2483.70	1.51961	2489.31	1.05135	2489.31	1.01208
2483.90	1.52796	2489.55	1.07141	2489.61	1.03769
2484.10	1.53198	2489.80	1.08764	2489.83	1.06625
2484.30	1.52157	2490.05	1.11605	2490.07	1.09689

2484.50	1.50900	2490.29	1.15845	2490.30	1.12151
2484.70	1.47979	2490.54	1.21714	2490.54	1.14248
2484.90	1.44251	2490.79	1.29126	2490.82	1.15671
2485.10	1.40433	2491.03	1.36940	2491.05	1.16414
2485.30	1.37376	2491.28	1.44152	2491.29	1.16689
2485.50	1.34501	2491.53	1.48984	2491.53	1.16646
2485.70	1.32809	2491.78	1.51961	2491.78	1.16482
2485.90	1.32223	2492.02	1.52796	2492.02	1.16495
2486.10	1.32719	2492.27	1.53198	2492.26	1.16063
2486.30	1.34457	2492.52	1.52157	2492.54	1.15906
2486.50	1.36705	2492.77	1.50900	2492.78	1.15409
2486.70	1.39804	2493.01	1.47979	2493.02	1.14912
2486.90	1.42913	2493.26	1.44251	2493.27	1.14356
2487.10	1.46116	2493.51	1.40433	2493.52	1.14014
2487.30	1.50115	2493.76	1.37376	2493.77	1.14043
2487.50	1.53679	2494.01	1.34501	2494.01	1.13556
2487.70	1.58406	2494.25	1.32809	2494.29	1.13967
2487.90	1.63201	2494.50	1.32223	2494.53	1.14612
2488.10	1.68306	2494.75	1.32719	2494.78	1.15730
2488.30	1.73693	2495.00	1.34457	2495.04	1.17122
2488.50	1.78365	2495.25	1.36705	2495.29	1.18928
2488.70	1.82976	2495.50	1.39804	2495.54	1.20696
2488.90	1.87149	2495.75	1.42913	2495.79	1.22668
2489.10	1.91493	2496.00	1.46116	2496.03	1.24598
2489.30	1.94750	2496.25	1.50115	2496.26	1.26223
2489.50	1.96729	2496.50	1.53679	2496.50	1.27660
2489.70	1.97591	2496.74	1.58406	2496.74	1.29227
2489.90	1.96956	2496.99	1.63201	2496.98	1.30412
2490.10	1.94551	2497.24	1.68306	2497.23	1.31260
2490.30	1.91848	2497.49	1.73693	2497.48	1.32497
2490.50	1.88254	2497.74	1.78365	2497.73	1.33095
2490.70	1.84145	2497.99	1.82976	2498.02	1.33799
2490.90	1.80446	2498.24	1.87149	2498.28	1.34253
2491.10	1.76028	2498.49	1.91493	2498.50	1.34422
2491.30	1.72263	2498.74	1.94750	2498.74	1.34576
2491.50	1.68060	2498.99	1.96729	2498.98	1.34191
2491.70	1.64287	2499.24	1.97591	2499.23	1.33383
2491.90	1.60341	2499.49	1.96956	2499.48	1.32642
2492.10	1.56553	2499.74	1.94551	2499.73	1.31212
2492.30	1.53019	2499.99	1.91848	2500.01	1.29697
2492.50	1.49649	2500.24	1.88254	2500.28	1.28326
2492.70	1.46504	2500.49	1.84145	2500.51	1.26670
2492.90	1.43541	2500.74	1.80446	2500.75	1.24769

2493.10	1.40807	2500.99	1.76028	2501.01	1.23103
2493.30	1.38111	2501.24	1.72263	2501.26	1.21600
2493.50	1.35623	2501.49	1.68060	2501.51	1.19955
2493.70	1.33404	2501.74	1.64287	2501.75	1.18826
2493.90	1.31524	2502.00	1.60341	2502.02	1.17584
2494.10	1.29803	2502.25	1.56553	2502.27	1.16620
2494.30	1.28414	2502.50	1.53019	2502.51	1.15435
2494.50	1.27129	2502.75	1.49649	2502.76	1.14600
2494.70	1.25758	2503.00	1.46504	2502.99	1.13446
2494.90	1.24320	2503.25	1.43541	2503.25	1.13007
2495.10	1.22650	2503.50	1.40807	2503.50	1.12052
2495.30	1.21058	2503.76	1.38111	2503.75	1.11087
2495.50	1.19332	2504.01	1.35623	2504.04	1.10685
2495.70	1.16979	2504.26	1.33404	2504.27	1.09391
2495.90	1.15312	2504.51	1.31524	2504.49	1.08352
2496.10	1.12840	2504.76	1.29803	2504.76	1.07520
2496.30	1.11012	2505.02	1.28414	2505.01	1.06703
2496.50	1.08882	2505.27	1.27129	2505.26	1.05673
2496.70	1.07030	2505.52	1.25758	2505.55	1.04918
2496.90	1.04806	2505.77	1.24320	2505.80	1.04130
2497.10	1.03254	2506.02	1.22650	2506.06	1.03365
2497.30	1.01566	2506.27	1.21058	2506.30	1.02617
2497.50	1.00478	2506.53	1.19332	2506.55	1.02108
2497.70	0.99139	2506.78	1.16979	2506.81	1.01307
2497.90	0.98628	2507.03	1.15312	2507.01	1.00674
2498.10	0.97604	2507.28	1.12840	2507.26	0.99942
2498.30	0.97176	2507.53	1.11012	2507.55	0.99939
2498.50	0.96435	2507.79	1.08882	2507.83	0.99578
2498.70	0.96267	2508.04	1.07030	2508.07	0.99119
2498.90	0.96297	2508.29	1.04806	2508.31	0.98760
2499.20	0.96211	2508.55	1.03254	2508.56	0.98688
2499.40	0.96381	2508.80	1.01566	2508.81	0.98364
2499.60	0.96367	2509.05	1.00478	2509.06	0.98143
2499.80	0.96224	2509.31	0.99139	2509.32	0.98132
2500.00	0.96173	2509.56	0.98628	2509.57	0.98124
2500.20	0.96478	2509.82	0.97604	2509.81	0.98194
2500.40	0.96335	2510.07	0.97176	2510.06	0.98214
2500.60	0.96579	2510.32	0.96435	2510.32	0.98259
2500.80	0.96685	2510.58	0.96267	2510.62	0.98357
2501.00	0.97322	2510.83	0.96297	2510.87	0.98553
2501.20	0.97207	2511.08	0.96211	2511.12	0.98657
2501.40	0.97607	2511.34	0.96381	2511.37	0.98510
2501.60	0.98107	2511.59	0.96367	2511.63	0.98648

2501.80	0.98578	2511.85	0.96224	2511.88	0.98667
2502.00	0.98827	2512.10	0.96173	2512.13	0.98670
2502.20	0.99569	2512.35	0.96478	2512.38	0.98661
2502.40	1.00403	2512.61	0.96335	2512.64	0.98614
2502.60	1.00711	2512.86	0.96579	2512.90	0.98678
2502.80	1.01081	2513.12	0.96685	2513.16	0.98871
2503.00	1.01839	2513.37	0.97322	2513.41	0.99161
2503.20	1.02464	2513.63	0.97207	2513.67	0.99196
2503.40	1.03349	2513.88	0.97607	2513.92	0.99189
2503.60	1.03589	2514.14	0.98107	2514.17	0.99330
2503.80	1.04491	2514.39	0.98578	2514.41	0.99382
2504.00	1.04549	2514.65	0.98827	2514.64	0.99232
2504.20	1.05029	2514.90	0.99569	2514.89	0.99410
2504.40	1.05625	2515.16	1.00403	2515.15	0.99371
2504.70	1.05796	2515.42	1.00711	2515.40	0.99391
2504.80	1.06133	2515.67	1.01081	2515.68	0.99690
2505.10	1.06320	2515.92	1.01839	2515.99	0.99895
2505.30	1.06426	2516.18	1.02464	2516.25	1.00107
2505.50	1.06649	2516.44	1.03349	2516.48	0.99939
2505.70	1.06537	2516.69	1.03589	2516.72	1.00232
2505.90	1.06312	2516.95	1.04491	2516.97	1.00094
2506.10	1.06419	2517.21	1.04549	2517.23	1.00102
2506.30	1.06256	2517.46	1.05029	2517.48	1.00131
2506.50	1.06104	2517.72	1.05625	2517.74	0.99935
2506.70	1.05661	2517.97	1.05796	2517.99	0.99983
2506.90	1.05457	2518.23	1.06133	2518.24	1.00189
2507.10	1.05140	2518.49	1.06320	2518.53	0.99824
2507.30	1.05172	2518.74	1.06426	2518.81	0.99853
2507.50	1.04607	2519.00	1.06649	2519.05	0.99626
2507.70	1.04679	2519.26	1.06537	2519.26	0.99352
2507.90	1.04226	2519.51	1.06312	2519.51	0.99438
2508.10	1.04115	2519.77	1.06419	2519.77	0.99194
2508.30	1.03643	2520.03	1.06256	2520.03	0.98979
2508.50	1.03558	2520.29	1.06104	2520.32	0.99032
2508.70	1.03371	2520.54	1.05661	2520.57	0.99128
2508.90	1.03050	2520.80	1.05457	2520.80	0.98727
2509.20	1.03179	2521.06	1.05140	2521.09	0.98771
2509.40	1.02806	2521.32	1.05172	2521.34	0.98847
2509.60	1.02721	2521.57	1.04607	2521.60	0.98845
2509.80	1.02355	2521.83	1.04679	2521.86	0.98648
2510.00	1.02117	2522.09	1.04226	2522.12	0.98861
2510.20	1.02151	2522.35	1.04115	2522.36	0.98671
2510.40	1.02037	2522.61	1.03643	2522.60	0.98499

2510.60	1.02105	2522.87	1.03558	2522.89	0.98534
2510.80	1.02267	2523.13	1.03371	2523.13	0.98575
2511.00	1.01674	2523.38	1.03050	2523.39	0.98417
2511.20	1.01747	2523.64	1.03179	2523.65	0.98507
2511.40	1.01770	2523.90	1.02806	2523.91	0.98339
2511.60	1.01337	2524.16	1.02721	2524.20	0.98420
2511.80	1.01439	2524.42	1.02355	2524.44	0.98397
2512.00	1.01132	2524.68	1.02117	2524.69	0.98622
2512.20	1.01330	2524.94	1.02151	2524.95	0.98509
2512.50	1.01244	2525.19	1.02037	2525.21	0.98795
2512.70	1.01125	2525.45	1.02105	2525.46	0.98741
2512.90	1.01245	2525.71	1.02267	2525.72	0.99139
2513.10	1.01852	2525.97	1.01674	2525.98	0.99472
2513.30	1.01403	2526.23	1.01747	2526.23	0.99744
2513.50	1.00985	2526.49	1.01770	2526.51	0.99950
2513.70	1.01120	2526.75	1.01337	2526.80	1.00523
2513.90	1.01269	2527.01	1.01439	2527.06	1.01229
2514.10	1.01073	2527.27	1.01132	2527.31	1.02234
2514.30	1.01049	2527.53	1.01330	2527.57	1.03552
2514.50	1.00900	2527.79	1.01244	2527.83	1.05187
2514.70	1.01034	2528.05	1.01125	2528.09	0.96679
2514.90	1.00980	2528.31	1.01245	2528.34	0.44687
2515.10	1.00956	2528.57	1.01852	2528.60	0.72240
2515.40	1.00964	2528.83	1.01403	2528.85	0.87459
2515.60	1.00704	2529.09	1.00985	2529.11	0.91260
2515.80	1.00602	2529.36	1.01120	2529.34	0.93258
2516.00	1.00547	2529.62	1.01269	2529.59	0.94216
2516.20	1.00461	2529.88	1.01073	2529.85	0.94671
2516.40	1.00421	2530.14	1.01049	2530.13	0.95220
2516.60	1.00036	2530.40	1.00900	2530.43	0.95568
2516.80	1.00248	2530.66	1.01034	2530.68	0.95802
2517.00	0.99973	2530.92	1.00980	2530.94	0.96052
2517.20	1.00217	2531.18	1.00956	2531.20	0.96059
2517.40	1.00036	2531.45	1.00964	2531.47	0.96575
2517.60	1.00108	2531.71	1.00704	2531.73	0.96787
2517.80	0.99879	2531.97	1.00602	2531.99	0.96934
2518.10	0.99903	2532.23	1.00547	2532.29	0.97068
2518.30	0.99880	2532.49	1.00461	2532.53	0.97129
2518.50	1.00314	2532.75	1.00421	2532.78	0.97568
2518.70	1.00054	2533.02	1.00036	2533.04	0.97548
2518.90	1.00377	2533.28	1.00248	2533.30	0.97760
2519.10	1.00102	2533.54	0.99973	2533.57	0.98126
2519.30	1.00283	2533.80	1.00217	2533.83	0.98162

2519.50	1.00292	2534.07	1.00036	2534.09	0.98654
2519.70	1.00710	2534.33	1.00108	2534.34	0.99036
2519.90	1.00797	2534.59	0.99879	2534.63	0.99294
2520.10	1.00774	2534.86	0.99903	2534.91	0.99639
2520.30	1.01382	2535.12	0.99880	2535.16	1.00162
2520.60	1.01595	2535.38	1.00314	2535.38	0.99857
2520.80	1.01509	2535.65	1.00054	2535.64	0.99874
2521.00	1.01627	2535.91	1.00377	2535.91	1.00018
2521.20	1.01809	2536.17	1.00102	2536.16	1.00419
2521.40	1.02116	2536.44	1.00283	2536.46	1.00693
2521.60	1.02157	2536.70	1.00292	2536.72	1.00589
2521.80	1.02543	2536.96	1.00710	2536.97	1.00869
2522.00	1.02488	2537.23	1.00797	2537.26	1.00970
2522.20	1.02749	2537.49	1.00774	2537.52	1.01209
2522.40	1.02883	2537.76	1.01382	2537.79	1.01354
2522.70	1.03191	2538.02	1.01595	2538.05	1.01677
2522.90	1.03105	2538.28	1.01509	2538.30	1.01697
2523.10	1.03523	2538.55	1.01627	2538.55	1.01578
2523.30	1.03705	2538.81	1.01809	2538.80	1.01682
2523.50	1.03776	2539.08	1.02116	2539.11	1.01943
2523.70	1.03800	2539.34	1.02157	2539.37	1.02174
2523.90	1.04155	2539.61	1.02543	2539.64	1.02355
2524.10	1.04605	2539.87	1.02488	2539.91	1.02062
2524.30	1.04392	2540.14	1.02749	2540.17	1.02255
2524.50	1.04669	2540.40	1.02883	2540.45	1.02452
2524.70	1.04661	2540.67	1.03191	2540.71	1.02543
2525.00	1.05206	2540.93	1.03105	2540.94	1.02421
2525.20	1.05008	2541.20	1.03523	2541.20	1.02587
2525.40	1.05159	2541.46	1.03705	2541.47	1.02647
2525.60	1.05546	2541.73	1.03776	2541.74	1.02921
2525.80	1.05601	2541.99	1.03800	2542.01	1.03195
2526.00	1.05798	2542.26	1.04155	2542.25	1.03228
2526.20	1.06265	2542.53	1.04605	2542.53	1.03332
2526.40	1.06193	2542.79	1.04392	2542.81	1.03434
2526.60	1.06564	2543.06	1.04669	2543.06	1.03716
2526.80	1.06856	2543.32	1.04661	2543.29	1.03556
2527.10	1.07101	2543.59	1.05206	2543.56	1.03831
2527.30	1.07219	2543.86	1.05008	2543.87	1.04352
2527.50	1.07638	2544.12	1.05159	2544.16	1.04331
2527.70	1.07914	2544.39	1.05546	2544.38	1.04091
2527.90	1.08269	2544.66	1.05601	2544.65	1.04273
2528.10	1.08404	2544.93	1.05798	2544.96	1.04487
2528.30	1.08711	2545.19	1.06265	2545.22	1.04494

2528.50	1.09082	2545.46	1.06193	2545.46	1.04490
2528.80	1.09358	2545.73	1.06564	2545.77	1.04509
2529.00	1.10171	2545.99	1.06856	2546.03	1.04247
2529.20	1.10116	2546.26	1.07101	2546.25	1.04269
2529.40	1.10598	2546.53	1.07219	2546.53	1.04390
2529.60	1.10937	2546.79	1.07638	2546.81	1.04874
2529.80	1.11577	2547.06	1.07914	2547.08	1.04712
		2547.33	1.08269	2547.34	1.04766
		2547.60	1.08404	2547.60	1.04699
		2547.87	1.08711	2547.86	1.04725
		2548.13	1.09082	2548.13	1.05074
		2548.40	1.09358	2548.39	1.04886
		2548.67	1.10171	2548.66	1.04928
		2548.94	1.10116	2548.98	1.04925
		2549.21	1.10598	2549.25	1.04975
		2549.47	1.10937	2549.65	1.05495
		2549.74	1.11577		